uc3m | Universidad Carlos III de Madrid

University Degree in Mechanical Engineering

2017-2018

Bachelor Thesis

"Mechanical and electrochemical characterization of an LFP-CNT deformable composite electrode"

Jesús Almenara Rescalvo

Dr. Juan José Vilatela García

Dr. Nicola Boaretto

EPS, Leganés, September 25th, 2018

ABSTRACT

This dissertation characterizes the mechanical and electrochemical performance of a lithium-ion battery electrode constructed with a commercial active material, lithium ferrophosphate; and an unusual current collector, made of a unidirectional fabric of carbon nanotubes fibers.

These fabrics, produced using a semi-industrial process, combine porosity, toughness and electric conductivity, which enables an enhancement of the typical figures of merit of batteries, such as specific energy; as well as the addition of augmented mechanical properties, like foldability and ductility. Such capabilities pave the way to flexible electronics or batteries integrable in complex geometries, finding gains in energy density. Furthermore, the potential of carbon nanotubes as structural material also opens the door to the development of multifunctional composites which can simultaneously perform the load-bearing and energy-storing tasks.

By means of well-established testing procedures, such as the uniaxial tensile test, for the mechanics; and the rate-capability and cyclability tests versus lithium metal, for the electrochemistry, the manufactured LFP-CNT electrodes are evaluated. A capacity of 160 mAh/g is obtained, close to the theoretical upper limit of LFP. The infiltration of the coating on the CNT substrate allows for the retention of capacity after strains up to 18%, with mild effects on the rate-capability and the aging behavior. The infiltration also reinforces the fabric. Two mechanisms are proposed to explain that behavior: intra-bundle friction enhancement and an effective polymer matrix created from electrode binder.

Keywords: lithium batteries, carbon nanotubes, energy storage, multifunctional composites.

ACKNOWLEDGMENTS

I want to thank all the people who has accompanied me through all these years, in countless occasions, for whose support I am truly grateful to them and to God.

I must thank all my professors, for all the time, effort and passion which dedicate to their indispensable task; and to my University, as a whole, for having provided me with the best possible tools to deal with the future, including a wonderful student housing, where enduring friendships were born.

To my colleagues in the Formula UC3M team, with whom I shared a tough but enriching experience.

To all the friends I met during my years in Mechanical Engineering, with special mention to *California*`s group and what comes associated to it; and to all of those who have accompanied me since earlier, from Toledo, Miguel Esteban and other places over the world, who I can still share my life with.

To Dra. Anastasiia Mikhalchan, for her contributions to this work and the valuable knowledge she selflessly shared with me. To Dr. Nicola Boaretto, for his guidance inside and outside of the laboratory. To my tutor, Dr. Juan José Vilatela, for his inspiring vision of science.

And lastly, to all the members of my family. Especially to my siblings, Daniel and Carmina, who know that, beneath the ordinariness of everyday life, lie profound trust and affection. And to my parents, Prudencio and Mª Carmen, who through their endless love and sacrifice, both mutual and towards the world, are my reference and inspiration.

TABLE OF CONTENTS

TABLE INDEX

FIGURE INDEX

NOMENCLATURE

LIB	Lithium-Ion Battery
CNT	Carbon Nanotube
SHE	Standard Hydrogen Electrode
SI	International System of Units (*Système International*)
SOC	State of Charge
DOD	Depth of Discharge
SOH	State of Health
SOE	State of Energy
SOF	State of Function
EV	Electric Vehicle
BMS	Battery Management System
LTO	Lithium Titanate
LFP	Lithium Ferrophosphate
LCO	Lithium Cobalt Oxide
NMC	Nickel-Manganese-Cobalt
NCA	Nickel-Cobalt-Aluminum
LMO	Lithium Manganese Oxide
SWCNT	Single-Walled Carbon Nanotube
MWCNT	Multi-Walled Carbon Nanotube
CVD	Chemical Vapor Deposition
FCCVD	Floating Catalyst Chemical Vapor Deposition
CF	Carbon Fiber
SEM	Scanning Electron Microscopy
AFM	Atomic Force Microscopy
PVDF	Polyvinylidene Fluoride
NMP	N-Methyl-2-pyrrolidone
EC-DEC	Ethylcarbonate-Diethylcarbonate
CCCV	Constant Current – Constant Voltage
DMA	Dynamic Mechanical Analysis
SEI	Solid Electrolyte Interphase
LFO	Lithium Iron Oxide
SPE	Solid Polymer Electrolyte

1. INTRODUCTION

1.1. Main topic and motivation behind this work

The ever-increasing need for sustainable power sources and forms of energy transport and conservation is, unquestionably, one of the greatest and most crucial challenges that humankind is facing. Thus, it is not surprising that plenty of active research groups worldwide, from varied disciplines related to physics, chemistry and engineering, put a lot of effort in finding discoveries and achieving developments which help fulfill the needs of an increasing demand of cleaner energy.

In this context, as an intrinsic interdisciplinary field, materials engineering plays a vital role serving as hub where research groups work tirelessly to help turn the current anchored habits into a sustainable activity. One of the ways that materials engineering can provide such help is by contributing to the increase in resources usage efficiency, both of energy and feedstock.

There is an undeniably consensus about electricity being the most desirable energy carrier. It is such because of several facts: high efficiency of electric machines, usually beyond 90%, allowing profitable extraction from primary sources (oil, coal, uranium, wind, solar-radiation, etc.) and cost-effective usage; its versatility to be transformed easily from many and into even more kinds of energy such as thermal, chemical, mechanical, etc.; and a relatively simple way to be transported. However, one of the major drawbacks of electric energy is its difficulty to be stored massively, what limits its potential applications. Nevertheless, despite the limitations and complexity, since electricity began to be used as an energy carrier, technologies have been developed to store it to certain degree. Among those, the most prominent ones are batteries, or electrochemical accumulators, which rely on redox chemical reactions between two separated materials to deliver electric current.

The sustainability problems exposed have driven recently a stronger push on the boundaries of the electric-storage technologies. The need of improvements in efficiency and reduction in emissions are forcing that electric-storage is utilized in applications where it had not been needed before, such as transportation or energy generation, as Figure 1.1 shows. For the first one, the low efficiencies and contamination of combustion engines suggest that this technology is substituted by electric motors in the main role of

powering the vehicle. Nonetheless, this puts on a demand on both power and energy densities higher than ever before, due to the sensitivity of vehicles to the mass and volume magnitudes. For energy generation, on the other hand, the relevance of renewable primary sources in the energy-mix, is increasing. Yet sustainable, those sources have the disadvantage compared to the traditional ones that are quite unpredictable and intermittent. Thus, their spread should be supported by the proliferation of back-up facilities where the excesses of energy produced can be stored to be deployed during periods of short-supply. Although batteries have been used for a long time coupled with photovoltaic generators, there is room for improvement in the field. Cost reduction, enhanced aging behavior and higher volumetric energy density would be desirable in order to achieve the generalization of such systems as part of the electrical grid improvement.

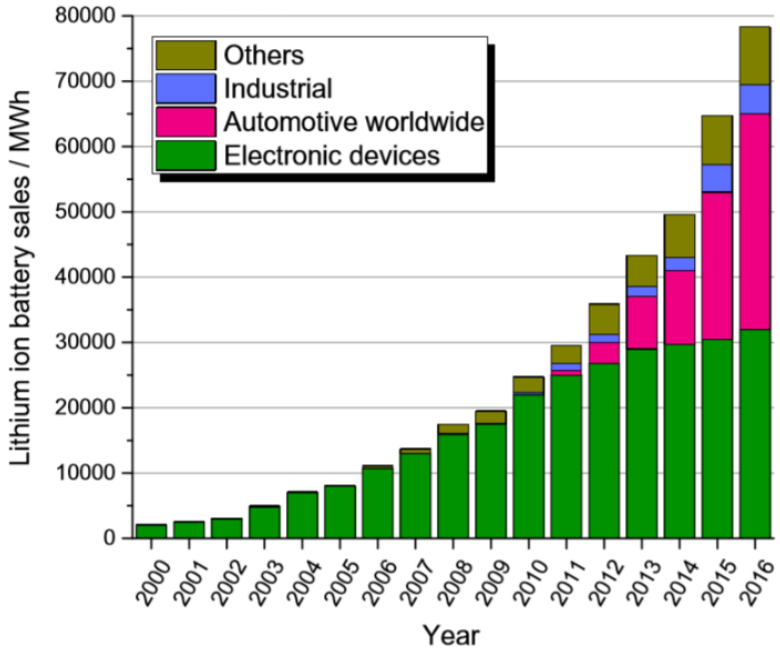

Figure 1.1 Lithium ion battery sales worldwide from 2000 to 2016 (cell level); others: power tools, gardening tools, e-bikes, medical devices, etc. Reproduced from [1].

These are only two of the applications which will drive the development of batteries in the near future, adding to the well-known field of nomadic electronic devices (smartphones, laptops, tablets, etc.), and other developing fields such as biomedical implants.

Although the landscape of distinct battery technologies is vast and heterogeneous, the most relevant kind since the nineties is the lithium-ion battery (LIB) thanks to its superior

energy and power density compared to other technologies such as lead-acid or nickel-cadmium [2].

Therefore, the main topic of this work is the mechanical and electrochemical study of LIB electrodes made with an innovative material, carbon nanotubes (CNTs). The aim is to obtain a component with better characteristics than current LIB electrodes: more specific energy density, both volumetric and gravimetric; and better behavior under extreme conditions of aging (many cycles) or current densities (quick charge-discharge).

However, the utilization of nanomaterials like CNTs does not only contribute to the enhancement of the traditional figures of merit of batteries, but it also makes possible to include new characteristics such as flexibility or ductility, what opens the door to the implementation of flexible wearable electronics or deformable batteries capable of being integrated in geometrically complex structures, such as body-panels of vehicles, with the subsequent advantages in volumetric exploitation. In fact, more recently, a strong interest has appeared for the fabrication of batteries with augmented mechanical properties which can not only be integrated into structures but to carry out the load-bearing function themselves. To continue with the previous example, instead of embedding energy-storing layers in the cavities of the body and chassis of a vehicle, the actual structural material would simultaneously provide with mechanical integrity and store energy. These *multifunctional composites* could thus offer higher weight reductions [3].

Altogether, the long-term goal of this project is to contribute to that ongoing research field by helping understand the mechanical and electrochemical behavior of a CNT-based electrode.

The dissertation begins with an introduction of the main characteristics of batteries, as well as a review of the lithium-ion technology in particular. After that, carbon-nanotubes are presented and their suitability for their utilization as electrodes is explained. This introductory chapter is completed with some works of the research community about the utilization of CNTs for energy-storing, and the concretion of the specific objectives of the experimental work, which constitutes the core of the text.

To ensure a good comprehension of the work, the next chapter is dedicated to the experimental methods used: a birds-eye-view of the strategy followed, a relation of the materials tested and the manufacturing process, and a detailed description of the mechanical and the electrochemical tests performed. The regulatory framework for the

laboratory works is also commented here, both in terms of occupational risks and technical standards.

Once the method has been introduced, the results and discussion of each branch of the work, mechanical and electrochemical, are presented respectively in chapters 3 and 4. The results sections of each chapter present the data objectively but contain comments on the difficulties faced during the experimental process, something unavoidable when doing laboratory work, especially in the case of such a novel material like carbon nanotubes. The discussion in each chapter proposes different hypotheses to the phenomena occurring in the material which explain the trends observed.

Chapter 5 contains the budget for the realization of the study and a brief analysis of its social and economic implications.

To finish the work, the conclusions are summarized in chapter 6, going back to an overview of the material properties obtained, merging the mechanical and electrochemical approaches; and presenting a reflection on future directions of research in the fields of energy-storing by LIBs and multifunctional composites.

1.2. State of the Art

1.2.1. Secondary lithium-ion batteries

1.2.1.1. Battery: definition and working principle.

A battery can be defined as a system which extracts an electric current from the electrochemical oxidation-reduction (redox) reaction between two materials. It was firstly developed by an Italian professor, Alessandro Volta, in 1800. [4]. The material that is oxidized in the reaction (gives electrons) is denoted as *anode*. The other one, which is reduced (accepts electrons), is called *cathode*.

Depending on their nature, batteries are classified into *primary batteries*, if the reaction is non-reversible and they can only be discharged once; and *secondary batteries*, also known as *rechargeable batteries* or *accumulators* [5], when the reaction can be reversed by the application of an inverse electric potential, thus setting the system back to the initial state.

The first widely used primary battery was created by Leclanché in 1865 [4], whereas the first known secondary battery was presented by Gaston Planté in 1859 [5]. Since that time, a wide variety of different types of batteries has been developed, thanks to the

multiple combinations of possible redox couples, each one with its own advantages and disadvantages.

1.2.1.2. Structure of a battery

Strictly speaking, the term *battery* is commonly referred to a system which gives a certain voltage and current output thanks to an internal array of *cells*, which are the minimum units where the redox reactions occur. Depending on the way that several cells are electrically connected, different properties are increased: potential, if it is in series; current, if it is in parallel. From here in advance, we will refer the terms *battery* and *cell* indistinctly, although the underlying distinction between them should not be forgotten.

The electrochemical cell has three basic components [6]: a negative electrode, a positive electrode, and an electrolyte. The electrodes contain the active materials which participate of the redox reaction. In a primary battery, the negative electrode always acts as the anode, and the positive as the cathode. However, if the battery is rechargeable, each electrode can play both roles, depending on if it is being discharged (negative, anode; positive, cathode) or charged (negative, cathode; positive, anode) [5]. The electrolyte is an ideally passive medium that allows the movement of ions from one electrode to another. It is typically a liquid electrolytic solution, with water or an organic solvent; although solid ionic conductors are sometimes used [6].

Each of those three basic components is formed by a number of subcomponents which play a specific role within the assembly, and which depend on the chemistry of the cell. For example, in a battery with a liquid electrolyte, a physical separator is normally needed to prevent the contact between the electrodes, which would cause short-circuits. But if the electrolyte is a solid, a separator is not needed. The following paragraphs will focus on the secondary lithium-ion battery (LIB).

LIBs are based on a redox reaction in which lithium-ions are interchanged between two materials where they are allocated through reversible intercalation [6]. Equation (1.1) shows the expanded chemical equation of a typical LIB cell, with a lithiated transition metal-oxide in the positive electrode and graphite at the negative.

$$\begin{gathered} LiMO_2 \leftrightarrow Li_{1-x}MO_2 + xLi^+ + xe^- \\ C_6 + xLi^+ + xe^- \leftrightarrow Li_xC_6 \\ LiMO_2 + C_6 \leftrightarrow Li_xC_6 + Li_{1-x}MO_2 \end{gathered} \tag{1.1}$$

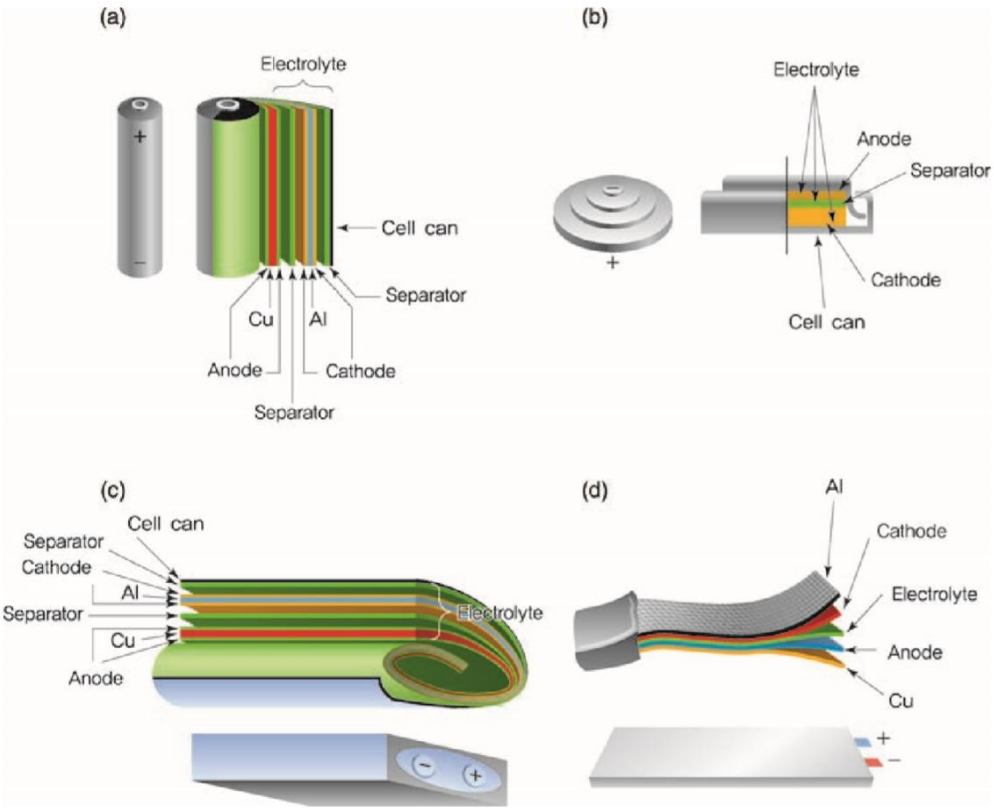

Figure 1.2: Different shapes of lithium secondary batteries:(a) cylindrical, (b) coin, (c) prismatic, (d) pouch. Reproduced from Principles and Applications of Lithium Secondary Batteries *[4].*

Figure 1.2 shows the most common kinds of cell shape for LIBs: cylindrical, coin, prismatic and pouch. It is possible to observe auxiliary components such as the casing, which is different for each shape type; or the aforementioned separator. The electrodes are comprised of the lithium-intercalating active material; a carbonaceous conductive agent; a polymer binder to hold the mix together; and a metallic current collector (normally Al for the positive and Cu for the negative) to canalize the flow of electrons to the terminals of the battery. In the case of the electrolyte, a separator is usually present, as the most common form is the liquid ionic solution formed by a nonaqueous organic solvent and a lithium salt. Apart from this, the electrolyte frequently contains additives as organic compounds to achieve special functions such as overcharging protection. Finally, other necessary components are the casing, which can have many different forms, and protects the battery; and the terminals, which are normally aluminum and nickel tabs [4].

1.2.1.3. Properties of a battery.

Theoretical limit: voltage, capacity and energy

For a given combination of active materials, which are the actors of the redox reaction, there exist some theoretical values which are intrinsic to the electrochemical process that

takes place between both electrodes. Each material has intrinsic reduction potentials, as well as an inherent capacity to store electric charge. The potentials are related to the tendency of a chemical compound to be oxidized or reduced, while the capacity is linked to the amount of charge than an electrode can store. Thus, the choice for the positive and negative electrodes will determine the electrochemical operation of the cell.

The theoretical potential (V_{Th}) of a cell is given by the difference in the standard reduction potential of the anode and the cathode (eq. (1.2)). Its units are Volts [6]. As the electric potential is always as a difference, the "standard" potentials are, by convention, tabulated in terms of the standard hydrogen electrode (SHE), which is arbitrarily given the value of 0.00 V [5]. Sometimes in this work we will utilize instead the potential vs. lithium metal (vs. Li^+/Li). The reason is that lithium has one of the lowest standard oxidation potentials (-3.05 V vs. SHE, [5]), so it is often used as a baseline.

$$V_T = E^r_{0\,cathode} - E^r_{0\,anode} \tag{1.2}$$

The theoretical capacity of one electrode, also known as "coulombic", is determined by the mass of active material of each electrode. Faraday's law (1.3) is used to translate that mass to electric charge [5].

$$m_{active} = R_F \frac{M\ Q}{n\ F} \tag{1.3}$$

Where,

m_{active} is the mass of active material (g);

R_F is the faradaic efficiency of the conversion, usually close to 1;

M is the molar mass (g/mol);

Q is the amount of electric charge (C);

n is the number of moles of electrons transfered per mole of active material (more simply, the coefficient of the "e^-"term on the redox reaction equation);

F is the Faraday's constant (96485 C/mol).

In the SI, the capacity has its own specific unit, the coulomb (C). However, in the battery field, capacity is normally expressed in ampere-hour (Ah) or milliampere-hour (mAh) [5].

An inherent specific capacity for active materials can be defined, usually normalized by mass (gravimetric, (1.4)), although for certain applications is preferred the normalization by volume (volumetric capacity) (1.5).

$$C_{Th_m}\left[\frac{Ah}{g}\right] = 3600 * \frac{n\,F}{M} \tag{1.4}$$

$$C_{Th_v}\left[\frac{Ah}{cm^3}\right] = C_{Th_m} * \rho \tag{1.5}$$

The theoretical capacity (C_T) of a battery is the quantity of charge that can be stored in it. It is given by the capacity of the limiting electrode (1.6), which is the electrode whose active material acts as limiting reactant in the redox reaction.

$$C_T = m_{active}^{lim}\, C_{Th_m}^{lim} \tag{1.6}$$

It is rarely the case that the two electrodes are stoichiometrically balanced. For example, in the case of the LIBs, the anode capacity must exceed that of the cathode, for safety reasons: if the cathode's capacity is larger than the anode's, lithium metal is deposited at the anode at the end of the charge (when the anode is full) [4], causing undesirable effects.

Finally, the theoretical limit of a cell is completed by the theoretical energy that it can potentially deliver (1.7). That energy is the product of the theoretical capacity of the cell and the potential at which it is able to deliver it.

$$E_T = C_T\, V_T \tag{1.7}$$

These three theoretical limits are very useful because they set up a benchmark for each combination of materials. Nevertheless, practical electrodes and cells never reach those values due to complexity of the electrochemical process involved.

The real-life operation of an electrochemical cell is affected by many different parameters such as temperature, aging, current density, state of charge (SOC), etc. Therefore, the basic electrical parameters such as voltage, charge or energy available are characterized in special ways, which are often related to the specific conditions at which they were measured. In the following paragraphs details will be introduced on how the basic parameters of a real battery are normally indicated.

Voltage: open-circuit, nominal and cut-off.

The voltage of a battery changes whether it is measured in open- or closed-circuit conditions, as that of any electrical power source. The *open circuit voltage* of a cell is

defined as the voltage drop measured between the terminals of a battery when it is not connected to any load. It is usually close to the theoretical voltage.

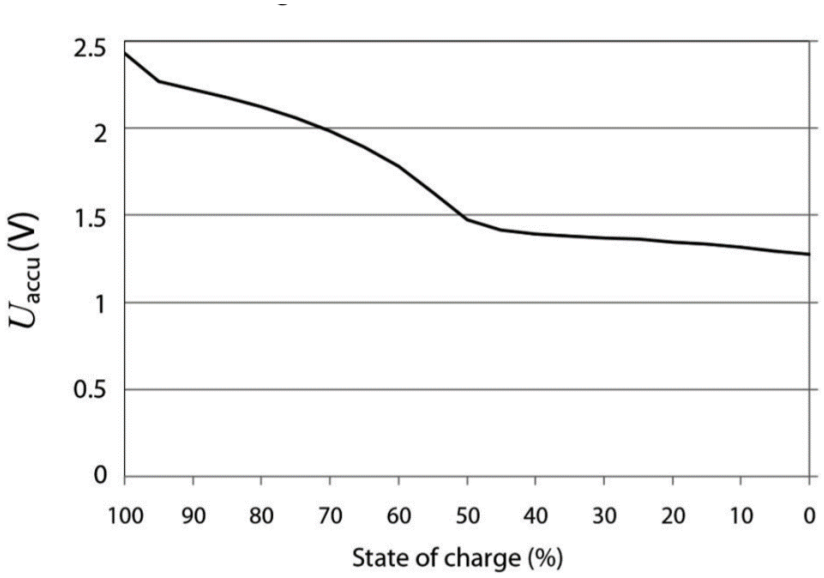

Figure 1.3: The voltage of a lithim-$Li_2Ti_3O_7$ secondary battery versus SOC. [5]

As opposed to this, once a load is connected to any source, the potential is reduced due to the losses which appear, such as the ones related to the Joule effect, which will be denoted as *ohmic* losses. In the case of a battery, the potential also varies with other parameters such as the SOC or the current (see Figure 1.3) due to the *polarization* effects, which are caused by redistributions of the electric charges. Therefore, it is common to denote the *nominal voltage* as the average value of the voltage drop between the terminals in closed-circuit conditions, with moderate discharge current (the idea of "moderate" will be explained in the next item). It can also be defined in a simpler way as the average between the voltage at 100 % SOC and at 0 % SOC, if the complete discharge curve is not available.

To define the limits utilized for computing the nominal voltage, it is common to fix *cut-off voltages* at which the charge or discharge processes are interrupted. These are usually linked to certain values of SOC that have been obtained experimentally and beyond which it is advisable not to set the battery.

Charge/Discharge current: C-rate.

The current is nothing but the rate of charge or discharge to which a battery is subjected, and it affects not only the ohmic losses but also the polarization effects, which increase with it. Generally speaking, a higher discharge current produces a drop in

nominal voltage and a decrease in *effective capacity* (introduced later). However, in the case of batteries, it is more precise to talk in terms of *current density*, as a 100 mA current will not affect equally a 100 mAh battery and a 2 Ah one. Therefore, the concept of *C-Rate* is utilized.

The C-Rate is a common method to denote the rate of charge or discharge of a battery in terms of its capacity. For instance, if a battery is being discharged at "3C" or "C/10", the number (a) in front of the C means the ratio between the current passing through the circuit (I) and the capacity of the battery (C) (1.8).

$$a = \frac{I}{C} \tag{1.8}$$

Capacity: effective and nominal.

As it happens with the potential, the real capacity of a battery is lower than the theoretical upper bound that it is able to attain, and it varies depending on given conditions such as the discharge current, the temperature or the aging. Therefore, for a set of specific conditions, the cell will have an *effective* capacity, computed as the amount of electricity that it provides over a certain amount of time (1.9).

$$C_{eff} = \int_0^t i(t)\, dt \tag{1.9}$$

The *nominal capacity* is the value that the effective capacity takes at the conditions set by different standards, which change depending on the application of the battery. For instance, the standard IEC 61960-3, which refers to secondary lithium batteries for mobile applications [7], fixes the nominal or *rated capacity* as the amount of electricity provided by the battery over a 5-hour period. Another example is the European Standard EN60952-1, for aircraft batteries, which sets the rated capacity over a 1-hour timespan [8]. In terms of notation, the nominal capacity is often denoted by C_n, where n is the duration of the period use to set the value.

Battery states

Once the nominal capacity is defined, it is possible to express the present amount of electrical charge contained in the electrodes of the battery in relation to that nominal value. It is possible, thus, to define a depth of discharge, or DOD (1.10); and a state of charge, or SOC (1.11). The first one is a measure of the amount of electricity drained from the battery, while the SOC is what remains.

$$DOD = \frac{\int_0^n i(t)\, dt}{C_n} \tag{1.10}$$

$$SOC = \frac{C_n - DOD}{C_n} \tag{1.11}$$

A battery is often degraded by many aging mechanisms that hinder its ability to store and deploy electric energy. To cite some, loss of active material by degradation, modification of crystalline structure of the materials (due to excessive charging temperature, for instance), decohesion of the particles in the electrodes, secondary chemical reactions of pollutants, etc. [5]. All those mechanisms cause the effective capacity of the battery to decrease. To get a quantitative measure of the aging of the battery, the state of health (SOH) is defined. It is a measure of the amount of charge delivered by the battery during discharge with respect to the nominal capacity of the battery (1.12). The way that the SOH of a battery evolves with time and usage depends strongly on the kind of battery and application.

$$SOH = \frac{Q_{discharge}}{C_n} \tag{1.12}$$

Others similar concepts are the state of energy (SOE), which substitute the concept of charge by the energy over the same period; and the state of function (SOF), which is a notion which includes the operating conditions.

Energy and power

Effective stored energy (E_s) is defined using the discharging profiles of the battery (1.13)

$$E_s = \int_0^t i_{discharge}(t)\, v_{discharge}(t)\, dt \tag{1.13}$$

Notice that energy depends on the product of current and voltage profiles. Therefore, the value of maximum stored energy of a battery is for a certain C-rate.

An approximation to the stored energy is often obtained by assuming that the voltage profile is constant and equal to the nominal voltage, V_n (1.14). For some types of batteries, this is not far from reality and the assumption gives a very reasonable estimation. For other batteries in which the slope of the voltage profile is steeper, it becomes less accurate. If the current is set to be constant at a certain C-rate (n), then the estimation becomes yet simpler (1.15), and it is a function of nominal parameters. However, as it was explained

earlier, the underlying concepts below these estimations have to be always watched in order for them to be trustworthy.

$$E_s \approx V_n \int_0^t i(t)\, dt \tag{1.14}$$

$$E_s \approx V_n\, n\, C_n \tag{1.15}$$

In terms of power delivery, it is common to define concepts like *pulse* power, which would be the ability of the battery to withstand certain energy consumption over a short period of time (given for a specific case); or *average* power, as the relation of the total energy stored in a battery and the time it is needed to drain it completely (1.16).

$$P_{av} = \frac{E_s}{t_{discharge}} \tag{1.16}$$

Power figures are, hence, closely related to the application of each battery. For instance, data of pulse power over milliseconds or over tens of seconds will be much more relevant for the battery of a camera flash or an electric vehicle (EV); whereas for the case of a cell phone, the value of average power will be of greater interest. The reason why the power figures are so specifically detailed for given conditions is because they are affected by a great number of parameters, which can be as unrelated as the rate of diffusion of ions on the electrolyte or the performance of the heat-dissipation system, to cite only a couple of them.

Therefore, it is common to distinguish between *power-oriented* and *energy-oriented* systems. This happens because the amount of charge a battery is able to store and its ability to do it quick are mutually-opposed properties and a decision has to be made whether on which one should prevail. Hence, applications which demand smaller power figures will sacrifice the ohmic and polarization losses to be able to store more energy (for instance, increasing the thickness of the active material layer of the electrodes), and other applications in which the power supply must be favored will penalize the energy density of the batteries to reduce as much as possible the losses within the components. An example could be an increase of the current collector thickness to decrease resistivity, increasing the amount of inactive mass of the battery.

Specific magnitudes

Values for capacity and energy are usually provided on a “per unit mass” or “per unit volume” basis, as a way to compare different battery systems and to address their suitability to certain applications. They depend considerably on the basis used for

calculation, because batteries have many passive elements which add inactive weight and volume. Thus, it is not the same to compute the theoretical specific capacity of a given active material, that the specific capacity of an electrode, with its current collector; or even the specific capacity of a usable battery, with all its auxiliary components. It is common to use the term *specific capacity* to refer the gravimetric value and *energy density* the volumetric one.

In a work by Kasavajjula et al. [9], a formula for the specific capacity of a LIB full cell is presented, provided that the specific capacity and the specific inactive mass are available.

$$Q_{cell} = \frac{1}{\frac{1}{C^{+}_{Th_m}} + \frac{1}{C^{-}_{Th_m}} + m'_{in}} \tag{1.17}$$

Where,

Q_{cell} is the total specific capacity of the LIB, in mAh/g;

$C^{+}_{Th_m}$, and $C^{-}_{Th_m}$ are the gravimetric capacities of the cathode and anode, respectively, in mAh/g.

m'_{in} is the specific mass of inactive components, in g/mAh.

Coulombic and energy efficiency

To finish section 1.2.1.3, the concept of coulombic (or faradaic) and energy efficiency of a secondary battery is presented.

The coulombic efficiency is measured over a cycle of charge and discharge and is the ratio between the electricity delivered in discharge and the amount "injected" upon charging (1.18).

$$\eta_C = \frac{\int_0^{t_1} i_D(t)\, dt}{\int_{t_1}^{t_2} i_C(t)\, dt} \tag{1.18}$$

Usually, the coulombic efficiency is degraded by parasitic processes such as electrolysis or secondary reactions, which rarely happen in lithium secondary batteries. Therefore, is common to see coulombic efficiencies close to 1 for them. Nonetheless, it is also frequent that the electronics associated to the battery management system (BMS)

degrade the faradaic efficiency of batteries, especially of big battery packs composed by multiple cells.

Aside the coulombic efficiency, there is another interesting parameter of a battery which is the energy efficiency, which is defined analogously as the ratio between the energy drained from the battery (defined previously as energy stored, E_s (1.13)), and the energy invested during charging (1.19).

$$\eta_E = \frac{\int_0^{t_1} v_D i_D(t)\, dt}{\int_{t_1}^{t_2} v_c i_C(t)\, dt} \tag{1.19}$$

As it is derived from energy measurements, which are more complex than charge, as explained earlier, it is common that, in LIBs, the fluctuations are greater than the those of the coulombic efficiency. Furthermore, energy efficiency tends to be lower as it reflects the ohmic and polarization losses.

1.2.1.4. LIBs development: origin and trends on electrode improvement

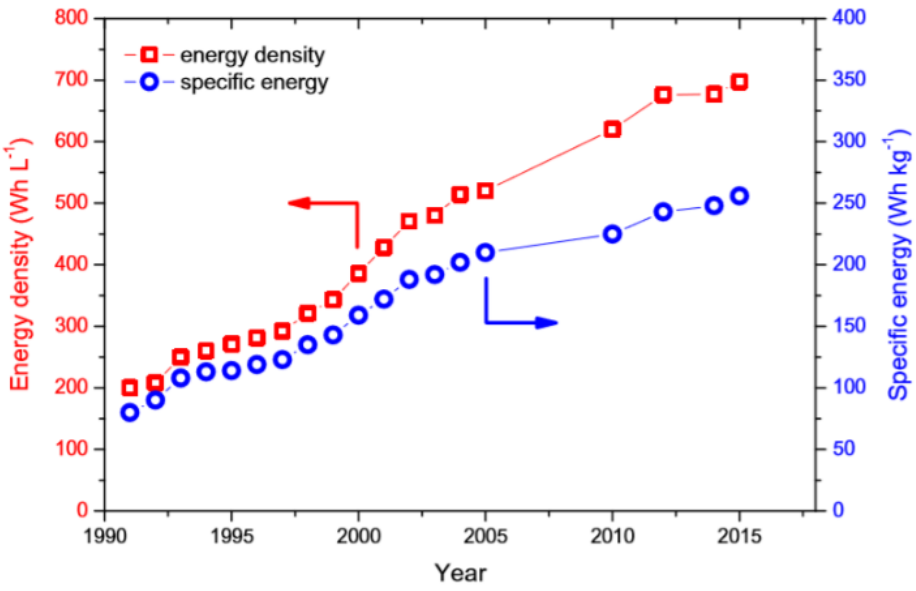

Figure 1.4: Development of the specific energy and energy density of LIBs (cell level) from 1991 to 2017. Reproduced from [1].

The first batteries based on lithium were primary cells developed during the 70s and used lithium-metal as anode material and different options for the cathode such as carbon-monofluoride or manganese dioxide. Soon, during the 80s, a strong research effort was carried out to create secondary batteries based on lithium. However, they had plenty of safety problems due to the deposition of dendrites of metal lithium upon recharging [10]. For that reason, the development of lithium secondary batteries moved to the use of

intercalation materials, with special structures which are retained even when lithium ions are trapped inside them [2]. The appearance of the first “lithium-ion” batteries took place during the 90s, sponsored by the growth of the mobile electronics [10]. More specifically, the introduction by Sony Corp. of the LIB based on graphite-$LiCoO_2$ resulted in a 3.6-V cell with 200 Wh/L and 80 Wh/kg back in 1991 [2]. Since then, LIBs have undergone a rapid development, having currently tripled their specific energy and energy density, as Figure 1.4 reflects (256 Wh/kg and 697 Wh/L) [1].

A great portion of the improvements achieved come from the development of battery electrodes, which is summarized here, with most of the information extracted from reference [2], unless noted.

In terms of anode materials, the focus of research has been applied in the improvement of carbonaceous materials, which were used since the early development of LIBs thanks to their low potential (-2.9 V SHE) and relatively high specific capacity (372 mAh/g, [10]). The trend in development was, mainly, the decrease in size of the SEI passivation layer (which will be explained later) to decrease the irreversible capacity lost during the first charge-discharge cycles.

Besides the research on carbonaceous anodes, other materials proposed for the role of negative electrodes are lithium titanate, $Li_4Ti_5O_{12}$ (LTO) and tin-based anodes. LTO is interesting because its high potential (1.55 V Li/LI^+) gives advantages in terms of power and safety, since larger over-voltages can appear without risks of lithium deposition or irreversible losses of capacity. However, its lower gravimetric capacity compared to graphite (175 mAh/g) and the higher working potential lower the energy density.

Tin is a metal able to store lithium by alloying, instead of intercalation like LTO or graphite, which is interesting because this mechanism has intrinsically a higher energy density. Nonetheless, the volumetric changes which occur upon charge and discharge are also greater in alloying, what causes important problems, because the active material can detach from the current collector. Therefore, the investigation of tin-based materials has targeted the reduction of volumetric changes by, for example, dispersion of nanoscale tin particles in graphite, what yields specific capacities of around 450 mAh/g [11].

For the positive electrodes, the active materials used possess host-structures where lithium-ions can be stored reversibly. These structures can be 1D (olivine), 2D (layered)

and 3D (spinel). In current LIBs, it is possible to find active cathode materials of all three kinds.

Lithium ferrophosphate, $LiFePO_4$ (LFP) is an olivine material with around 140-160 mAh/g of practical specific capacity (theoretical 170 mAh/g) and a potential of 3.4 V Li/Li^+. Its advantages are being relatively cheap and abundant and thermally and structurally safe, which means enhanced safety upon high current densities or sudden temperature rise. Therefore, it is becoming one of the most important active positive materials for EVs.

In the family of layered structures, it is possible to find metal oxides of cobalt, nickel and manganese. $LiCoO_2$ (LCO) was the first material to be used in LIBs, as mentioned earlier. Its main advantage is its high working potential, which reaches up to 4.2 V Li/Li^+ on charging, giving superior energy density. The specific capacity is medium (140 mAh/g), but the main disadvantage are the structural instability and the high cost and toxicity of cobalt. Therefore, since the early 2000s, it was proposed to use "hybrid" nickel-manganese-cobalt oxide, $Li[Ni_{1/3}Mn_{1/3}Co_{1/3}]O_2$ (NMC), more stable, which show a slightly less working voltage compensated by a small increase in specific capacity. Aside these two, there is a vast variety of other layered lithium oxides, among which, nickel-cobalt-aluminum, $Li[Ni_{0.8}Co_{0.15}Al_{0.05}]O_2$, (NCA) must be highlighted, with increased specific capacity but lower thermal stability compared to NMC.

Although NMCs is currently the most widely-used cathode, its properties are only slightly incrementally superior to those of LCO. Therefore, its substitution by other materials is desirable.

The spinel-type of positive electrode material is represented by manganese oxide, $LiMn_2O_4$ (LMO), which offers advantages compared to layered oxides in terms of cost, environmental impact and stability, both structural and thermal. Also, the theoretical capacity of LMO is in line with the others, 148 mAh/g; and the behavior at high rates is good thanks to the 3D structure which allows for many diffusion channels and high conductivity. However, the major drawback of LMO is its bad performance upon aging, with a noticeable decrease in capacity. Therefore, different approaches are currently being studied to reduce the capacity-fade of LMO electrodes after several cycles, which is mainly caused by electrolyte oxidation and dissolution of manganese into it. Specifically,

LMO in the form of nanoparticles shows improvements compared to traditionally used dispersions.

The active materials mentioned represent the most relevant redox-couple members which are currently utilized in LIBs. Nonetheless, as explained in section 1.1, the development of electrical storage is being fostered by the sustainability demands. Therefore, there is a number of research trends in the electrodes field aiming to improve the performance of electrochemical energy accumulators. Two of the most relevant ones are the introduction of high-voltage cathodes (up to 5 V Li/Li^+) and the utilization of nanotechnology to create more efficient layouts of the active materials.

Regarding the first one, several materials have been proposed as high-voltage cathodes: modified LMO with nickel content (4.7 – 4.75 V Li/Li^+) or $LiCoPO_4$ (4.8 V Li/Li^+). However, those potentials are beyond the stability of the electrolytes, which are degraded. One possible solution to this would be the utilization of higher-voltage anodes such as LTO to create safer 3V cells, avoiding the deposition problems of metal lithium during strong charging. There are other cathode materials whose advantages are beyond the scope of this work such as "lithium-rich" cathode layered composites, lithium vanadium phosphate, sulfur and vanadium oxide, although they must be mentioned here as part of the review on incipient lithium-ion technologies. Details about them can be found in reference [12], as well as information of development on negative electrode materials, such as titanium dioxide or silicon, which could be used as an alloying material of extremely high capacity (3578 mAh/g) but presents many challenges.

About the utilization of nanotechnology, one of the most promising fields is the utilization of nanostructured carbonaceous materials such as CNTs, fullerenes and graphene. However, when used directly as intercalation materials, they show high irreversible capacities upon the first charge/discharge cycles, so the main roles they are heading towards are the utilization as nano-structural supports for active material architectures or as highly conductive paths, both things indirectly helping to reduce the inactive mass and volume of the cells.

The application of one of those carbon allotropes, nanotubes, to a LIB electrode, is fundamentally the genesis of this dissertation. The exceptional properties of CNTs, result of its nanometric nature, allow, when combined with the right active materials, not only for an improvement of the classical specifications of a cell but also for the introduction

of new possibilities such as deformability, as it was already exposed at the beginning of this introductory chapter. In the following section, an analysis of the main characteristics of CNTs is presented. For further information on the present and future development of LIBs, Placke et al. offer a comprehensive review [1].

1.2.2. Carbon nanotubes

It has been already discussed the different components which form a lithium-ion battery (see 1.2.1.2) and the features which characterize it, as well as the recent evolution of this technology and its importance. Among those components, attention should be paid to the current collectors.

Traditionally, copper and aluminum have been the choice because of two main properties: high electrical conductivity and electrochemical potentials compatible with the working range of lithium-ion batteries. However, at the same time, these metals account for an important portion of the weight of the electrodes, becoming a significant contribution to the inactive matter of batteries; especially in the case of copper, due to its high density. Besides, they cannot withstand large strains because the active material laid on top (in a process which will be presented later, in section 2.2.3) detaches easily due to the weakness of the mechanical bond between the layers, as reported by Wang et al. [13]. This compromises the mechanical integrity of the battery when it needs to be subjected to large deformations.

Table 1: Some relevant properties of current collector materials.

	Electrical Conductivity (S/m)	Redox potentials (V SHE)	Bulk density (g/cm^3)
Individual CNT	$10^6 - 10^7$ [14]	-2.9 ($Non-constant$) [5]	1.4
CNT fibers mat	$4.04 * 10^4$ [14]		0.39 [14]
Al	$3.83 * 10^7$ [15]	-1.66 [5]	2.703 [15]
Cu	$6.33 * 10^7$ [15]	$+0.34$ [5]	8.89 [16]

A relatively new material has been proposed in recent years to replace copper and aluminum as current collector: carbon nanotubes. This nanomaterial exhibits a range of properties which makes it look as a promising substitute, a comparison of the most relevant ones being presented in Table 1. In that chart two different lines refer to CNTs,

and the great differences between them are remarkable. This happens because, as a hierarchical nanoscale material, carbon nanotubes present a different behavior at the nanometric level than in macroscopic formats. Thus, the properties of an individual CNT are not directly transferred to bulk macroscopic forms of CNT structures. That is why the conductivity measured for individual CNTs can be up to two orders of magnitude larger or why their bulk density is not available, since at the nanoscale its definition becomes non-trivial. However, despite the losses in the path from the nanoscale to the macroscopic world, the properties of bulk forms of CNT materials such as the mats presented in this work are already good enough to be taken into consideration: mainly, relatively high conductivity and low weight. In the meantime, it is an active topic of research the ways to transfer the outstanding properties of single CNTs to the macroscopic level.

An introduction to CNTs and its production process is introduced in the following paragraphs: what they exactly are, how they are made and what are the characteristics behind their performance.

1.2.2.1. CNT as a particular carbon allotrope.

Carbon nanotubes are seamless tubular networks of rolled-up graphene layers in which carbons are assembled together by means of a sp^2-hybrid bond [17]. They were discovered by Ijima in 1991 [18], after the discovery of fullerenes by Kroto and Smally in 1985 [19] had raised the interest in new carbon allotropes.

CNTs have radius on the range of 3 to 30 nanometers, a property which gives their name [20]. The typical length is on the order of micrometers, although they can reach several centimeters with special conditions. Due to the high aspect ratio, they are considered as unidimensional nanomaterials, and their highly ordered structure gives them remarkable properties: electrical conductivities in the range of metals with much lower density (see Table 1), exceptionally high thermal conductivity, around 3500 Wm/K [21], as well as outstanding mechanical properties: 1 TPa elastic modulus and 100 GPa tensile strength [22].

Carbon nanotubes can be classified into two big groups: single-walled and multi-walled, denoted as SWCNT and MWCNT, respectively. The name is self-explanatory: SWCNT are formed by a single layer of graphene, yielding an individual cylinder of 1-2 nm of diameter [23]; on the contrary, MWCNT are composed by several concentric rings of graphene, separated by a distance of 0.34 nm [18]. Figure 1.5 shows the two kinds of

structure. The double-walled nanotube (DWCNT) is a special case of MWCNT with only two layers. MWCNT can have up to 20 layers of concentric tubes [24].

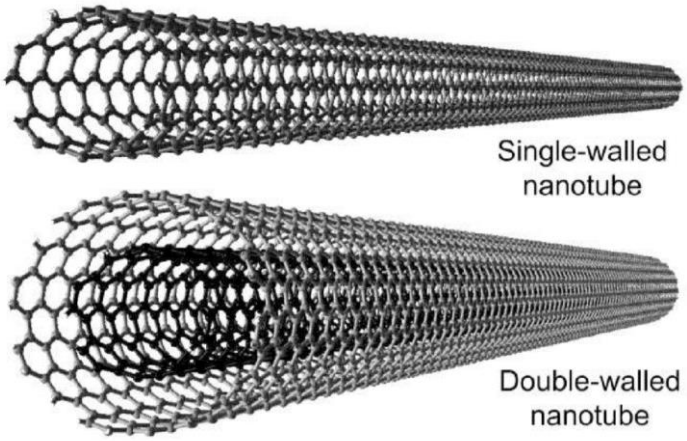

Figure 1.5 Schematic representations of single- and double-walled carbon nanotubes. Reproduced from [24]

1.2.2.2. Manufacturing of CNT mats by Floating Catalyst Chemical Vapor Deposition (FCCVD)

CNTs can be synthetized by three distinct methods, according to literature: electric arc-discharge [25], laser ablation [26] and chemical vapor deposition (CVD) [27], [14]. Nonetheless, only the CVD technique will be covered here, since it is the most popular technique for the production of CNTs [20], and it is the one utilized for the macroscopic veils which are tested later in this work. The reader is referred to reference books such as [28] and [29] for further information on arc-discharge and laser ablation procedures for CNT growth. A comprehensive review of differences and typical properties of CNTs produced by each method is presented by Eder [30].

During the last decade several procedures to create bulk forms of CNT materials starting from CVD have been developed. Stallard et al. [14] divides them into three families: post-processing of vertically aligned CNT forests, utilization of CNT-solvent solutions and continuous direct-spinning of condensate aerogels (also known as “Windle Process”, published by Li et al. in 2004 [31]). Schematics of all of them are depicted in Figure 1.6, from the same paper. The macroscopic mats utilized in this work were produced by the third method.

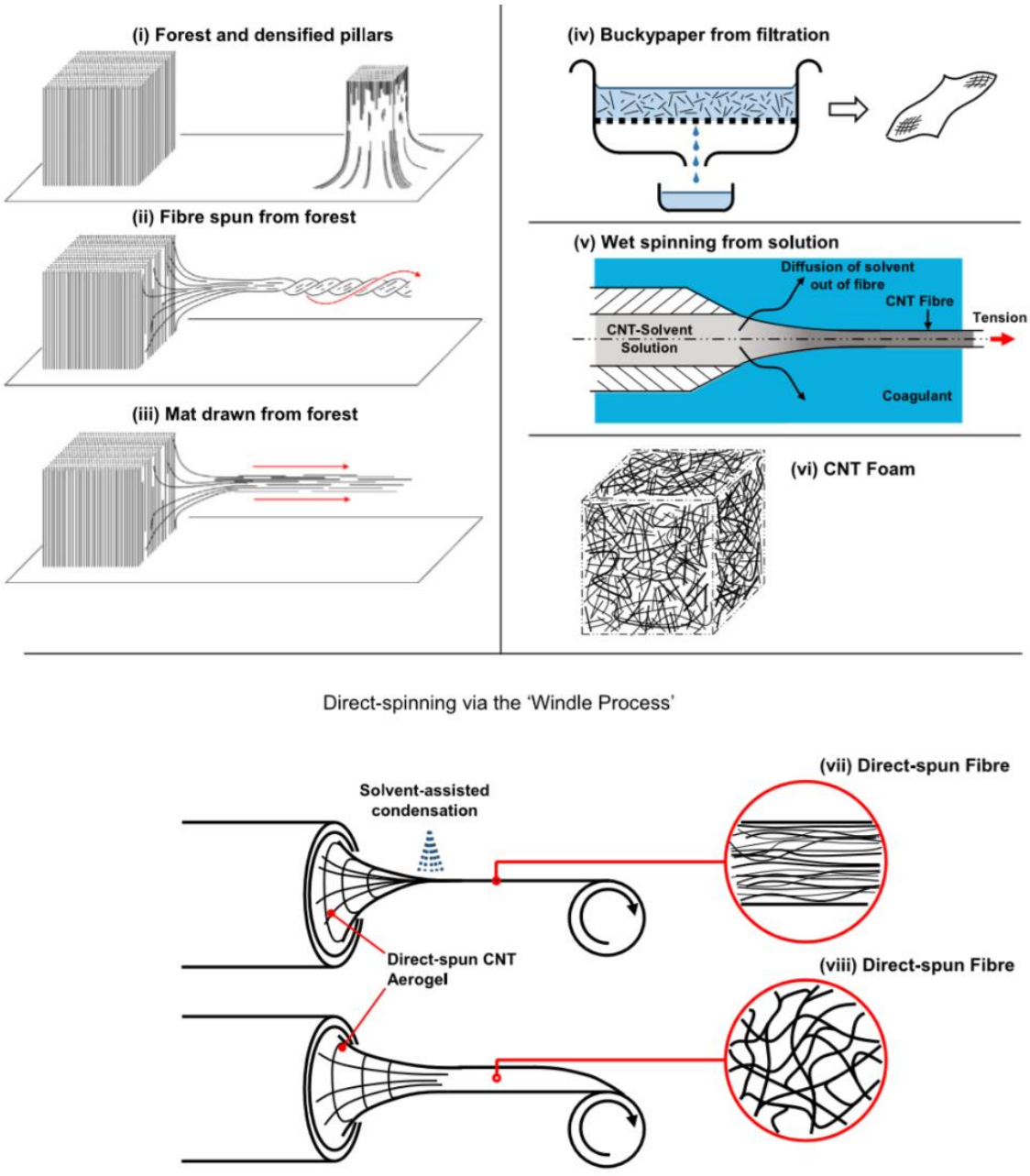

Figure 1.6: Classes of bulk CNT materials and production methods. Reproduced from [14].

The direct-spinning process is basically a continuous, mechanically-assisted CVD process. The key of this method, compared to classical CVD, is that the catalyst nano-particles are injected into the gas flow at high temperature, where they condensate while moving along with the reactant and carrier gases, instead of being fixed to a stationary substrate. This is why is also called floating-catalyst CVD (FCCVD). The result is CNT aerogel continuously synthesized and which can be spun as a macroscopic fibre [14]. The whole process is illustrated in Figure 1.7. It is possible to produce macroscopic CNT yarns or mats by changing the winding geometry.

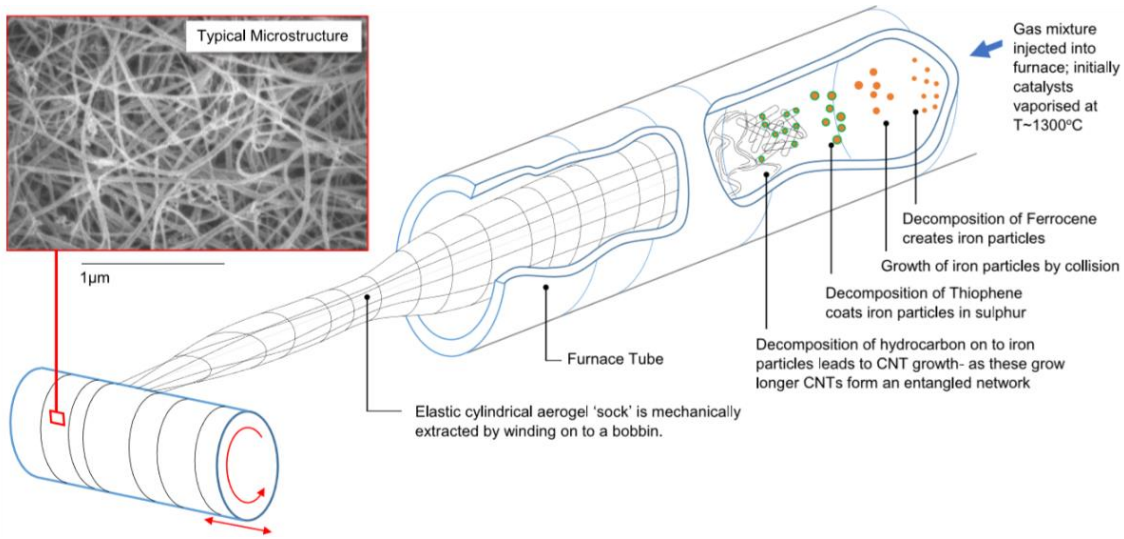

Figure 1.7: The "Windle Process" for producing direct-spun CNT mat, and typical microstructure. Reproduced from Stallard et al. [14].

.

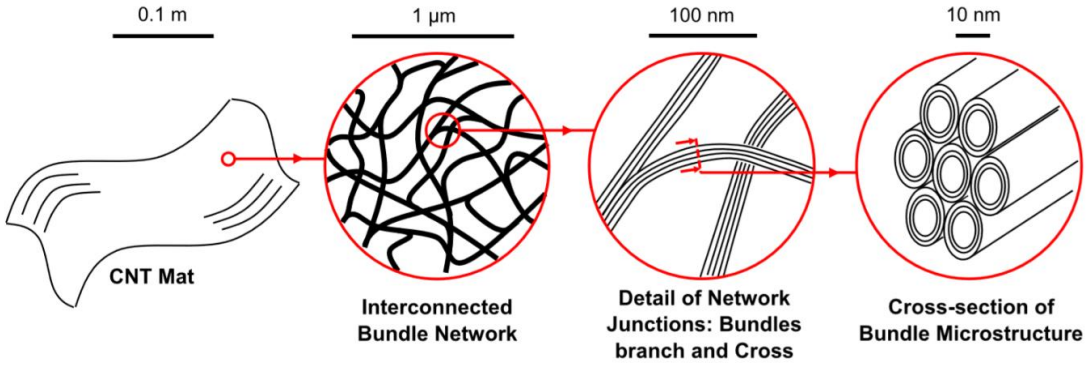

Figure 1.8: The hierarchical microstructure of direct-spun CNT mat. Reproduced from [14].

The microstructure of direct-spun CNT mats and fiber is characteristic. It is a hierarchical structure with three levels: the nanotube, nanotube bundle and the bundle network [32]. Figure 1.8 shows a scheme of this hierarchy.

In this microstructure lies the bottleneck in the transfer of mechanical properties from the exceptional values of individual CNTs to the bulk material. Whereas the nanotube bundles are still very stiff and possess high tensile strength [33], the inter-tube connections are created by weak van-der-Waals interactions which compromises the longitudinal shear strength and modulus. [34].

1.2.2.3. Summary of characteristics of bulk CNT materials

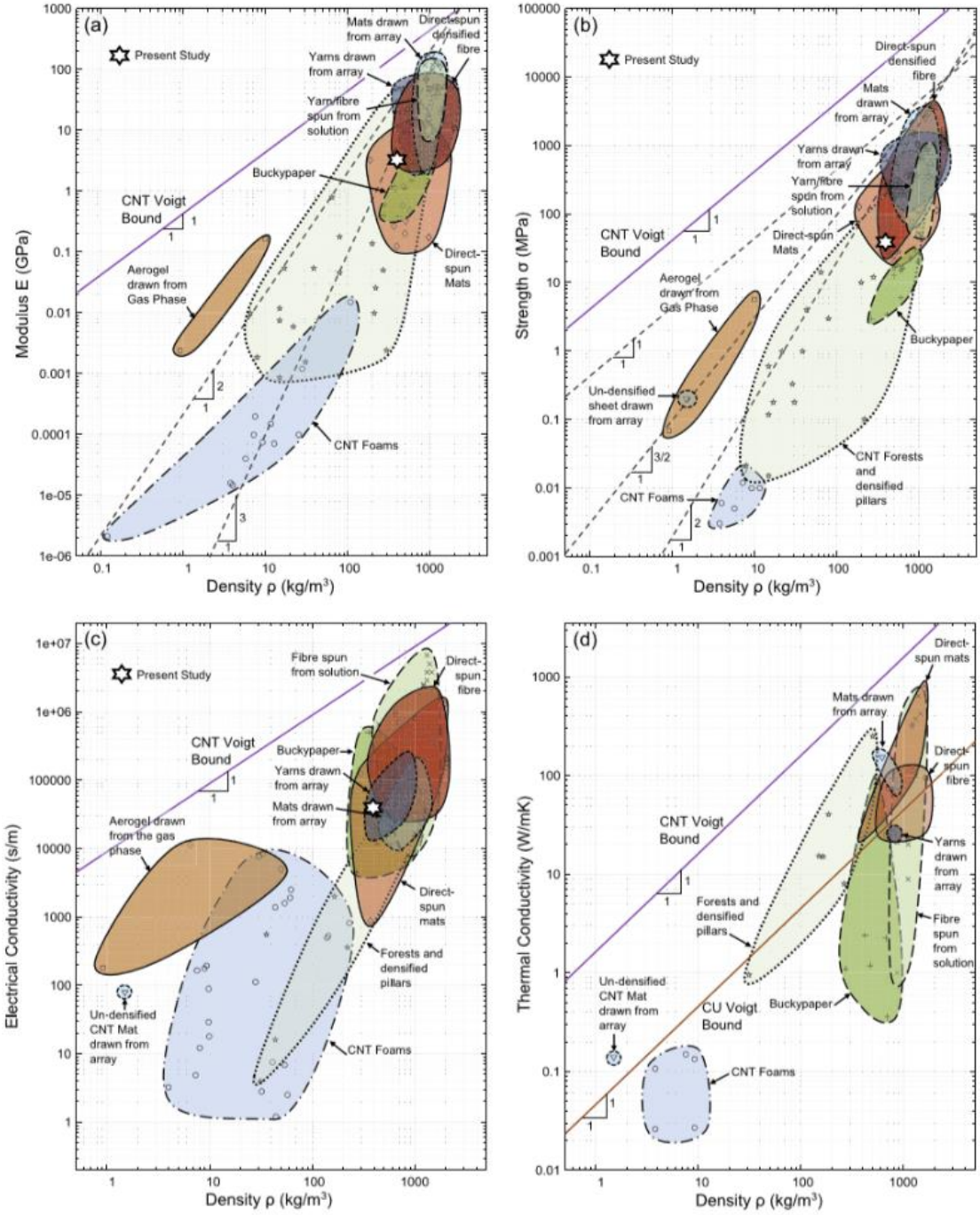

Figure 1.9: Property charts of CNT materials: (a) modulus vs. density. (b) strength vs. density. (c) electrical conductivity vs. density. (d) thermal conductivity vs. density. References for the experimental data used in these property charts are given in the supplementary material of Stallard et al. [14], from where this figure is reproduced.

As it has been exposed, there is a variety of techniques to produce CNTs which importantly affect the properties of the final bulk material. In Figure 1.9 a-d, reproduced from Stallard et al., a comprehensive review of experimental data from various sources is offered. There are four maps where elastic modulus, strength, and electrical and thermal

conductivities are plot versus bulk density. The heterogeneity of the properties among the different processes is notorious. Nonetheless, thanks to the advances achieved by the research community, the bulk CNT forms are getting closer and closer to the Voigt upper bound (denoted in the plots by a purple straight line). This is the theoretical limit as it comes derived from the in-plane properties of graphene sheets [14].

1.2.3. Applications of CNTs for LIB technology enhancement and multifunctional composites.

In a work by Yoon et al. [35], pristine direct-spun CNT are reported to be used as intercalation material themselves, achieving reversible capacities greater than 200 mAh/g after more than 50 cycles thanks to a heat treatment process. Welna et al. report an 800 mAh/g electrode using vertically-aligned CNTs (VACNTs) over a nickel current collector [36], and Sun et al. [37] have produced a lithium-metal anode embedded in a MWCNT scaffold able to deliver up to 2830 mAh/g after 1000 cycles at 1C. Similarly, sulfur-infiltrated VACNTs have been used to create cathodes with high-performance at high temperatures (70-90 ºC), with stable capacities on the range of 400 mAh/g after 150 cycles [38]. In Choi et al. [39], a MWCNT mat produced by coagulation of a dispersed CNT powder was used as the current collector of an LCO cathode, reaching capacities on the order of 100 mAh/g.

There has been progress on the use of CNT fibers in multifunctional electrodes with augmented mechanical properties such as bendability and stretchability. Composite fiber LIB electrodes have been produced by coating CNT fibers with silicon, LMO, LFP or LTO in a coaxial layout, able to attain a gravimetric energy density of 27 Wh/kg in a CNT/LTO-CNT/LMO fiber battery [40]. This “linear” battery can be knitted to make a flexible wearable battery, retaining 84 % of the capacity after 200 cycles at a strain of 100 %. In Hu et al. [41], a folding LCO-LTO battery with CNTs as current collectors is able to retain more than 130 mAh/g after 100 cycles (164.3 mAh/g at the first discharge) while being in a folded state from the 30^{th} to the 70^{th} cycle. Luo et al. [42] have developed a binder-free LCO/CNT cathode capable of 151.4 mAh/g at 0.1C, with 98.4 % retention after 50 cycles; and 90.8 % retention at 2C, compared to 0.1 C. The LiCoO2-CNT nanocomposite was created by simultaneous dispersion of both components in ethanol and co-deposition. Yet flexible thanks to the low thickness, the ductility was low: below 4 %. Also, a foldable graphite-CNT anode with 97 % retention at 2C compared to 0.1C

(326 vs. 335 mAh/g) is reported by Wang et al. [13], although the stretchability is even lower (1.3 % strain at break).

This review of literature shows the potential of CNT arrays in enhancement of LIBs electrochemical and mechanical properties. Nonetheless, it is of interest to produce CNT-containing LIBs with mechanical properties beyond flexibility, forming multifunctional composites in which the energy-storing assemblies also provide with the load-bearing capabilities, instead of being an add-on to the main structural material. In particular, large-area laminar assemblies are attractive because of their similarity with structural composites.

Literature data show that energy-storing CNT fiber-composites are already approaching mechanical specific figures of regular carbon fibers (CFs). Gonzalez et al. [3] report values of 0.2-0.6 and 17-37 GPa/(g/cm^3) for the strength and modulus of a composite CNT fiber, compared to 1.4 and 93 GPa/(g/cm^3) for a regular CF/epoxy composite. This is encouraging as the electrochemical properties of CNTs are superior to those of the regular CFs, thanks to their higher specific surface area (200 vs. 0.2 m^2/g, approx.) [3].

Although most of the concepts on structural energy-storing currently rely on carbon fibers as reinforcement/anode material, it is expected that the advances in the transmission of the outstanding mechanical properties of CNTs to the macroscopic scales will result in new ground-braking combinations of mechanical and electrical properties.

1.3. Objectives

To contribute to the ongoing research on multifunctional CNT fibers, exploring not only the properties, but also the characterization method, of a semi-industrial CNT mat produced by FCCVD.

To address the viability of a stretchable electrode by studying the mechanical and electrochemical behavior of a practical LIB electrode composed of the aforementioned CNT film and a well-known and representative lithium-intercalation positive material such as LFP, with interesting advantages in terms of stability and sustainability.

To get an overview of LIB the state-of-the-art technology and the role that CNTs play in it, locating the outcome of the produced electrodes within that frame, and identifying to some extent the limitations and the potential development lines of the technology, especially in the field of multifunctional composites.

2. EXPERIMENTAL METHODS

2.1. Summary of the strategy and regulatory framework

As stated in the introduction, the core of this project is the experimental work performed on a CNT/LFP electrode.

For the mechanical side of the work, the samples were obtained by manual cutting using knives and paper templates. The specimens were later weighted with a precision balance and their thickness measured with a digital micrometer so that the transverse cross-section and the areal density were known. After the successful tensile test, some of the specimens were submitted to Scanning Electron Microscopy (SEM) to gain more knowledge about the nature of their behavior.

To continue with the electrical part, some of the deformed samples were later electrically tested to address an eventual coupling between mechanical deformation and change in electrical performance.

Regarding the regulatory framework, all the experimental work was carried out after receiving the corresponding training in prevention of occupational risks in laboratories, getting specific detailed handouts on safety in electrochemical laboratories and hazardous waste disposal instructions, provided by FREMAP Prevention Society (*Sociedad de Prevención de FREMAP*), in accordance with the 31/1995 Occupational Health and Safety Act (*Ley de Prevención de Riesgos Laborales, LPRL*).

2.2. Materials

2.2.1. Current collectors: metallic foils and CNT mats.

Current collectors are high-conductivity materials whose purpose is to guide the electrons obtained from the redox reaction to the terminals of the battery and, ultimately, the circuit that needs the electric current.

Typical current collector materials include aluminum and copper, commonly used due to their high conductivities. Aluminum is often used for the positive electrode because, although it should get corroded due to its low redox potential (see Table 1), the natural Al_3O_2 layer passivizes it. In the negative electrode, it would be desirable to use aluminum as well. Nonetheless, aluminum is irreversibly alloyed with lithium at low potential Therefore, copper is used instead, despite its high density, partially compensated by its

very high electrical conductivity. It is usual that current collectors come in the shape of thin foils which can be wounded as desired to create prismatic, cylindrical or pouch cells [6]. The high conductivity of copper allows for the use of thinner foils, reducing the weight penalty.

In this work, the mechanical properties of those typical metallic foils are compared with those of a semi-industrial direct-spun CNT mat produced by IMDEA Materiales (see section 1.2.2.2 for details) which is a potential substitute for them.

It is frequent in this kind of direct-spun mats that there exists some degree of in-plane anisotropy as the result of the winding process, in which the winding direction becomes somewhat favored. Therefore, the winding direction of the mats will be nouned as *longitudinal*, following an analogy to typical ply-based carbon or glass fiber composites [43]. All the properties presented in this text refer always to the longitudinal direction of the mat.

*Table 2: Geometric and mass properties of current collector materials tested. * Unpublished data from IMDEA Materiales*

	Aluminum	**Copper**	**CNT mat**
t, measured (μm)	15 ± 1	10.6 ± 1.0	5 ± 2
ρ_a, measured (mg cm^{-2})	4.1 ± 0.4	8.8 ± 0.7	0.29 ± 0.07
ρ, computed (g cm^{-3})	2.7 ± 0.4	8.3 ± 1.4	0.6 ± 0.4
ρ, literature (g cm^{-3})	2.703 [44]	8.89 [45]	0.33*

Table 2 summarizes thicknesses and areal and volumetric (or bulk) densities for the collector materials tested. The measurements of the thickness were challenging because of the very low values. For the metallic foils, a digital micrometer was used. This method could not be reproduced on the CNT mats. Their high porosity and fragility made it extremely difficult to perform measurements with the micrometer, because the material stuck to the probes and was damaged when released. Thus, the most reliable data was obtained through the SEM images of a cross section of already-coated CNT mat (Figure 2.1). From this source it was decided to assume a thickness value of $5 \pm 2\ \mu m$. Though

the uncertainty value was very high, a smaller choice was considered unrealistic, given the method used.

Regarding the densities, the interesting parameter for us was the areal magnitude, as it will be shown later. However, the volumetric density was used as a figure of merit of the measurements by comparing the experimental values with the numbers found in the literature. From that comparison, it is possible to see that a more accurate measurement of the mass and the thickness would be desirable, in future iterations. Nevertheless, the numbers for aluminum are very accurate. About the copper, it is possible to conclude, according to the difference in densities, that the measure of the thickness was probably a bit overestimated. And regarding the IMDEA mat, it is clear that alternative methods for measuring the thickness are needed in order to reduce the huge uncertainty. Perhaps the utilization of Atomic Force Microscopy (AFM), which was discarded for this work because of the complexity of that procedure, which would have consumed too much of the available time-window.

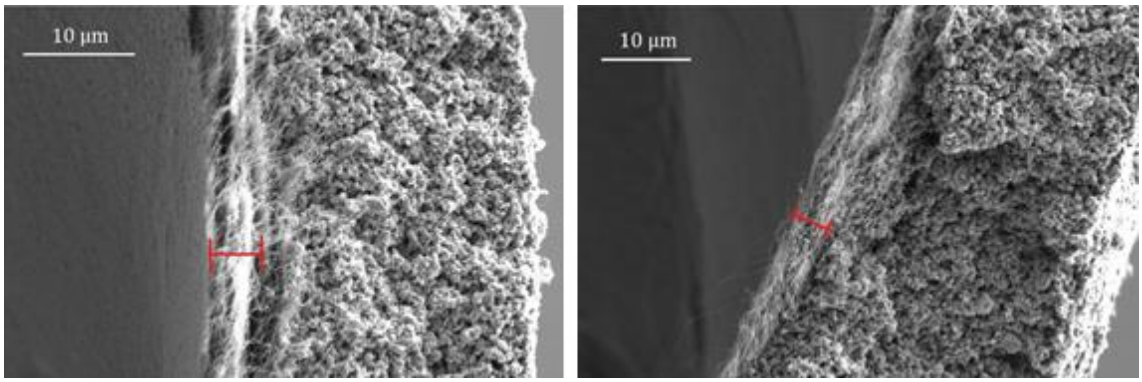

Figure 2.1: Cross-sectional SEM images of the fracture surface of a CNT+LFP electrode after tensile testing. Highlighted in red is the thickness of the CNT mat. The thick, porous layer to the right is the LFP coating. Images courtesy of Anastasiia Mikhalchan.

2.2.2. Active material: LFP

Lithium ferrophosphate, $LiFePO_4$, (LFP) was mentioned in section 1.2.1.4 as a common positive electrode material for LIBs and is the one evaluated in this work. Its redox semi-reaction is expressed in equation (2.1): discharge, left to right; charge, vice versa. In a charged electrode, $(x = 0)$ [5]. It is an olivine compound with orthorhombic crystal structure (Figure 2.2).

$$Li_{(1-x)}FePO_4 + xLi^+ + xe^- \leftrightharpoons LiFePO_4 \qquad (2.1)$$

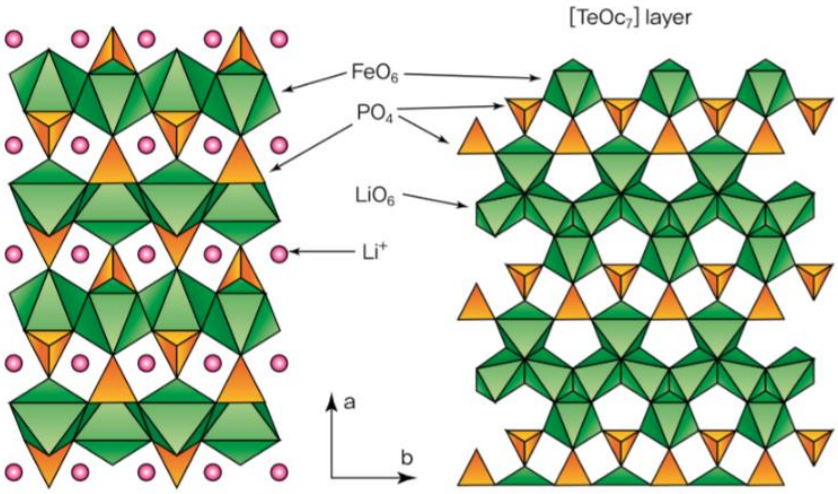

Figure 2.2: Structure of olivine LiFePO4. Reproduced from [4]

The most relevant properties are presented in Table 3. Its main advantages are the chemical, thermal [46] and structural stability, its constant voltage profile upon charge and discharge, and its low cost, abundancy and relatively low environmental impact. Besides, the nominal potential is sufficiently high to get acceptable figures of energy density; but at the same time is slightly lower than that of LCO or NMC, which limits the electrolyte degradation [4]. This, in turn, reduces calendar aging, something especially valuable for medium- and large-size applications such as EVs or energy generation.

Table 3: Some relevant properties of LFP [4], [46].

Theoretical capacity	**Practical capacity**	**Nominal potential**	**Density**	**Electric conductivity**	**Li^+ diffusivity**
170 mAh/g	160 mAh/g	3.4 V vs. Li/Li^+	3.6 g/cm^3	10^{-7}-10^{-9} S/cm	10^{-16} cm^2/s

The cause of the constant voltage profile of LFP is the two-phase deintercalation method of the lithium ions. Instead of a progressive decrease in the concentration of ions, there is a deintercalation "front" which advances between a lithium-rich phase ($Li_{(1-x)}FePO_4$, $x \rightarrow 0$) and the lithium-poor phase ($x \rightarrow 1$), or simply $FePO_4$. Both phases share the same crystalline structure, what contributes to the good stability of LFP [5].

Iron is cheaper, more abundant and less harmful to the environment than other metals utilized in LIBs such as manganese, cobalt or nickel. Therefore, LFP electrodes are more sustainable [47].

The main disadvantages of LFP are the slow diffusivity of lithium-ions and its low electric conductivity. The first is a consequence of its crystal structure, which only allows unidimensional channels for the lithium ions to go through. This problem can be diminished by controlling the size and direction of crystals [47].

The problem of electronic conductivity is palliated through the utilization of very small particle sizes of LFP, coated with carbonaceous additives, with the aim of reducing as much as possible the path that charges need to cover inside the LFP particles. Nonetheless, the control of the coating of the particles and a correct homogenization of them in the electrodes are problems which appear commonly, and there is a great amount of research dedicated to this issue, as reported by Xia et al. [48].

The commercial LFP utilized in this project is LFP-NCO (Lithium Ferrophosphate Nano-co-crystalline) M121 produced by Aleees Co. [49]. It has a surface area of 13 m^2/g, a particle size of 50 nm, and rated capacity of 153 mAh/g at C/10 and 25 ºC.

2.2.3. Complete electrode: current collector with active-material coating

To create the electrode assembly, the current collectors, Aluminum and CNT mat, were coated with a slurry which contained the active material. The composition was a mixture of LFP powder; a conductive additive, carbon black (SUPER P™ Li) and a polymer binder, polyvinylidene fluoride (PVDF), in proportions (90:5:5) by weight percentage, respectively. Everything was diluted in an organic solvent, N-Methyl-2-pyrrolidone (NMP).

The procedure to prepare the slurry was the following. At first, the LFP powder was dried in vacuum for 2h, at 110 ºC, to eliminate the humidity. After that, the LFP was mixed with the right amount of carbon black powder and the mixture was further grinded inside a ball mill for 30 minutes, at 300 rpm, to ensure a correct dispersion of the additive in the active material, which is a key feature during electrodes manufacturing [4]. At the same time, a solution of the polymeric binder (PVDF) with organic solvent (NMP) was prepared, mixing it in a magnetic stirrer. Afterwards, the grinded mixture from the ball mill containing LFP and carbon black was added. This solution was stirred for half an

hour approximately using a dispersion machine (ULTRA TURRAX ®). During the stirring process, an extra amount of solvent could be added to the solution to decrease the viscosity, since a high value can complicate the process of coating.

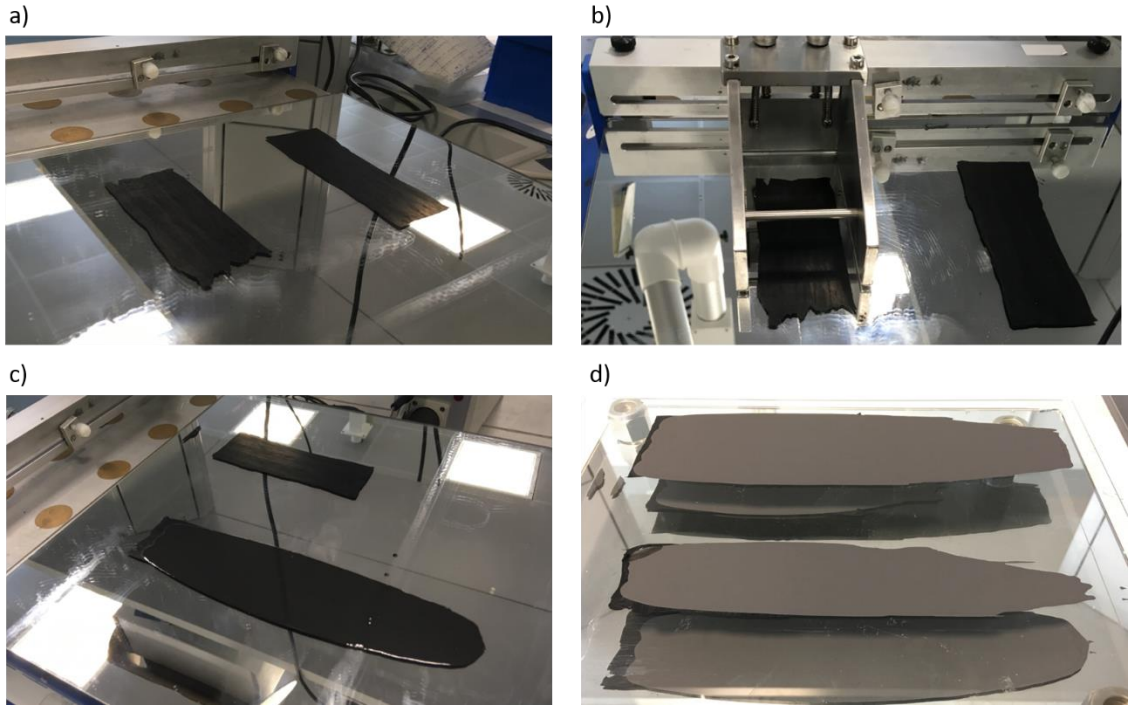

Figure 2.3: Process of dispersion of the active material slurry onto a current collector. (a) CNT mat laid onto a polished surface. (b) Dotor blade set at 150 microns of wet *thickness. (c) Humid slurry dispersed right after the movement of the blade. (d) Finished electrode after drying at 80 ºC for 12 h.*

After the preparation of the slurry, it was dispersed onto the current collectors by means of a doctor blade (see Figure 2.3), [50]. This instrument allowed to fix precisely a *wet* thickness of the coating, with a constant speed of 15 mm/s. Later, the wet electrodes were left in vacuum at room temperature for 5 h and, finally, they were dried in the same vacuum oven at 80 ºC for 12 h. Once out of the oven, each electrode was labelled, and its *dry* thickness measured manually with a micrometer. The areal density was also determined with the help of a precision balance. Table 4 summarizes the values obtained. For the sake of simplicity, from here in advance, the acronym *LFP* will be used indistinctly to refer the layer of coating of the electrode, even though it contains other components.

The reduction in thickness upon drying of the slurry film is similar in both electrodes, as expected: 69 % in the aluminum and 75 % for the CNT electrode, subtracting the thickness of the collectors (86 to 26 and 145 to 36 µm, respectively)

Table 4: Properties of manufactured electrodes. Notice that wet *and* dry *thicknesses refer to the gap set at dotor blade during dispersion and the value measured with the micrometer after drying, respectively.*

	Aluminum + LFP	**IMDEA CNT + LFP**
Label	*LFP* 002.01	*LFP* 003.03
Wet thickness (μm)	100 ± 1	150 ± 1
Dry thickness (μm)	41 ± 3	41 ± 3
Areal density (mg cm^{-2})	6.6 ± 0.2	4.6 ± 0.3
Mass loading (mg cm^{-2})	2.5 ± 0.6	4.3 ± 0.4

Figure 2.4 shows some micrographs of an analogous coating made with LTO active material instead of LFP, intended to be used in another project. The proportions of the slurry were equal, so the microstructure is representative of that of the LFP electrodes referred here.

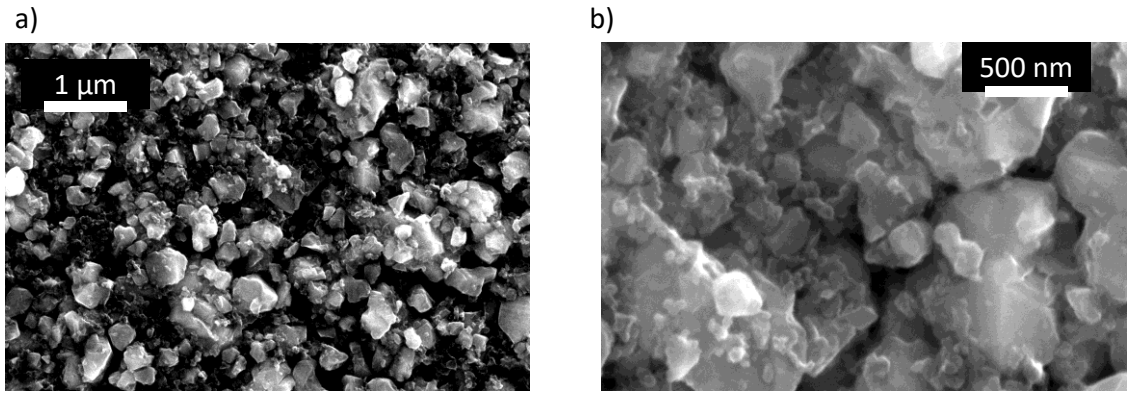

Figure 2.4: SEM micrographs of an LTO-coating on top of a CNT mat

2.3. Mechanical properties: Uniaxial Tensile Test

2.3.1. Remarks about standardized test procedures

Due to the novelty of the CNT mats being tested, it was necessary to relax the compliance with the standards of tensile testing, which are normally specific for a group of materials. Such is the case for plastics [51] or metals [52] . Some of the facts which force the procedures to disagree with the standards were the lack of typical ranges of values of maximum stress and strain, the inexistence of a well-established procedure for the preparation and manipulation of the samples of CNT mat and the limitations in terms of budget and time. This last one was perhaps the most conditioning issue, because the availability of feedstock CNT was severely constrained by the laboratory-scale

production process accessible at IMDEA Materials, something typical at the low maturity level of the technology.

In any case, being aware of the risks and implications of not using standard procedures, it was decided to carry out this way because the inaccuracies derived from that would be acceptable at the current stage of research. Nevertheless, after performing these batch of experiments, it is suggested that ISO standard for tensile testing of thin plastic films [53] serves as a suitable set of guidelines for CNT mats, when more accuracy in the numbers is needed in the future.

2.3.2. Specimen shape

An essential factor affecting the outcome of satisfactory tensile tests is the form of the specimen, represented in figure Figure 2.5.

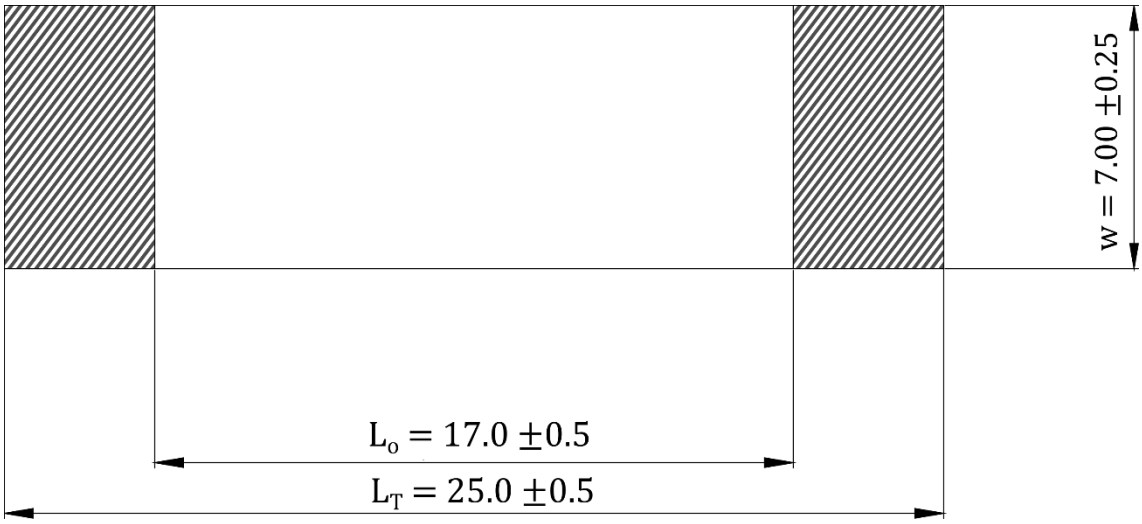

Figure 2.5: Specimen geometry. Line-pattern denotes gripped region. Units in mm.

In the case of this work, the shape did not comply with the standards. However, it was chosen due to the constraints explained in 2.3.1. A study on the dependence of the outcome of the tensile test on the specimen shape is included in Appendix A. The study conclude that the shape utilized was valid for the purpose of this dissertation.

2.3.3. Properties of interest

Besides the common material properties measured in a tensile test such as strength, strain or modulus, this section contains other properties utilized in a particular manner for this work.

Experimental error propagation for each magnitude was applied. Its development for each magnitude starting from the uncertainty of the measuring instruments can be consulted in Appendix B.

Stress, σ:

The *stress* (2.2) is the force per unit area applied perpendicularly to a section of material.

$$\sigma = \frac{F}{A_0} \tag{2.2}$$

Where,

σ is the stress, in megapascals (MPa);

F is the tensile force, measured by the load cell, in Newtons (N);

A_0 is the initial cross-sectional area of the specimen, in mm^2.

Strain, ε

$$\varepsilon = \frac{\Delta L}{L_0} \tag{2.3}$$

Where,

ε is the strain, expressed as a non-dimensional ratio;

ΔL is the elongation of the specimen measured from the beginning of the test, expressed in millimeters (mm);

L_0 is the gauge length, the longitudinal region of the specimen where the elongation is measured. It is given in (mm).

Elastic modulus, E

It accounts for the stiffness of a material. The term *elastic* accounts for the Hookean behavior that the materials commonly have at the beginning of the loading steps, when all the energy absorbed by the solid during the deformation can be elastically recovered.

$$E = \frac{d\sigma}{d\varepsilon} \tag{2.4}$$

Where,

E is the elastic modulus, given in units of stress, typically MPa or GPa;

$\frac{d\sigma}{d\varepsilon}$ is the slope of the line tangent to the initial region of the stress-strain curve;

Nevertheless, the path to obtain the elastic modulus from the raw data has been through the *elastic slope, k* (2.5), obtained through a least square fit [54] along some initial portion of the raw force-displacement curve, instead of from the stress-strain curve, which already includes uncertainties from the measurement of dimensions. Once the value of k and its uncertainty were defined, the elastic modulus E was obtained as in (2.6). The value of k was also used directly to compare samples of different materials when the dimensions of the specimens made it possible.

$$k = \frac{\Delta F}{\Delta L} \tag{2.5}$$

Where,

k is the elastic slope, expressed in N/mm;

ΔF is the increase in force measured at the sufficiently linear region chosen, in N;

ΔL is the elongation of the specimen in that region, expressed in mm.

$$E = k\frac{L_0}{A_0} \tag{2.6}$$

Where,

E is the elastic modulus, given in MPa;

k is the elastic slope, expressed in N/mm;

L_0 is the gauge length, in mm;

A_0 is the initial cross-sectional area of the specimen, in mm^2.

Tensile strength, σ_t

The tensile strength, σ_t, is the value that takes the stress when the specimen breaks under tension. From here in advance, it will be referred simply as *strength*.

$$\sigma_b = \frac{F_b}{A_0} \tag{2.7}$$

Where,

σ_b is the tensile strength, expressed in MPa;

F_b is the breaking force of the specimen, in N;

A_0 is the initial cross-sectional area of the specimen, in mm^2.

Specific strength or tenacity, σ'

The specific strength is defined as the strength divided by the volumetric density of the material (2.8). It gives an idea of how stiff a material is in relation with its weight and volume, and its formal units are m^2/s^2 or GPa cm^3/g. Alternatively, in the engineering textiles industry it is common to obtain the specific strength (or *tenacity*) of materials using the linear density of fibers because the measure of cross-sections is particularly complicated (2.9).

$$\sigma'_b = \frac{\sigma_t}{\rho} \tag{2.8}$$

Where,

σ'_b is the specific strength, formally given in m^2/s^2;

σ_b is the strength of the material, given in GPa;

ρ is the volumetric density of the specimen, given in g/cm^3.

$$\sigma'_b = \frac{F_b}{T} \tag{2.9}$$

Where,

σ'_b is the tenacity or specific strength, given in m^2/s^2 or $GPa/(g/cm^3)$;

F_b is the breaking force of the specimen, in N;

T is the linear density of the specimen along the gauge length, given in tex (grams per kilometer).

It is common to find this form of specific strength in reports about CNT yarns [55], and it was decided to use it in an analogous manner with the mats of this project. It possible to show that units are hold (2.10).

$$\frac{[N]}{\left[\frac{g}{km}\right]} \equiv \frac{[GPa]}{\left[\frac{g}{cm^3}\right]} \tag{2.10}$$

The linear density in tex of the flat 2D specimens was generated *ad hoc* as shown in equation (2.11).

$$T = \rho_a w \, x10 \tag{2.11}$$

Where,

T is the linear density of the specimen, in tex;

ρ_a is the areal density of the film, measured in mg/cm^2;

w is the width of the specimen, in mm.

Specific modulus, E'

Similarly, to what happens with the specific strength, the specific modulus can be computed in two ways, both presented in equation (2.12), each being more or less suitable depending on the available data of the specimen.

$$\mathrm{E'} = \frac{\mathrm{E}}{\rho} = \frac{\Delta F}{T\,\Delta\varepsilon} \tag{2.12}$$

Where,

E' is the specific modulus, expressed in GPa/(g/cm^3).

E is the elastic modulus, in GPa;

ρ is the volumetric density, in g/cm^3;

ΔF is the increase in force measured at the sufficiently linear region chosen, in N;

T is the linear density of the specimen, in tex;

$\Delta\varepsilon$ is the increase in strain corresponding to the Hookean region chosen.

Sliding modulus, E_S

It is only used with CNT foils because they show a secondary straight portion of the curve after the initial elastic region finishes (see Figure 2.6). The physical mechanism from which this parameter takes its name is the sliding of nanotube bundles relative to each other. It will be detailed more deeply later in the text. A concept fundamentally similar to this sliding modulus was used by Gspann et al. [56], although in that work, it was expressed as a stress obtained from the intercept of the straight line with the line of zero strain.

The sliding modulus (2.6) is obtained in a manner analogous to the elastic modulus, using the raw *sliding slope* obtained through a least-squares fit of the force-displacement curve.

$$E_s = k_s \frac{L_0}{A_0} \tag{2.13}$$

Where,

E_s is the sliding modulus, given in MPa;

k_s is the sliding slope, expressed in N/mm;

L_0 is the gauge length, in mm;

A_0 is the initial cross-sectional area of the specimen, in mm^2.

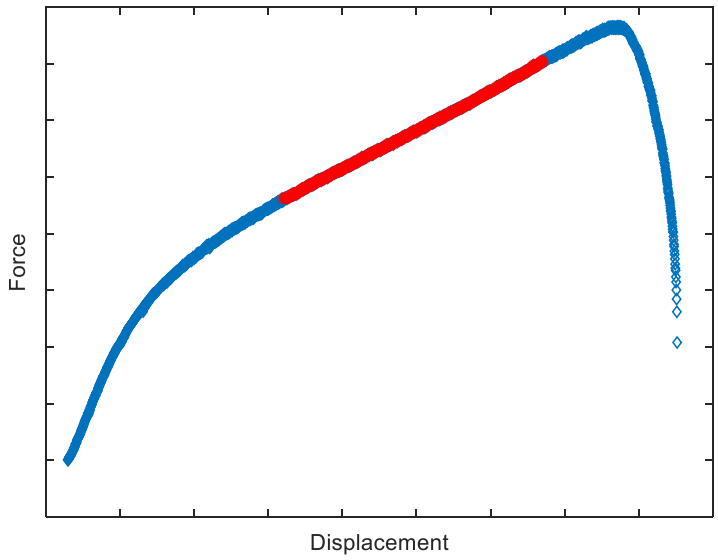

Figure 2.6:Typical Force-Displacement curve of a CNT mat. Highlighted in red is the straight portion reported as Sliding Slope *in this work.*

2.4. Electrical properties: Rate-capability test and Cyclability test

To characterize the electrical performance of the experimental CNT+LFP electrode, rate-capability and cyclability tests were performed in a coin-cell built with metal lithium as the negative electrode.

The reasons for using metal lithium as the negative electrode are its very low oxidation potential (-3.05 V/SHE, see section 1.2.1.3), which is also kept constant during charge-

discharge; and it is an infinite source of lithium-ions, so it is guaranteed that all the active material of the electrode is consumed.

2.4.1. Cell construction and materials

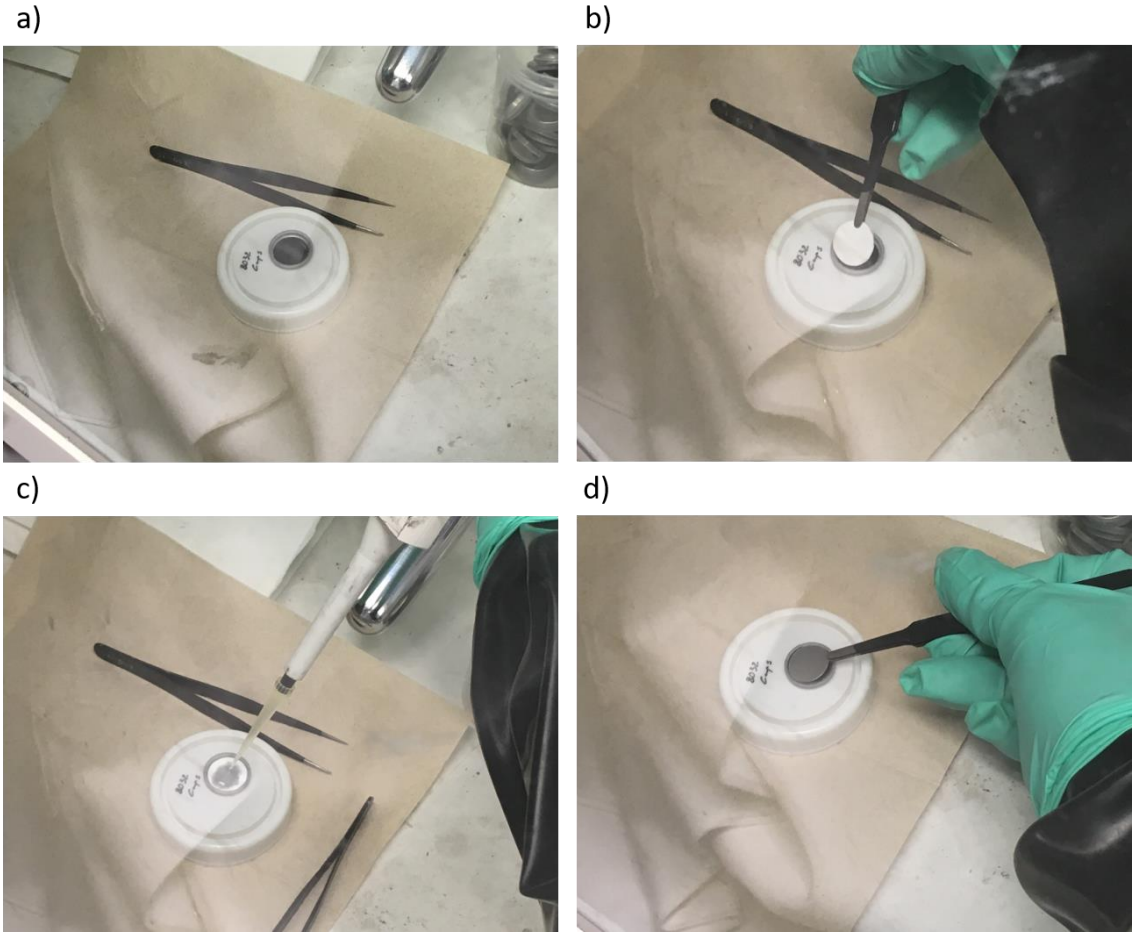

Figure 2.7: Images of some steps of the cell construction. (a) LFP electrode placed inside the coin-cap. (b) Glass fiber separator being inserted in the assembly. (c) Injection of the liquid electrolyte. (d) Closing of the cell with the external upper cover.

The procedure was the following. First, the electrodes were given the desired shape. In the case of the undeformed electrodes, circular-shaped specimens were cut by punching out of a foil of electrode (prepared as shown in 2.2.3), with the help of a press. For the deformed sample, some of the specimens' halves deformed through tensile testing were selected and cut out of the cardboard support manually with scissors. After that, in inert atmosphere, the electrodes were weighted with a balance to determine the mass of active material. Next, they were placed inside a "coin-cap" (Figure 2.7-a), where 300 µL of liquid electrolyte were added (Figure 2.7-c), together with the separator (Figure 2.7-b). Following that, the lithium metal negative electrode was placed inside the coin cap, and the rest of the casing components were assembled: a 0.5 mm flat spacer, a wave-spacer

and the final lid (Figure 2.7-d), in that order. To finish the process, the whole cell was crimped at 100 kg/cm^2 to ensure correct sealing and electric contact between the components.

Some relevant characteristics of the coin cell are the cell dimensions, the electrolyte and the separator. The cell is of type LIR 2032. The liquid electrolyte is a commercially available solution produced by Solvionics, a 1 M solution of $LiPF_6$ using 1:1 (by volume) Ethylcarbonate-Diethylcarbonate (EC-DEC) as solvent [57]. The separator is a glass-fiber filter Whatman® GF/D.

2.4.2. Electrical measurements

LFP versus metal lithium half-cells were tested initially in a galvanostatic cycler for 5 cycles at C/10 to check its correct functionality. Figure 2.8-a shows an image of some cells connected simultaneously to different channels of the apparatus. The average level of charge obtained during this initial test was set as the nominal capacity of the electrode.

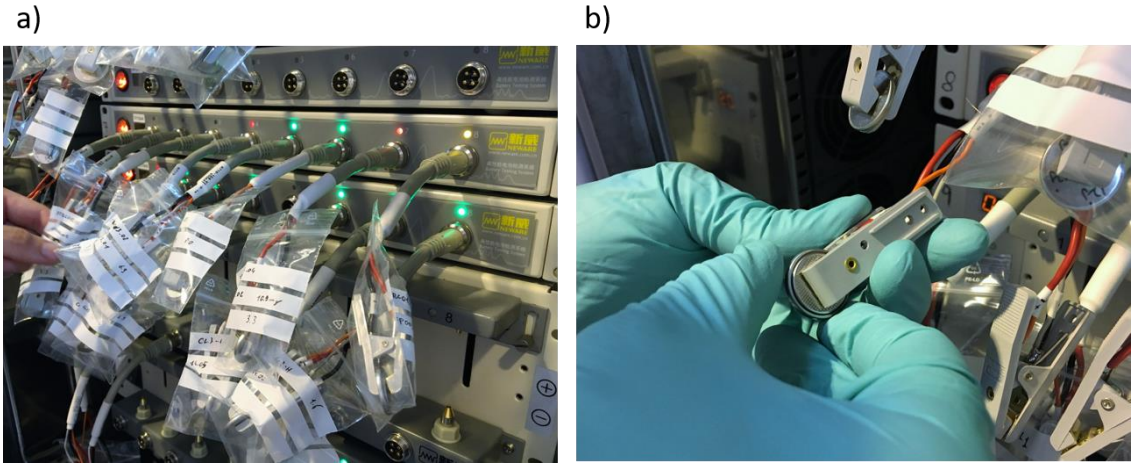

Figure 2.8: Images of the setup used at the multichannel galvanostat. (a) Multiple cells connected to different channels. (b) Detail of a coin cell being pluged to the terminals of a channel.

After the initial test, two other kinds of test were carried out without disconnecting the coin batteries from the cycler. The first one, called *rate-capability test*, subjects the electrode to several charge-discharge cycles at different C-rates with the aim of evaluating the charge-storing capability of the electrode at different current densities. More specifically, the coin-cell underwent 5 charge-discharge cycles at each of these C-rates: C/5, C/2, 1C and 3C. After that, another 5 cycles at C/10 were performed again, to check for any capacity irreversible losses that could have appeared [4].

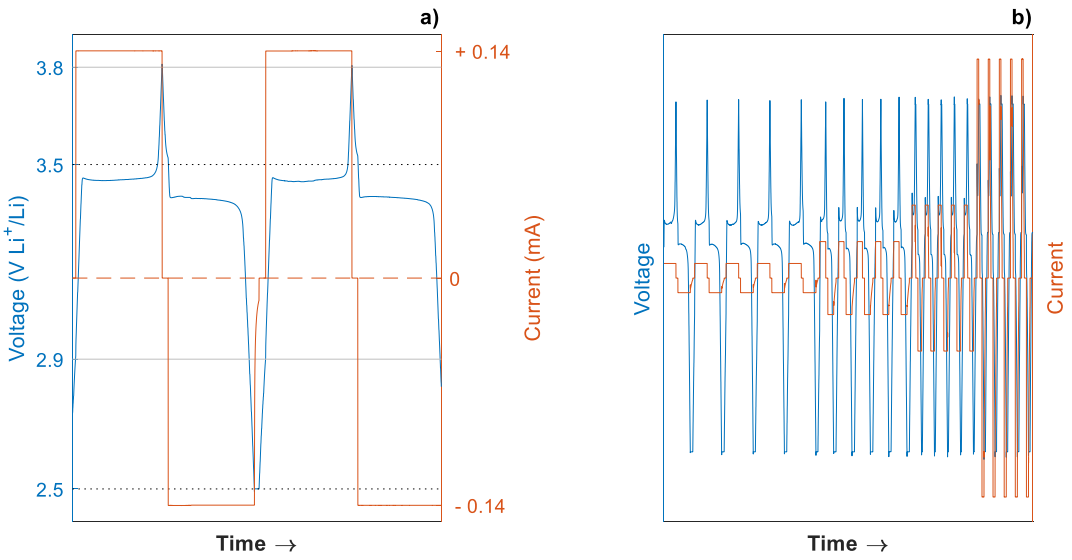

Figure 2.9: Voltage and current time profiles. (a) Initial testing, 2nd and 3rd cycles at C/10. The solid line delimits cut-off voltages during charging; the dotted-line, during discharging. (b) Rate capability test. Cycles at C/5, C/2, 1C or 3C, chronologically. Notice the decrease in cycle time at higher C-rates.

After those 25 cycles had been performed successfully, the same setup was leveraged to carry out a *cyclability test*. This means that the cells were repeatedly submitted to charge-discharge cycles at C/2 to get an insight to the long-term evolution of the battery. The effects of the aging can be quantified by the SOH, presented in section 1.2.1.3.

The charge-discharge procedure followed for each cycle was the constant current-constant voltage protocol (CCCV). The desired current (dictated by the C-rate) was fixed between two cut-off voltages, different for the charge and discharge phases (Figure 2.9-a). Once those voltages were reached, they were fixed as constant and the current flow thus adapted by decreasing until its magnitude was 1/10 of the initial value. Then, after a fixed idle period, the next charge-discharge phase began until the corresponding cut-off voltage was reached, and so on.

The values for the cut-off potentials were fixed taken as reference the values found in literature for a graphite-LFP cell, which were 3.7 and 2.0 V [5]. They correspond to 4.0 and 2.3 V vs. Li^+/Li at the cathode, subtracting the redox potential of graphite. Thus, it leaving a safety margin of 200 mV, the cut-off voltages were fixed at 3.8 and 2.5 V vs. Li^+/Li for the initialization of the cells. However, it was decided to raise the discharge cut-off to 2.8 and 3.0 V for the rate-capability and cyclability tests, respectively, to prevent accelerated aging due to large DOD.

3. MECHANICAL PERFORMANCE

3.1. Results

3.1.1. Introduction and remarks about data treatment.

The results presented in this section were obtained along a three-month period in the IMDEA Materials laboratories. Two different testing machines were used because of the availability during that period.

Some initial parts of the force-displacement curves from the machines were truncated during post-processing according to standard ASTM D638-02a [58] to correct for imperfections during initial loading (see Figure 3.1).

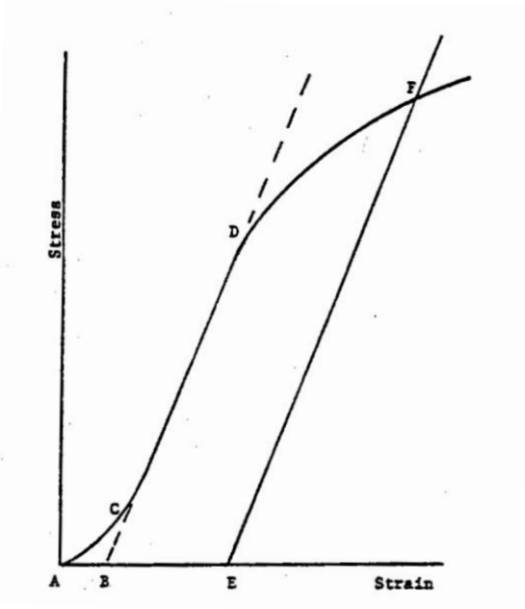

Figure 3.1: Toe-compensation *of the stress-strain curve. Analogous to the force-displacement plot. [58]*

3.1.2. Metallic foils

As a way to set up a baseline for the newly developed electrodes based on CNT mats, existing current collector foils of Aluminum and Copper were tested. The samples were prepared with the same method as the CNT mats: cut manually with a knife using a paper template fixed on top of the foil.

Figure 3.2 shows the stress-strain curves of the Aluminum and Copper samples. In the case of these metallic materials, the measurements of thickness were consistent, so the stress plotted can be accepted as a meaningful figure.

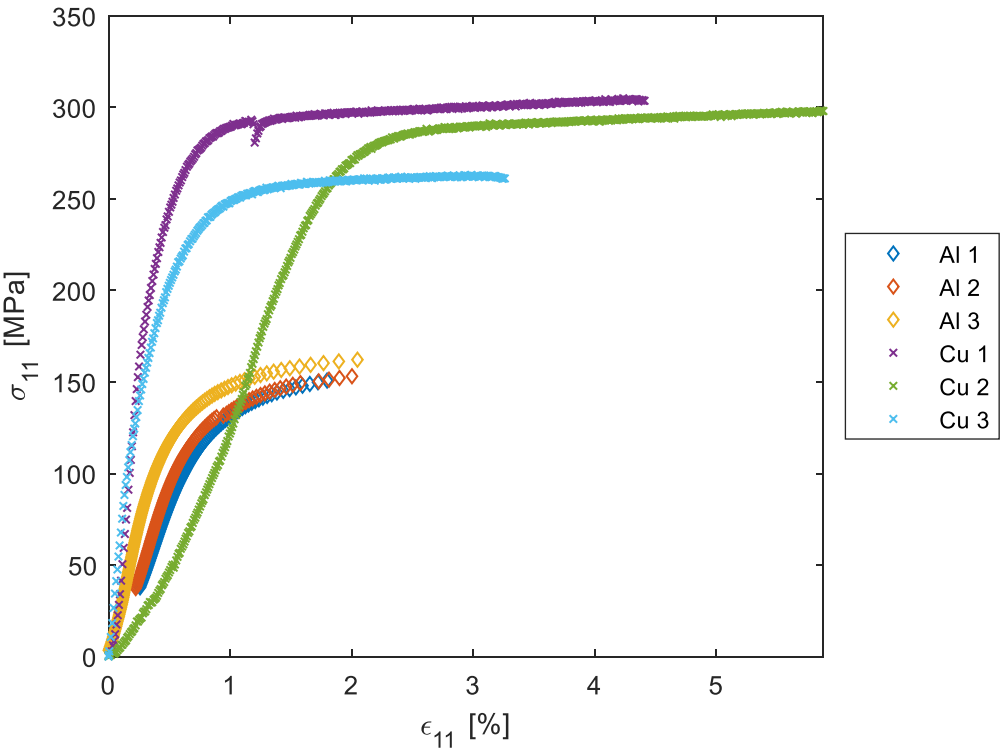

Figure 3.2: Longitudinal stress-strain curves of the metallic foils tested

In Table 5 the properties derived from the curves are summarized. It must be pointed out that specimen *Cu 2* was discarded in the calculations of modulus and strain. From the plot in Figure 3.2 one can see that its loading process at the beginning of the test-run was not satisfactory.

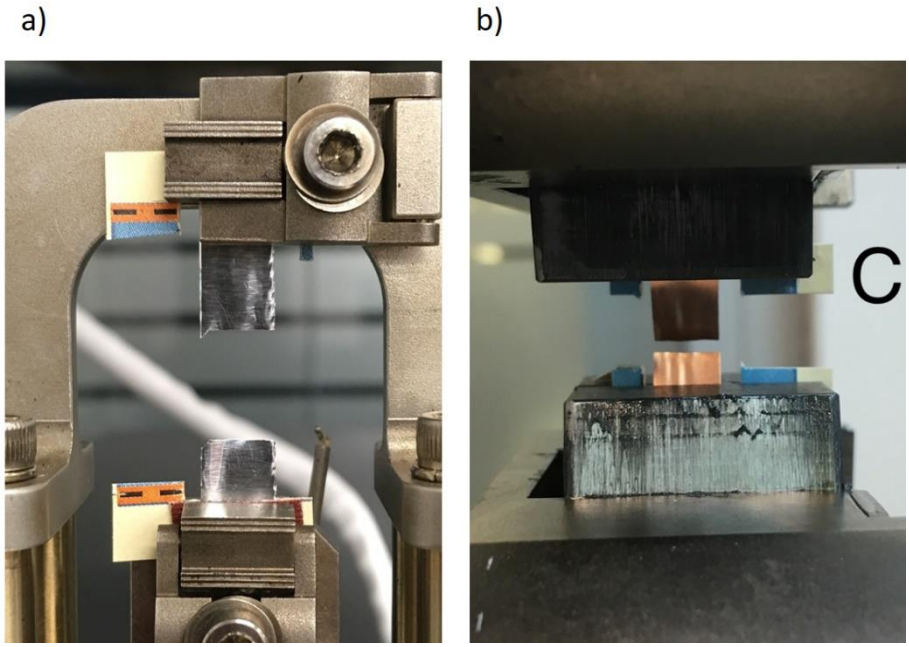

Figure 3.3: Tensile test specimens, right after breakage. (a) Aluminum (b) Copper.

The specimens broke in a region well within the gauge length (Figure 3.3). This was considered as a success given their rectangular shape, which could have led to the appearance of fracture at the grips.

Table 5: Properties of Aluminum and Copper foil tested. Specimen Cu 2 was only included in the tensile strength calculation:

	$\boldsymbol{Al}$	$\boldsymbol{Cu}$
$Strain\ at\ break, \varepsilon_b(\%)$	1.95 ± 0.16	3.8 ± 0.7
$Tensile\ strength, \sigma_b(MPa)$	156 ± 20	287 ± 56
$Elastic\ Modulus, E\ (GPa)$	23 ± 7	75 ± 19
$Specific\ strength, \sigma_b' \left(MPa \left(\frac{g}{cm^3}\right)^{-1}\right)$	58 ± 9	35 ± 6
$Specific\ modulus, E' \left(GPa \left(\frac{g}{cm^3}\right)^{-1}\right)$	9 ± 3	9 ± 2

A first glance at the obtained properties suggests several ideas. Comparing aluminum properties with typical values of literature for an aluminum alloy specially dedicated for electrical conductors such as Al 1350 [59] , the tensile strength figure seems to be in good agreement. However, the modulus of elasticity and the strain at break are far from the typical values, being both well below 69 GPa [60] and 11% [59], respectively.

The 5 times lower strain at break with respect to a cold-worked high-purity Al 1080 sheet could be explained by the assumption of strong residual stresses present in a foil of such reduced thickness (15 μm), consequence of an intensive cold-work reduction. Another condition that favors such a low deformation can be the use of the force-controlled DMA machine to perform the test. This apparatus works by subjecting the sample to a force which increases at a constant rate. The result, when testing a material with a plastic region, is that as the material enters that zone of the curve, the slope is reduced and, therefore, the strain-rate increases to maintain the constant-rate increase of the force. This phenomenon can be observed in the increased spacing between points of the aluminum curves in Figure 3.2. Its effect gets extremely noticeable as the slope approaches zero because the strain-rate is, hence, infinitely increased, what reduces the maximum allowable strain. The fact that the tensile strength obtained here (156 MPa) is larger than the largest tensile strength reported in [59] for the aforementioned Al 1080 sheet (135 MPa) is in line with both hypotheses.

As opposed to that, the elastic modulus is one third of the one present in literature. It is believed that this can be a consequence of working in force ranges close to the limit of the machine, what could have made the compliance of the apparatus to become important. The average breaking force for the aluminum samples was 16.7 N while the limit of the load cell is 18 N. In any case, although the result for the modulus should not be considered as acceptable in absolute terms, it will be useful to establish later a comparison with LFP covered specimens tested in the same machine.

Properties of copper are also compared with the handbook values. Again, the tensile strength seems in good agreement with the expected quantities. For a strip of an oxygen-free, high conductivity copper, of high purity (Cu 99.95%+), as the standard UNE-EN 1978:1998 for copper cathodes dictates [16], the tensile strength can be as high as 314 MPa for a cold-rolled material. This falls within the uncertainty window of our data. On the other hand, and equally as with aluminum, the reported modulus and elongation at break (117 GPa and 16%) [59] are not as close to the obtained results, although they are closer than the in the aluminum sample.

To explain the 4 times lower strain at break the same argument of extensive cold-rolling as for the aluminum foil is proposed, as this is an even thinner sheet of copper (10 µm). However, this sample was tested in a displacement-controlled machine (as it can be observed in the spacing in the points of the copper sample curves), so the issue with the increased strain-rate was not a problem. It is believed that some damage may have been induced in the edges of the specimens during the manual cutting process. Those edges could be already deformed at some strains prior to the test, what could lead to the early appearance of cracks with the corresponding stress concentration and early failure. This is a hypothesis that applies also to the aluminum sample and, in fact, the kind of damage described here can be observed at the edges of the aluminum sample pictured in Figure 3.3-a.

In the case of copper, the situation with the machine was diametrically opposed to the aluminum test: the range of working forces was far from the limits of the apparatus: average breaking force of 21.3 N, with a load cell of 500 N mounted on an Instron machine rated for 10 kN. Therefore, the discrepancy in the obtained copper modulus and the literature values was much smaller. The obtained number is approx. two thirds of the handbook value, while for aluminum was one third. It is concluded that an initial

misalignment could have caused the initial displacement of the copper to be slightly distorted, even with the toe region compensated.

3.1.3. CNT mat

The standalone CNT mat was tested in the displacement-controlled 10 kN Instron machine with the load cell of 500 N. This kind of mat had never been tested in the institute before, so the procedure was not fully clear. Besides, the sample size was limited, as explained in 2.3.1. Therefore, in parallel to the testing of the CNTs from IMDEA, an attempt to reproduce the results of a publication on a commercial CNT mat was performed [14]. The same direct-spun CNT mat of that publication, produced by Tortech Nano Fibers Ltd, was tested to address the suitability of our procedure to CNT mats. Figure 3.4 show the stress-strain plots for the sample of Tortech and IMDEA CNT mats, respectively, while Table 6 summarizes the properties.

Regarding the Tortech CNT, the dispersion in the data is quite significant, as shown in Figure 3.4.a. Therefore, a sample size of 9 specimens was used to obtain a result statistically significant. The comparison with the baseline paper is acceptable. The strain at break in this work ranges from 9 to 19% approximately, while in [14] is reported to be between 20 and 30%. The strength here is bounded between 37 and 67 MPa, which is a bit higher than the 30-40 MPa range of the reference; and the elastic modulus looks also in an acceptable range, between 0.6 and 1.7 GPa and about 0.5 GPa in [14] (estimation made from visual inspection of plots in figure 7a of this reference).

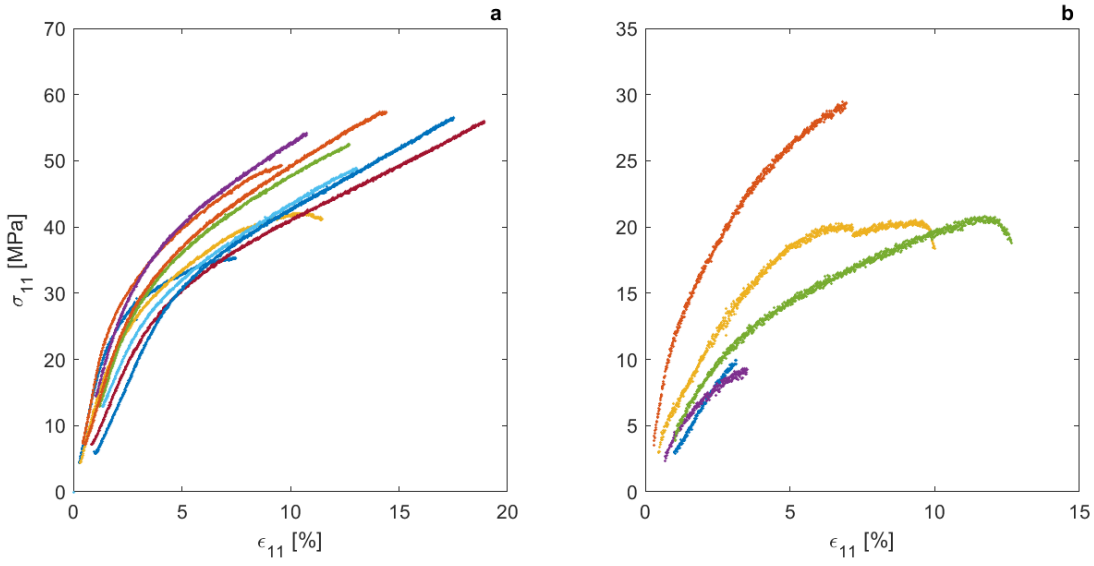

Figure 3.4: Stress-strain curves of the CNT mats. Tortech (a) and IMDEA (b).

Altogether, the reduced strain at break and increased strength and modulus seem to be linked with the type of grips and the low aspect ratio of the specimen shape utilized in this study. While the roller grips of the baseline paper allow the specimen to deform more freely, the pressure grips of this work, and specially with such a low aspect ratio, constrain the transverse deformation of the sample by hindering the micro-wrinkling of the strip in in that direction. The lack of this mechanism reported in Stallard et al., limits the deformability of the sample and makes it stiffer. Nevertheless, despite the non-ideal shape of the specimen, Figure 3.5 shows that the fracture region was located close to the middle of the gauge length. Altogether, the similarities allow to conclude that the procedure is valid.

Table 6: Summary of mechanical properties of CNT mats tested.

	Tortech CNT	***Imdea CNT***
$Strain\ at\ break, \varepsilon_b(\%)$	14 ± 5	9 ± 2
$Tensile\ strength, \sigma_b(MPa)$	52 ± 15	33 ± 25
$Elastic\ Modulus, E\ (MPa)$	1159 ± 527	833 ± 755
$Specific\ strength, \sigma_b' \left(MPa\ \left(\frac{g}{cm^3}\right)^{-1}\right)$	137 ± 43	57 ± 34
$Specific\ modulus, E' \left(MPa\ \left(\frac{g}{cm^3}\right)^{-1}\right)$	3065 ± 1454	1439 ± 1089
$Elastic\ slope, k\ (N\ mm^{-1})$	4.8 ± 1.4	1.7 ± 0.8
$Sliding\ modulus, E_S(MPa)$	190 ± 44	144 ± 117
$Sliding\ slope, k_S(N\ mm^{-1})$	0.78 ± 0.05	0.30 ± 0.10

The test of the Tortech mat gave more information on the mechanics of the microstructure of a CNT mat. While in the case of the elastic region the standard deviation is, after the least squares fit, 29% of the average, it is only 6% for the same figure in the sliding slope (defined in equation (2.13)). This difference is in line with the reported mechanisms of deformation of CNT mats. During the elastic regime, the nanotube bundles, initially randomly tangled, are progressively untangled and aligned. Once they are sufficiently aligned, the bundles themselves are able to withstand higher load. It is in this moment when the mechanism of deformation switches to the sliding of CNTs between each other within each bundle, and between bundles, as the shear strength of the van-der-Waals bonds between them is weaker than the covalent bonds along each CNT

(see section 1.2.2.2). This longitudinal shear deformation is why this portion of the curve has been indicated as *sliding slope.*

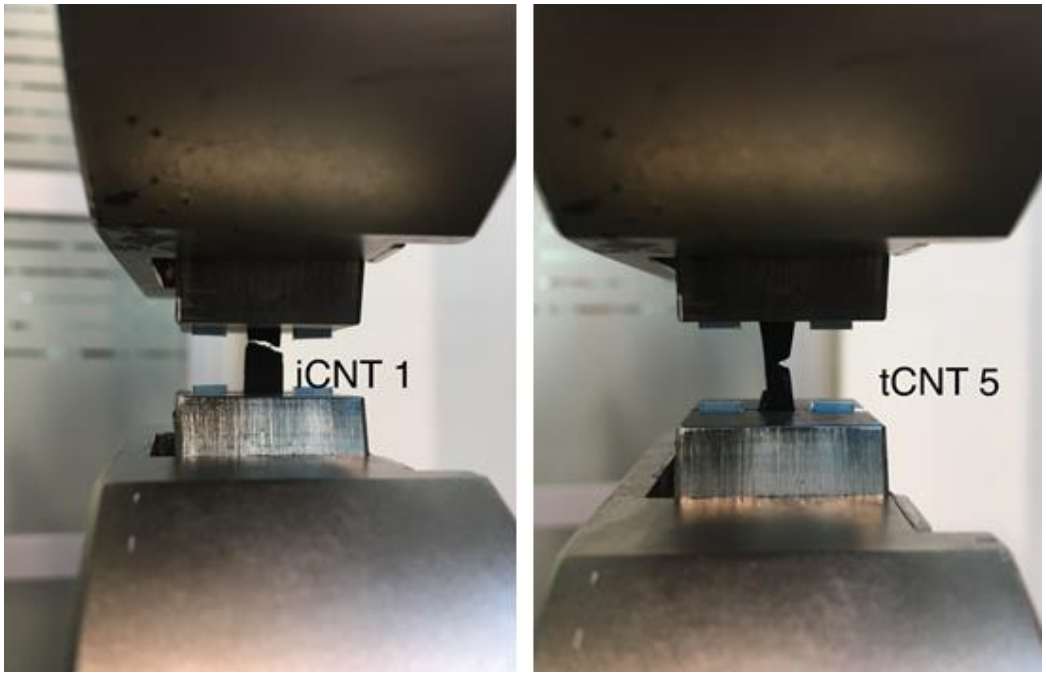

Figure 3.5: CNT mat specimens captured right after breakage. (Left) Imdea CNT, specimen 1. (Right) Tortech CNT, specimen 5.

The fact that its spread among the sample is lower than that of the elastic slope is consistent: once the bundles are more aligned, the randomness of the outcome is lower because the behavior is dominated by the shear strength of the CNT-to-CNT and bundle-to-bundle bonds, a property intrinsic to the material, instead of the degree of alignment of the tubes, which varies from specimen to specimen.

Regarding the Imdea CNT, the results cannot be considered very satisfactory, especially in terms of uncertainty (see Table 6). A sample of only 5 specimens is plotted in Figure 3.4.b. Two of the five specimens plotted presented evidences of flaws that hindered their performance noticeably (curves that end before the 5% strain). Those two have been excluded from the values of strength and strain at break. Only the initial part of their curves has been considered to obtain the modulus.

The main source of uncertainty in the results was the thickness value of the mat, which could not be measured appropriately, as exposed in section 2.2.1. Its 40% uncertainty is propagated through all the associated quantities (strength and elastic modulus) and, combined with the standard deviation of the forces measured, gives high total uncertainty (75% for the strength and 91% for the modulus). At the same time, the numbers for the

specific quantities have less uncertainty (60 and 76% for strength and modulus, respectively) since the measurement of the areal density is less problematic than the thickness, although they are still very high due to the high spread in the values.

Despite the problems, numbers obtained are on the order of the commercial mat, even with the improvable quality of the laboratory mat utilized. With all its lack of accuracy, these results are accepted as a very rough baseline, provided that the main topic of the work is not the characterization of the standalone CNT mats, but them coated, what is introduced in the following section.

3.1.4. Coated electrodes

The results for two kinds of electrodes are presented here. Both have a layer of active LFP coating produced at the same time from the same slurry (see section 2.2.3 for details), but they differ in the material of the substrate: one uses aluminum foil; the other, CNT mat manufactured by IMDEA. The objective was to understand the differences in the coating adhesion between the aluminum and the CNTs, and its consequences in the mechanical properties.

Table 7 summarizes the values obtained for the properties of interest, whereas Figure 3.6 shows the plots of normalized force (per unit width) versus strain. Normalized force is used instead of stress since the role of the coating layer in carrying the load is not clear. The thickness of this layer affects the values of stress and modulus, lowering them with respect to the bare aluminum of CNTs. Considering the stress as the main parameter implicitly assumes that the ceramic coating is sharing some of the load with the aluminum or CNT support, which is a non-trivial hypothesis. Hence the utilization of normalized force as the characterizing parameter, which allows to establish a direct comparison with the uncoated materials and determine the role of the coating.

The data of the two materials show different degree of spread. The standard deviation of the elastic slope, k, was of 12% for the metal, and 32% for the nanotubes. Very similar numbers were found in the normalized breaking force, with 14% of deviation in the aluminum sample and 33% among the CNTs specimens. As it is reasonable, the specimens of aluminum behaved in a more constant manner than the electrodes based on CNTs.

Table 7: Mechanical properties and some testing conditions of electrode films.

	Al + LFP	***CNT + LFP***
$\varepsilon_b(\%)$	1.0 ± 0.4	13 ± 6
$\sigma_b(MPa)$	54 ± 18	15 ± 6
$E\ (MPa)$	12805 ± 4794	1285 ± 574
$\sigma_b' \left(MPa \left(\frac{g}{cm^3}\right)^{-1}\right)$	34 ± 6	13 ± 5
$E' \left(MPa \left(\frac{g}{cm^3}\right)^{-1}\right)$	8016 ± 1744	1141 ± 512
$k\ (N\ mm^{-1})$	218 ± 26	22 ± 7
Mass fraction, $\frac{m_{coating}}{m_T}$	0.38 ± 0.10	0.93 ± 0.15
Machine used (Name/Load cell)	DMA/18N	Instron/ 500N
Test method	Force-controlled	Displacement-controlled

It must be pointed out that the aluminum with LFP electrode was tested with the same force-controlled machine as the bare aluminum foil, despite the drawbacks due to the strain-rate control explained earlier in section 3.1.2, as a way to ensure the comparability of the results between the coated and the uncoated metallic foil.

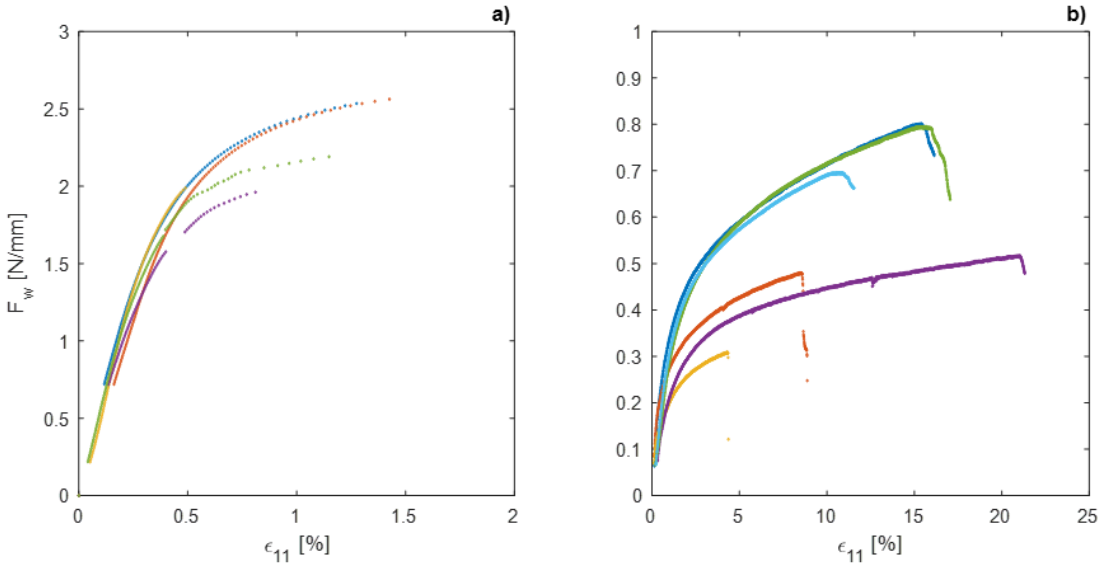

Figure 3.6: Normalized force vs. strain plots for four different types of electrode. (a) Aluminum + LFP. (b) IMDEA CNT + LFP

Regarding the CNT-based electrode, the piece of CNT mat used as substrate came from the same batch as the reported standalone IMDEA CNT strips of previous section also to ensure comparability.

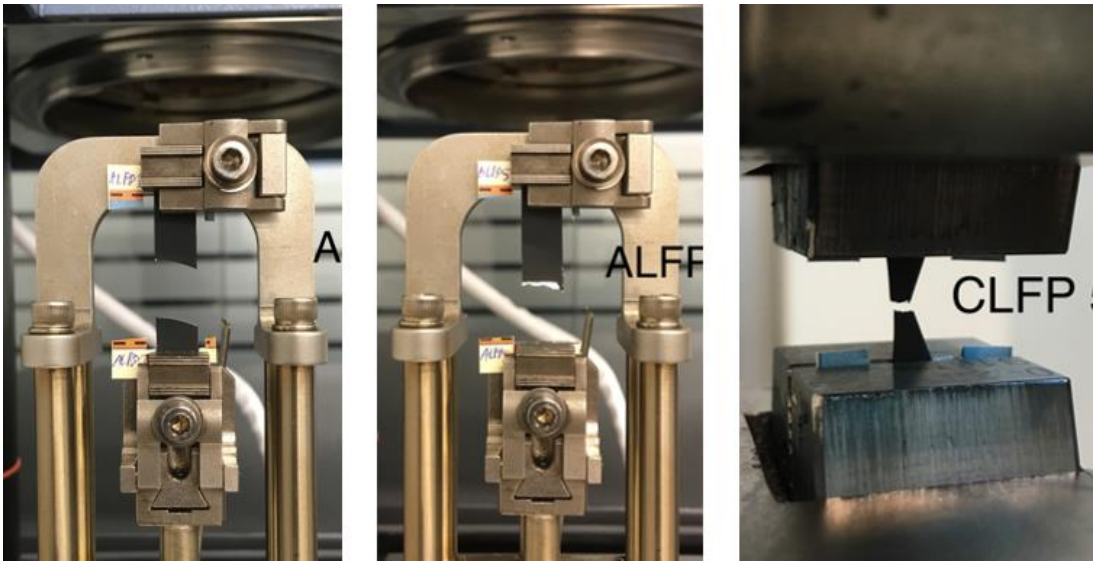

Figure 3.7: LFP coated electrodes after breakage during tensile testing. (Left) Aluminum with LFP, specimen 2. (Middle) Aluminum with LFP, specimen 4. (Right) CNT + LFP, specimen 5

In Figure 3.7 the fracture lines of some specimens of both types of electrode can be observed. Due to the rectangular shape of the specimens, the fracture not always appeared at the middle of the gauge length, as desired, (like in Figure 3.7-l and -r), but close to the grips region (Figure 3.7-m). Those runs were also considered as satisfactory when the force-displacement curve obtained was comparable to that of the specimens with the ideal fracture location.

3.2. Discussion

The effect of the coating was analyzed through samples prepared from the same batches of bare material, which is especially important for a laboratory-made material such as the CNT mat. Also, the testing conditions were kept unaltered from the setup used for each uncoated material to the samples with LFP on top. This means that the same machine (Force-controlled DMA for Aluminum, Displacement-controlled Instron for CNTs), the same specimen shape and the same testing speed (3 N/min for Aluminum, 1 mm/min for the CNT mat) were used for the plain foils and the coated strips.

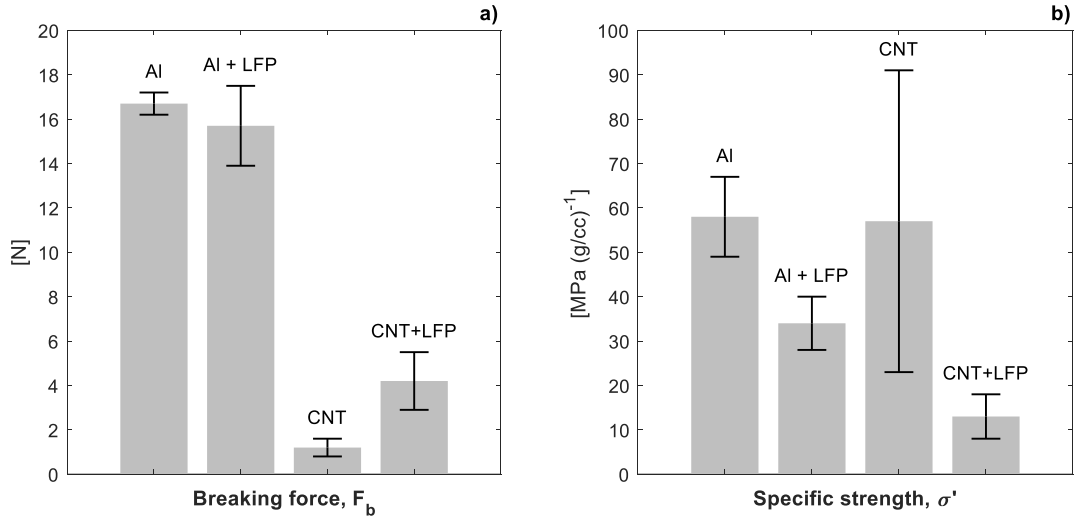

Figure 3.8: Comparison of breaking force (a) and specific strength (b) of coated and uncoated materials.

We shall begin the comparison with the data for breaking force and specific strength, summarized in Figure 3.8. It is worth noting that the regular or *geometrical* stress based on cross section (2.2) is not used in this discussion because, as explained at the beginning of section 3.1.4, the role of the coating layer in carrying load is not clear, so the complete cross section shall not be used *a priori*. Instead, as the specimen geometry is the same in all samples, it is possible to use the total breaking force (Figure 3.8.a) to understand if, in absolute terms, the addition of the active slurry modifies the load bearing capacity of the strips.

Independently of the influence of the coating, it is interesting to observe that, though with a very big uncertainty, the bare CNT mat looks already in the range of values of the specific strength of aluminum. This is interesting because a lot of effort has been made by the research community to transfer the outstanding specific properties of the CNTs in the nanoscale to bigger formats. The specific strength of this semi-industrial CNT mat, whose properties are not specifically oriented to the structural function, is already comparable to such a widely used structural metal as aluminum.

Regarding the coating effects, from the same plot it is possible to conclude a remarkable increase in the breaking force (+270%) of the CNT mat when coated with LFP ($1.16 \pm 31\%$ to $4.2 \pm 30\%\ N$). It is also interesting to notice that the relative dispersion of the figure remains constant at 30%. Opposite to that, there is a decrease in the average value for the breaking force of the aluminum foil (16.7 to 15.7 N). However,

this lowering is relatively much smaller (-6%) and, from direct observation of the plot it is possible to see that the value of the aluminum foil falls within the uncertainty window of the coated sample. Therefore, it is concluded that the coating has no effect in the breaking load for the metallic material.

In terms of specific strength (Figure 3.8-b), it is important to have in mind the areal densities of the coated materials since they are used to divide the recorded force, (equations (2.9) and (2.11)). They can be consulted in Table 4.

The difference in values of specific strength between coated and uncoated aluminum seems reasonable to be explained entirely by the increase in weight, given that it was earlier concluded that no effect in the total breaking load was present.

The situation is different for the CNTs. The increase in breaking force is not enough to balance the extra mass added to the structure. This result is no surprise because, even if the layer of active coating is able to improve the load carrying capabilities of the CNT mat, it is not intrinsically an efficient structural material, so it is logical that its mass does not contribute positively to the specific strength. Nevertheless, it is remarkable that the value of this magnitude for the uncoated CNTs is *only* 338% bigger than in the coated electrode given the increase in 1430 % in areal density due to the coating. This suggests that the coating is effectively reinforcing the material; and that it may be possible to find a specific mass fraction in which the specific strength remained equal to that of the CNT mat.

$$\sigma'_{ALFP} \propto \frac{F}{\rho_{a_{Al}} + \rho_{a_{LFP}}} = \frac{16.2}{4.1 + \rho_{a_{LFP}}}, 0 \leq \rho_{a_{LFP}} \tag{3.1}$$

$$\sigma'_{CLFP} \propto \frac{F(\rho_{a_{LFP}})}{\rho_{a_{CNT}} + \rho_{a_{LFP}}} = \frac{1.16 + 0.71\,\rho_{a_{LFP}}}{0.3 + \rho_{a_{LFP}}}, \quad 0 \leq \rho_{a_{LFP}} \tag{3.2}$$

$$\sigma'_{CLFP} \propto \begin{cases} \dfrac{1.16 + m\,\rho_{a_{LFP}}}{0.3 + \rho_{a_{LFP}}} & 0 \leq \rho_{a_{LFP}} \leq A \\ \dfrac{1.16 + m\,A}{0.3 + \rho_{a_{LFP}}} & A \leq \rho_{a_{LFP}} \end{cases}, \quad m > 0.71 \tag{3.3}$$

Despite the existing difference in LFP relative content, it is possible to extract conclusions from the comparison between the aluminum and the CNT electrodes. Linear fitting laws are proposed for the value of the specific strength as a function of the areal density (notice that the linear density in tex is directly proportional to the areal density). Thus, for the aluminum model (eq. (3.1)) it is assumed that no reinforcement effect is

caused by the LFP coating. The value of the breakage force is, then, the average between the plain foil and the coated one.

For the CNT mat it is assumed that the breaking force does increase with the LFP content linearly. This is a very rough assumption, but it will work to illustrate the concept. The values for the slope and the y-intercept have been obtained from the comparison of the bare CNT mat with the coated specimens (eq. (3.2)). Finally, another hypothesis is thrown: the breaking load depends on the content of LFP with a steeper slope up to a value A, from which the breaking load stops increasing (equation (3.3)). This hypothesis contemplates that the reinforcement effect of the coating stops increasing when a certain mass fraction is reached.

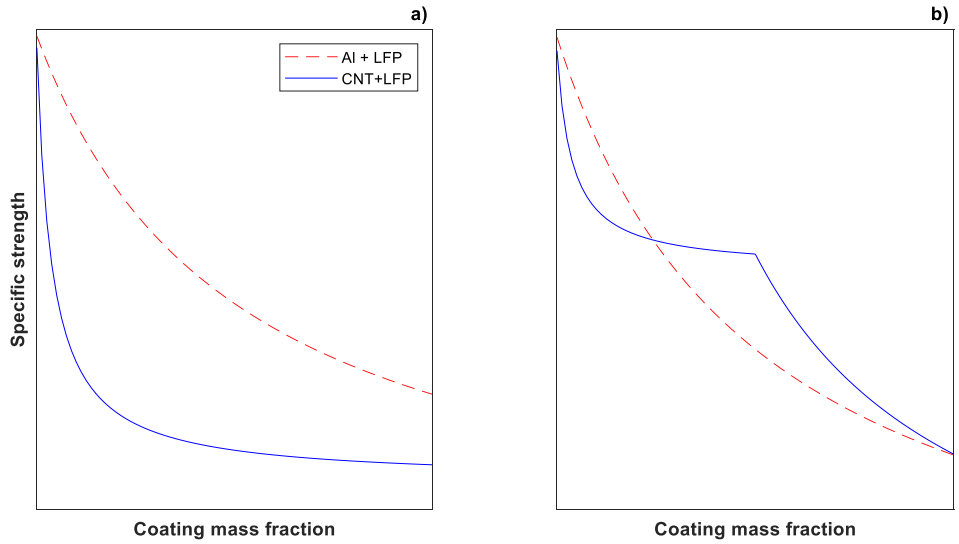

Figure 3.9: Different outcomes for the specific strength behavior depending on different hypotheses.(a) (3.1) vs. (3.2). (b) (3.1) vs. (3.3), with m=2.5 N cm^2/mg and A=4 mg/cm^2.

Two possible outcomes for the evolution of the specific strength as a coating mass loading are showed in Figure 3.9. The curves in a) represent the functions proposed in (3.1) and (3.2), whereas the plot in b) shows a comparison of (3.1) and (3.3). Looking at the plots it is possible to conclude that, in the case that a simple linear relation is present, the specific strength of the CNT electrode could never match the one of the aluminum, as the load bearing capabilities per unit mass of the coating are not good. However, there are evidences to believe that the reinforcement mechanism that the coating exerts on the CNT mat is linked to some level of infiltration of the slurry into the bundle network.

The infiltration could have two consequences in the mat. On the one hand, it could increase the friction between the nanotube bundles and between yarns, what would

increase the bulk strength of the mat [56]. Another hypothesis is that the infiltration of the polymeric binder in the porous mat could also enhance its strength and stiffness, acting as the matrix of a composite. This is the phenomenon observed in a publication by Mas et. al, where CNT fibers are infiltrated with a small mass content of epoxy (5 %wt) [61].

The situation is very much like the one with the PVDF here, since the total polymer weight content of the electrode is 4.65 %. The particularity of this infiltration is that, unlike regular carbon fibers, the high-porosity of CNTs allows the polymer molecules to fill the fibers, and not only the gaps between them. This creates an additional stress-transfer mechanism resulting in a net increase of the specific stress. Nonetheless, once the fibers are "full" and the additional polymer content goes to the surrounding areas, the reinforcement effect starts to evolve like in a traditional composite. This trend is depicted clearly in Figure 3.10.

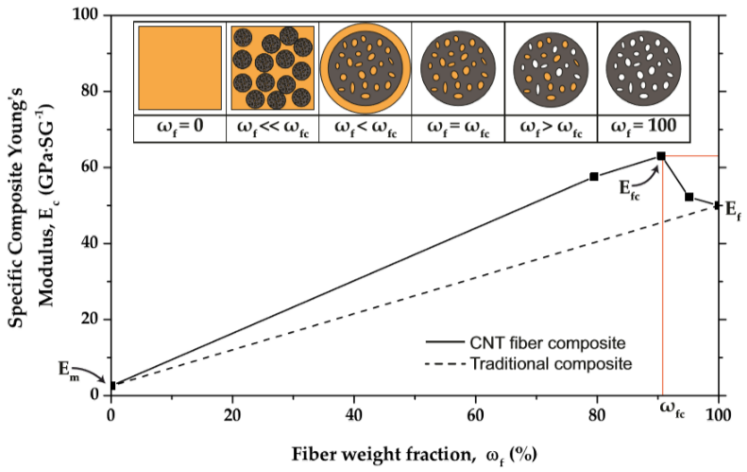

Figure 3.10:Plot of Young's modulus of an epoxy-CNT fiber film composite against polymer mass fraction. The dashed line shows the rule of mixtures of traditional composites. Reproduced from [61].

Regarding the LFP coating studied here, it is reasonable to expect that the reinforcing effect for higher coating mass fractions would stop increasing when reaching a threshold value, in both hypotheses. In the case of the augmented friction hypothesis, not all the thickness of added coating would be able to infiltrate and contribute to that effect, whereas for the effective polymer matrix, even if all the PVDF-binder was transferred to the CNT mat, there would exist a point in which the fibers would be full, and no more net reinforcing would occur.

The evidences which suggest that the more complex hypothesis (3.3) is closer to reality come from observations performed by SEM micrography of fractured CNT-LFP specimens.

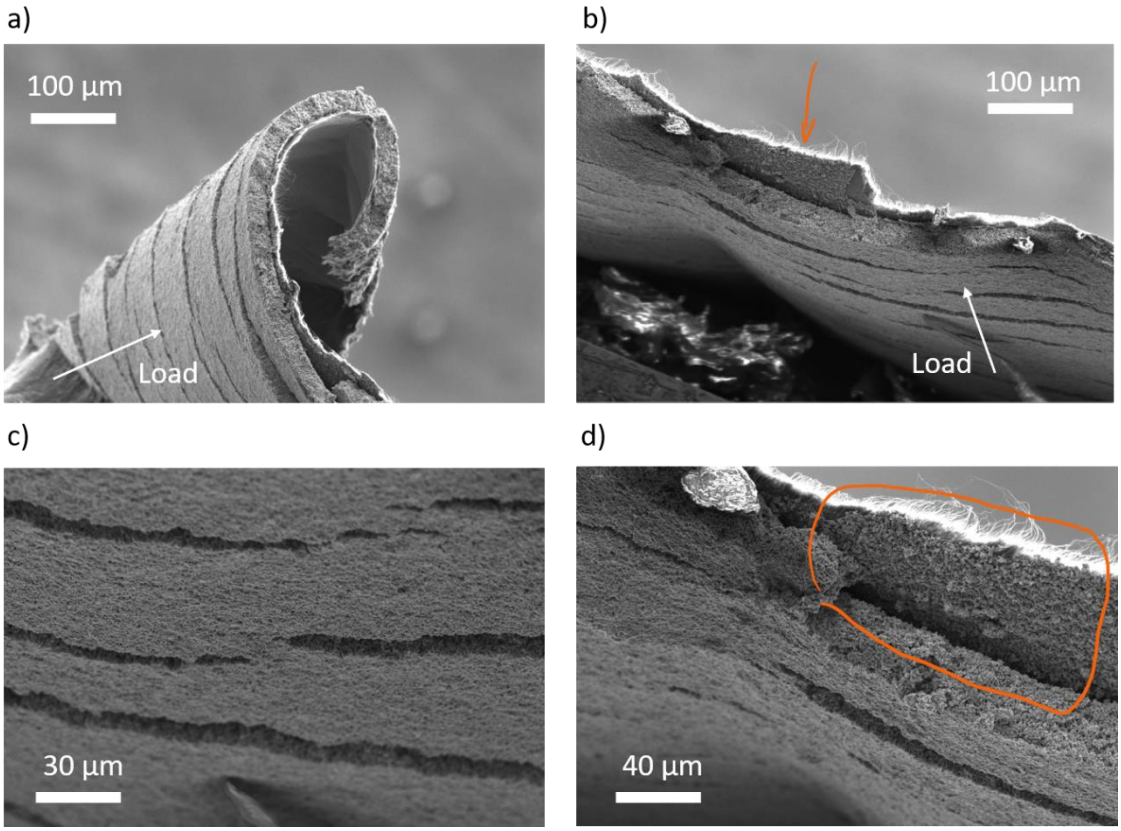

Figure 3.11: SEM micrographs of the fracture surface of CNT+LFP specimens. (a) Notice how the LFP coating remains attached to the structure even for tight radius of curvature. (b) Detail of delamination close to the fracture surface. Highlighted in orange: Delaminated CNT veil with LFP particles attached. (d) Same area, higher magnification. (c) Detail of fractures perpendicular to the load on LFP coating. Images courtesy of Anastasiia Mikhalchan.

In Figure 3.11-b the cross section of a fracture surface shows how delamination occurred between the LFP layer and the CNT substrate. However, it is possible to see in Figure 3.11-d depositions of LFP particles that remained attached to the CNT veil even after the rupture of the ceramic coating. This confirms the infiltration of the coating in the bundle network to some extent.

The fact is further confirmed by the SEM images of an analogous LTO-CNT electrode (prepared with the same slurry composition) taken from the CNT side (Figure 3.12). The regular low-energy image (a) shows the presence of some impurity clusters in the yarn network. The back-scattered mode (b) reveals fine particle-agglomerates (< 100 nm) at those clusters. A quick point-by-point energy dispersive X-ray spectrometry (EDS) exposes the presence of titanium and carbon in those bright particles. Them being

concentrated at the clusters seems to confirm that they are nothing but LTO and Super P dragged by infiltrated polymer binder.

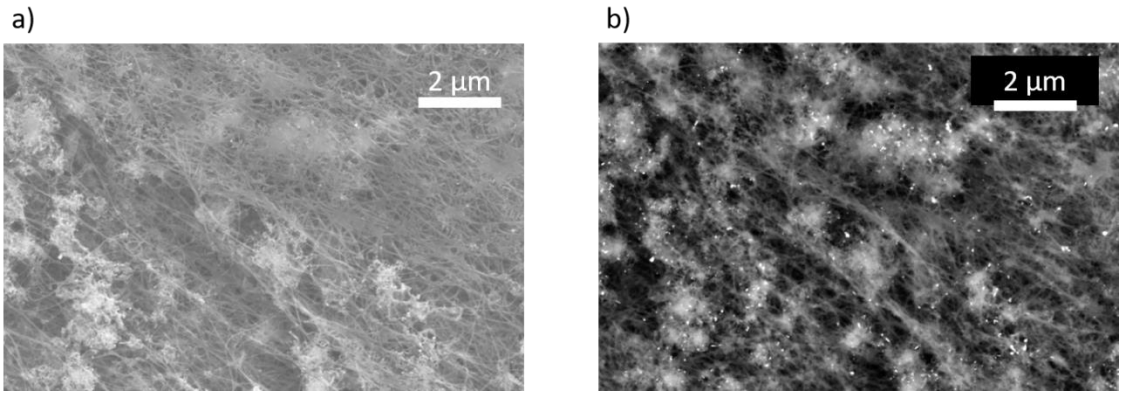

Figure 3.12: Regular (a) and back-scattered (b) SEM Micrograph of an analogous LTO-CNT electrode prepared with equal slurry composition. View from the CNT side. Images courtesy of Anastasiia Mikhalchan.

Having confirmed the efficient infiltration of the coating resulting in enhanced mechanical properties, the next step would be to quantify it precisely. The curve plotted in Figure 3.9-b was created under the assumption of a linear relationship with the added mass loading of coating. Nonetheless, that was an arbitrarily chosen exponent. A future study should be carried out to discern what mechanism prevails in the augmentation of the mechanical properties (friction or polymeric matrix), and what is the consequent fitting law. The components of the slurry and their proportions seem to have a crucial effect on the mechanical behavior of the electrode assembly. Factors such as active material and Super P particle size or the choice of a specific polymer binder look worth of studying

Regarding the stiffness, Figure 3.13 contains the values for the initial elastic slope and its specific variant. More conclusions can be obtained thereafter. The elastic slopes are enhanced, also in aluminum, and despite the uncertainty ranges. There is a 50% increase in the aluminum; and a much more dramatic 1160% for the CNT veil. These increases, unlike it happened with the strength, do compensate the added weight of the coating. As showed in Figure 3.8-d, the specific modulus of the coated strips are on the same range as their uncoated counterparts.

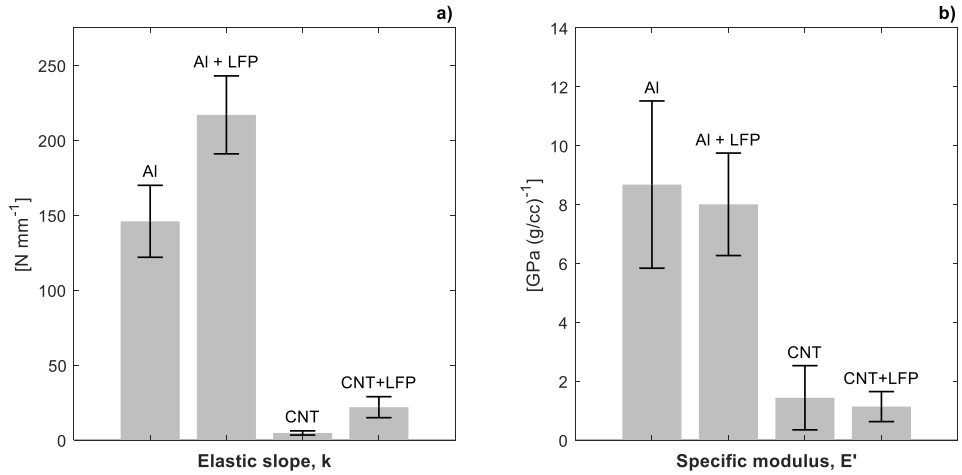

Figure 3.13:Comparison of elastic slope (a) and specific modulus (b) of coated and uncoated materials.

The proposed explanation to this phenomenon is the effective contribution to the load demand of all the thickness of LFP during the beginning of the test, at very low strains. During those initial instants, the coating layer still has not broken and contributes to the overall stiffness of the material. Soon, cracks begin to appear in the coating and it stops carrying load. In the case of the aluminum, as a very weak interface is developed with the coating, the breaking force remains unchanged with respect to the plain foil.

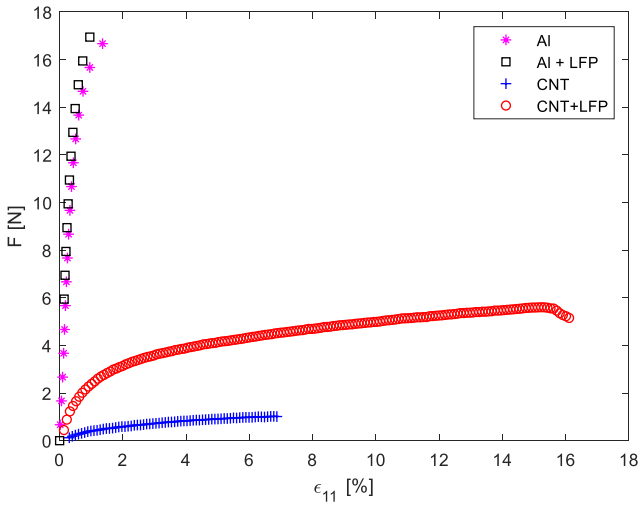

Figure 3.14: Force vs. strain curve of one representative specimen of each of the four kinds of material presented in section 3.1

In the case of the CNTs, the reinforcement effect continues during all the strain range as a result of the infiltration. Figure 3.14 shows a force-strain relationship of one representative specimen for each kind of material referred in this section. In that plot one can see that the strains levels at which the ceramic coating breaks, according to the given arguments, is around 1 %.

To continue this section, some words must be dedicated to the behavior of the elongation at break. A comparison for the percentage elongation is shown in Figure 3.15. In that plot we see that there seems to be a decrease in the strain at break for the aluminum when is coated (1.0% vs. 1.95%), even though the uncertainty increases. Both values are perhaps too low for a metallic material.

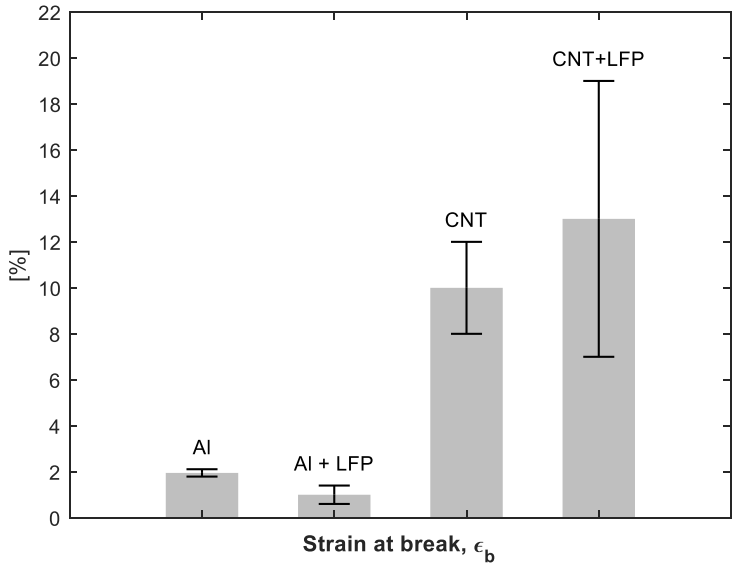

Figure 3.15: Comparison of values for elongation at break between coated and uncoated materials.

However, as it was explained in section 3.1.2, the measures of elongation at break in the DMA machine are not as reliable because, being a force-controlled machine, a sudden increase of the strain-rate occurs when the material enters the plastic zone. It is concluded that new measurements in a displacement-controlled machine should be performed. It is true that, defective or not, the same machine was used for the Al and Al+LFP samples, so a reduction in ductility due to the coating could be real. However, it is not clear the mechanism that would cause this to happen, because it seems to go against the poor adhesion hypothesis. Besides, during the manipulation of the samples it was possible to observe shiny edges around the coated aluminum specimens (see Figure 3.16). These were the result of the delamination and fall of coating *flakes* that left the aluminum uncovered. Obviously, this observation is hard to quantify, but it cannot be neglected that it reinforces the idea of the poor adhesion.

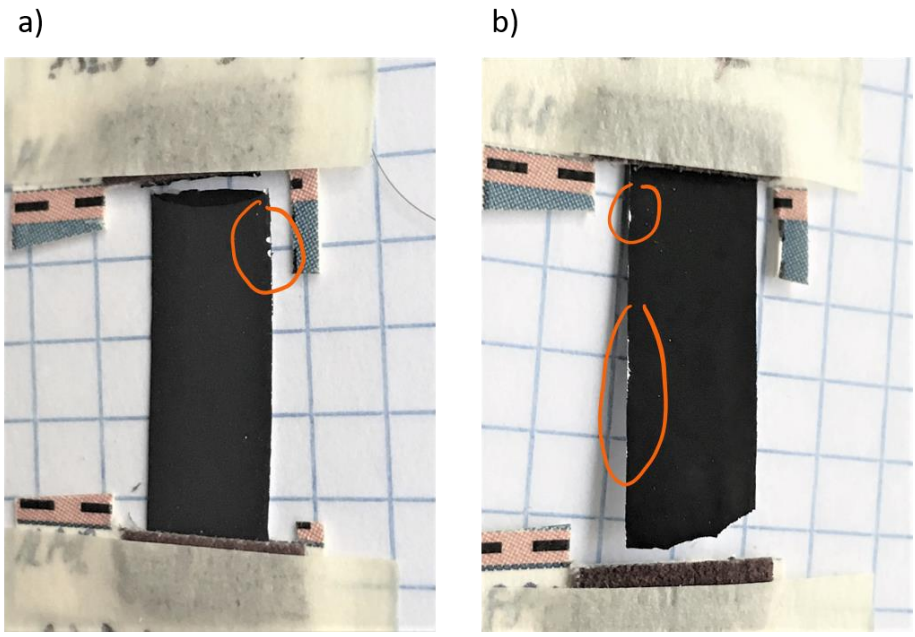

Figure 3.16: Close-up images of two different specimens of Al+LFP (a) Specimen 5; (b) Specimen 7. Highlighted in orange are the visible aluminum regions resulting from the falling of the easily delaminated flakes *of coating.*

The behavior of the coated nanotubes seems to be similar in terms of ductility that the sole CNT mat. The average value is a bit higher (12.6 vs. 9.5 %), but the dispersion of the results for the CNT+LFP sample is quite high, so it cannot be concluded confidently that an improvement of the ductility takes place. Nonetheless, the dispersed polymer matrix observed in the micrographs could have a positive effect on ductility by preventing the bulk failure of the mat, delaying the onset of fiber pull-outs, which seem to be one of the main phenomena along the fracture surface, according to Figure 3.11-b and -d.

The micrographs of Figure 3.11-c and -d also show the appearance of cracks perpendicular to the direction of the load on the LFP surface. Figure 3.11-c shows a closer detail of such fractures, which are likely to appear as a way to allow the longitudinal strain to take place across the whole thickness. This is another indication of the strong adhesion between the LFP layer and the CNT substrate because, despite of these cracks, the coating layer remains attached to the substrate They are not visible to the naked eye and their effect on the electrical properties will be a matter of discussion of the next chapter.

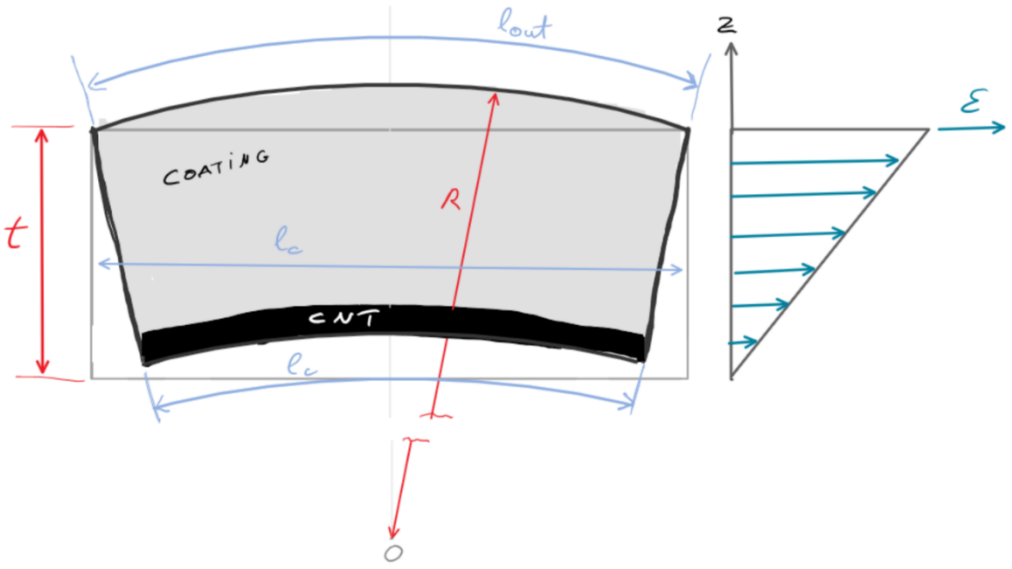

Figure 3.17: Schematics for the minimum radius estimation. Neutral axis (z=0) is assumed to be at the bottom of the CNT mat.

Finally, a short discussion on the behavior of the CNT electrode when bent and folded is introduced. From a macroscopic point of view, following the strength of materials equations, it is possible to make an estimate of the minimum radius of curvature that is attainable for a given thickness and strain limit. Hence, using the nomenclature of Figure 3.17, it can be written (eq. (3.4)) that the engineering strain at the outermost surface of the sheet (ε_{out}) is proportional to the distance to the neutral axis of the foil (z_{out}) divided by the radius of curvature to which it is subjected (R) [62]. This is valid for pure-bending conditions, with a linear and continuous tensile strain distribution along the thickness, a common assumption in laminated composites [43], to which this electrode resembles.

$$\varepsilon_{out} = \frac{l_{out} - l_c}{l_c} = \frac{z_{out}}{R} \tag{3.4}$$

The equation is not an estimate; it is derived from first principles. Nonetheless, the situation of the neutral axis is not trivial in a laminated structure such as this. Therefore, the worst-case-scenario for the coating is assumed, and the neutral axis is set at the bottom side of the CNT veil, what is impossible, but is not far from the actual situation that would take place, considering that the CNT mat carries most of the load and is much thinner than the coating.

With those conditions applied, the minimum radius of curvature (R_{min}) at which no breakage of the structure will appear is dictated by equation (3.5), where t is the thickness of the sheet and ε_b is the elongation at break of the material.

$$R_{min} > \frac{t}{\varepsilon_b} \tag{3.5}$$

Substituting in (3.5) for a thickness value of 40 μm and maximum strain of 9.5 %, we obtain a minimum radius of 0.42 mm, which would be translated, in practical terms, to a foldable structure. Nevertheless, this estimation was claimed to be macroscopic because the micrographs of Figure 3.11 show that, at strain levels of around 10 %, microscopic cracks have already appeared on the ceramic layer.

Yet to be confirmed is the fact that these cracks do not alter other properties such as the electrical ones or the subsequent mechanical behavior. Next chapter discusses on the electrochemical performance observed.

4. ELECTROCHEMICAL PERFORMANCE

4.1. Results

4.1.1. Initial test

Table 8: Discharge properties of deformed and undeformed electrodes during initial testing at C/10. Specific values normalized by mass of active material.

	Undeformed	**Deformed**
Nominal voltage (V Li^+/Li)	3.306 ± 0.005	3.46 ± 0.03
Nominal specific capacity (mAh/g)	162 ± 3	161 ± 9
Specific energy (Wh/g)	0.545 ± 0.009	0.54 ± 0.03
Coulombic efficiency, 1st cycle (%)	100.4 ± 0.2	94 ± 6
Coulombic efficiency, 5th cycle (%)	99.8 ± 0.3	99 ± 2

As explained in section 2.4.2, the coin cells were tested initially at C/10 for 5 cycles to determine a benchmark of their performance. Table 8 summarizes the average values obtained for a sample of 6 specimens of the undeformed and deformed electrodes. The specific values are normalized by mass of active material (see Table 9).

Table 9: Active material mass of each specimen tested. Notice the difference between the undeformed specimens of circular shape, and the deformed ones, cut from smaller specimens of mechanical testing.

	Specimen number	1	2	3	4	5	6
m_{active} $(mg \pm 0.1)$	Undeformed	5.8	5.7	5.8	9.3	9	10.2
	Deformed	1.2	1.3	2.2	1.4	2	1.5

The disparity in active material mass of the undeformed electrodes comes from the fact that specimens 4, 5 and 6 were not cut from the electrode LFP003.01 referred in

Table 4 (section 2.2.3), but from another one of the same batch (LFP003.02), which had a higher slurry content. In advance, it shall be distinguished between the *thin* (1, 2 and 3) and *thick* (4, 5 and 6) undeformed specimens.

4.1.2. Rate Capability test

To evaluate the charge-storing capability of the battery at different charging speeds, the rate capability test was performed, whose result is presented in Figure 4.1. This kind of plot is commonly used in battery performance reports [63]. Each point in the graph is computed as the average discharge capacity of each sample during the 5 cycles performed at every C-rate. Each pair of points belongs to a different C-rate: from left to right, C/10, C/5, C/2, 1C, 3C.

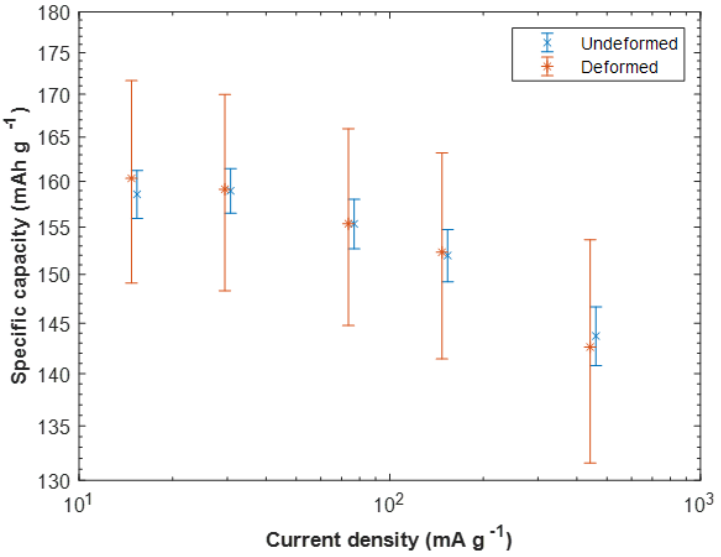

Figure 4.1: Rate capability test plot. (a) Undeformed. (b) Deformed. Values averaged among all specimens tested. From left to right, C/10, C/5, C/2, 1C, 3C.

Comparing the undeformed and the deformed samples it is noticeable the increase in uncertainty of the capacity that appears among the deformed specimens. The reason behind this is nothing but the smaller size of the deformed samples, and the lower active mass value associated (Table 9). As the same precision balance was used for all the electrodes, the relative uncertainty of the gravimetric capacity of the smaller electrodes must be bigger. Nevertheless, it is clear that not only the trend, but also the average values are very close in both samples. Although specimens of bigger size would be desirable in the case of the deformed electrodes to improve the precision, the fact that the mean values coincide as exactly as they do makes reasonable to guess that the measurements are accurate.

Table 10 shows the points used to build the previous graph and the relative discharge capacity compared to the C/10 cycle. The data show a loss of approximately 5% and 10% for the high-speed charge deployment at 1C and 3C respectively.

Table 10: Mean specific capacity values and relative value compared to cycle at C/10.

	Undeformed		**Deformed**	
	$\bar{C}_{spec}(mAh\ g^{-1})$	$\bar{C}_x/\bar{C}_{C/10}$ (%)	$\bar{C}_{spec}(mAh\ g^{-1})$	$\bar{C}_x/\bar{C}_{C/10}$ (%)
C/10	159 ± 3	100	160 ± 11	100
C/5	159 ± 2	100	159 ± 11	99
C/2	155 ± 3	98	155 ± 11	97
1C	152 ± 3	96	152 ± 11	95
3C	144 ± 3	91	143 ± 11	89

Regarding the coulombic efficiency, it should be pointed out that the values for each C-rate have been obtained excluding the efficiency of the first cycle. As it is possible to see in Figure 4.2-a and -b, there are some abrupt peaks in the coulombic efficiency versus cycle number. Those peaks belong to the cycles 1, 6, 11, 16 and 21; namely, the first cycle of each C-rate. They have been excluded from the calculation of the average since they are caused by a phenomenon which arises when switching the current density which will be commented in the discussion.

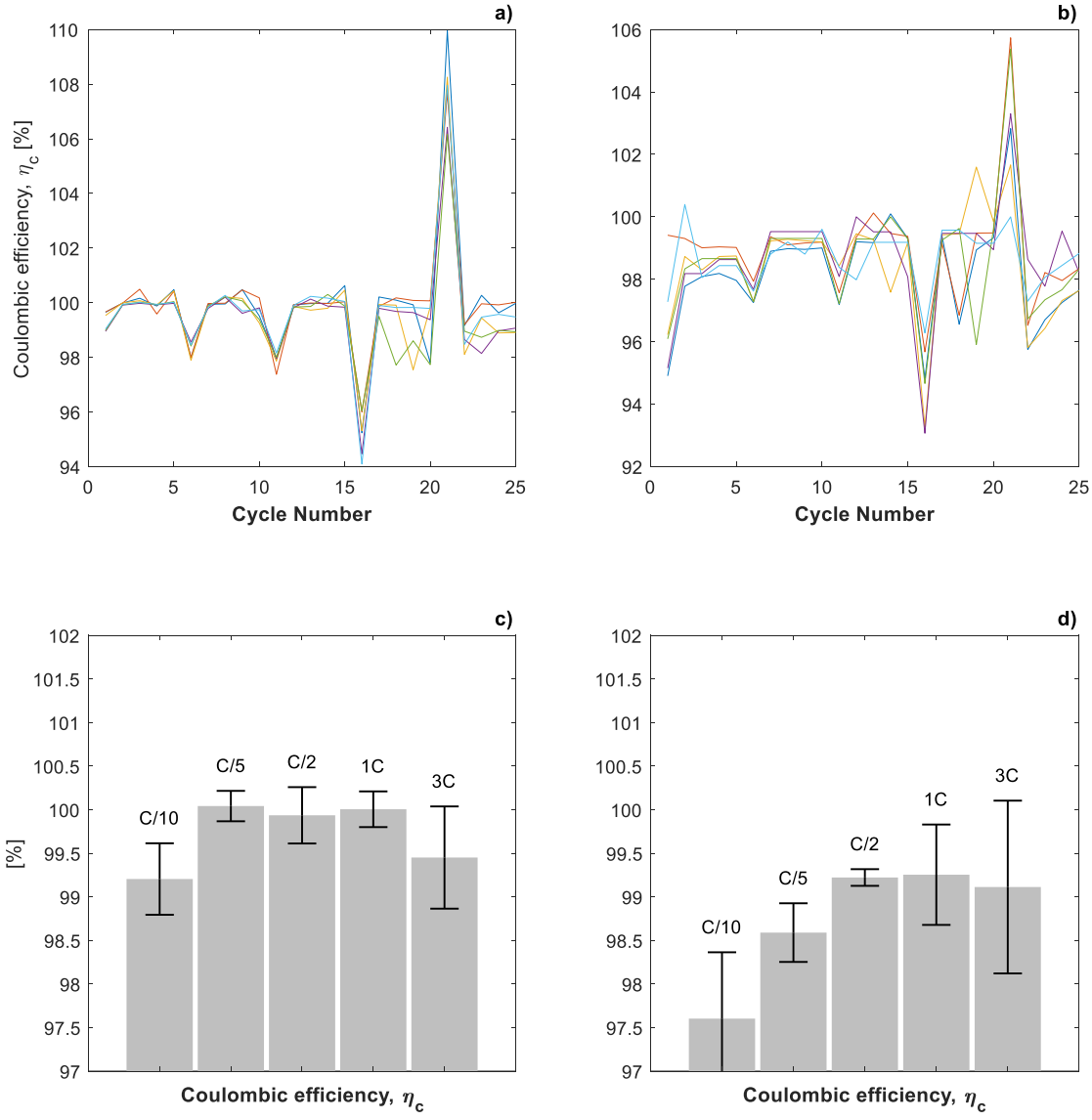

Figure 4.2: Coulombic efficiency as function of cycle number (a, Undeformed; b, Deformed) and C-Rate (c, Undeformed; d, Deformed).

To finish with the rate-capability data, Figure 4.3 presents the energy efficiency of the electrode in a manner analogous to that of the coulombic efficiency. The values of the first cycle of each C-Rate were, again, excluded, due to the same kind of peaks.

In the case of the energy efficiency, the plots show a different trend to the one observed with the coulombic, as the C/10 cycle has the highest (undeformed, Figure 4.3-a) and second-highest (deformed, Figure 4.3-b) efficiency. At higher C-rates the polarization and ohmic losses become both more relevant, as pictured in Figure 4.4. However, in the case of the coulombic efficiency, the ohmic or IR losses are not as relevant because, as long as the side-effects of higher currents (such as higher temperature) do not distort the capability of the material to store charge (like if, for instance, thermal expansion degrades

the assembly), the amount of electricity that is possible to be extracted during discharge will be very similar to that of the charge. Yet when talking about energy, those IR losses are increased irreversibly at higher C-rates, so the difference between charge and discharge becomes larger.

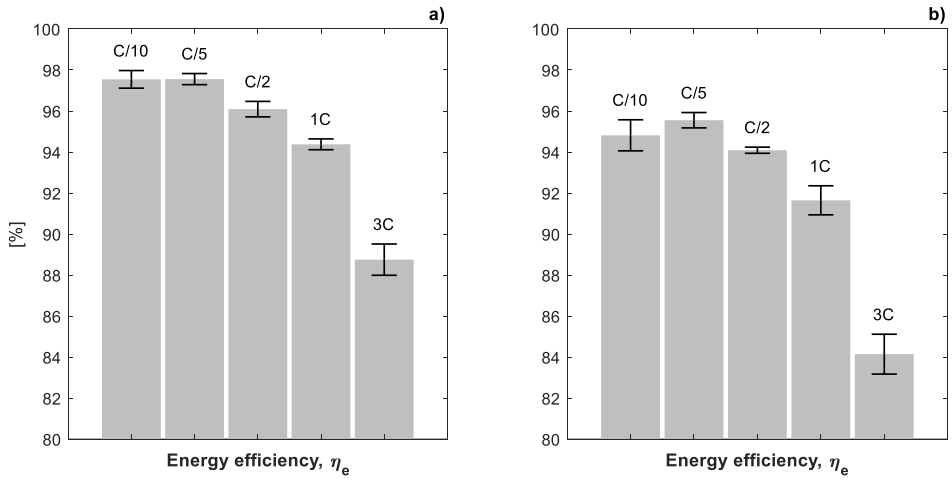

Figure 4.3: Energy efficiency as function of cycle number (a, Undeformed; b, Deformed) and C-Rate (c, Undeformed; d, Deformed).

From the comparison of Figure 4.3-a and -b it is also possible to notice a slight decrease of around 2% in the overall efficiency of the electrode at moderate C-rates (1/10 to 1) when it is deformed with respect to the original electrode. This reduction climbs to approximately 4% at 3C.

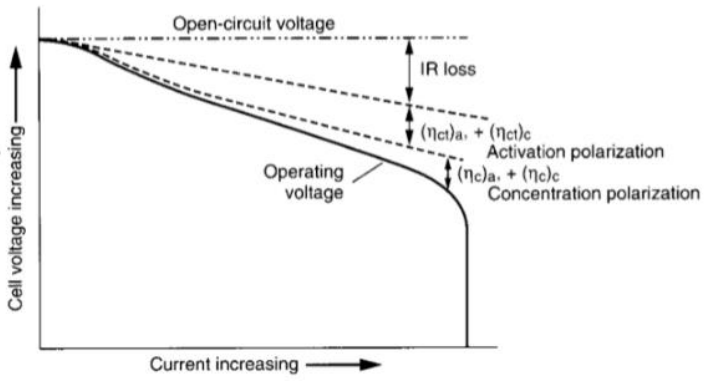

Figure 4.4: Cell polarization as a function of operating current. Reproduced from [6].

4.1.3. Cyclability test

To have a first intuition on what to expect from the deformable electrode in terms of long-term performance, a cyclability test was carried out, as detailed in section 2.4.2: one hundred charge-discharge cycles, at C/2. The results of the tested samples are presented

here. Figure 4.5 shows the outcome of the undeformed specimens, whereas Figure 4.6 does the same for the deformed sample. The legend presented in item (a) of the figures refers the specimen number and is valid for the other graphs.

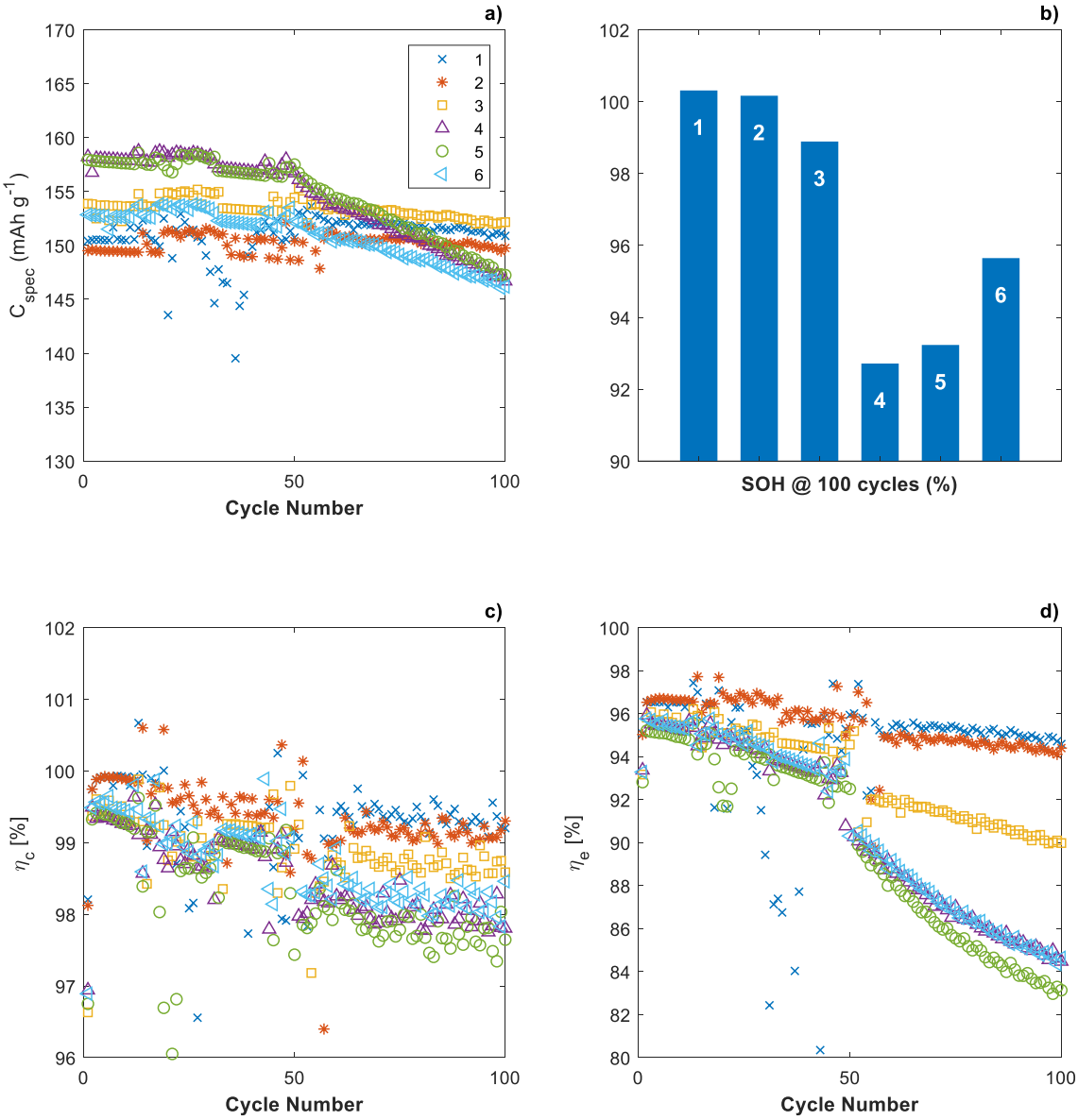

Figure 4.5: Cyclability test results for the undeformed samples. (a) Specific discharge capacity (b) State of Health (SOH) after 100 cycles. (c) Coulombic efficiency. (d) Energy efficiency. The legend in (a) denotes the specimen number, and it is valid for (c) and (d).

Both the undeformed and deformed samples present noticeable peaks on the graphs, caused by micro-short-circuits occurring due to the utilization of lithium metal. These are caused by the formation of dendrites by uneven metal deposition on the anode which pierce the separator. In the case of test cells, the separators do not have normally enough mechanical strength to resist that intrusion, and the lithium metal reaches the positive

electrode, short-circuiting the assembly [5]. Sometimes these dendrites self-melt instantaneously because of the heat increase and prevent the catastrophic failure. Also, they are partially dissolved during discharge. However, the irregularities created during deposition never fade completely and the dendrites "front" steadily advances with time during charging phases. Therefore, dendrites formation eventually results in short-circuiting, cell failure and possibly, in thermal-runaway.

The state of health (SOH) that appears on item (b) was introduced in section 1.2.1.3. In the figures, it is computed as the ratio of the discharge capacity after the hundredth cycle over that quantity after the first cycle of the cyclability test. Notice that the first cycle of this test is in fact the 31st one of the cells, considering the previous assessments. It was decided to use that capacity as reference, instead of the nominal value presented in 4.1.1, because it is different for each specimen and therefore gives a better understanding of the aging undergone by each electrode separately.

Regarding the non-deformed samples, it is noticeable that there is a slight difference in behavior between the specimens 1 to 3, and 4 to 6. The first ones have a slightly lower capacity at the beginning but retain a significantly higher SOH after 100 cycles (around 95%). It is worth recalling that, as Table 9 shows, specimens 4 to 6 have an active material mass 64% higher than 1 to 3, on average, as they were cut from different thicker electrodes. This is an interesting result because, from Figure 4.5-d it is possible to observe a simultaneous deterioration in the energetic efficiency of the thicker samples, which decays to the near of 85 %. At the same time, the thinner samples retain higher values: more than 90 % for number 3, and around 95 % for 1 and 2. The trend is interesting because it is not reflected on the coulombic efficiency, which is slightly lower, in general, for the thicker electrodes, but decreases progressively. On the other hand, the other two magnitudes (capacity and energy efficiency) see a significant increase in the negative slope after the 50th cycle. From the point of view of the ohmic and polarization losses described earlier in 4.1.2, it makes sense that the thicker electrodes have overall lower values of efficiency, since it is more difficult for the charges to move around. The sudden change in the "slope of aging", also known as non-linear aging, is related to the deposition of lithium at the anode (lithium plating). It is reasonable that thicker electrodes are more prone to it due to the higher polarization, which causes the potential at the anode to be lower, aggravating the effect.

To finish with the comments on the undeformed sample, it is remarkable the existence of a small increasing step in the specific capacity of all the specimens at around the 20th cycle (Figure 4.5-a). The fact that all of them show this somewhat strange behavior suggests that it could be a perturbation of the cycler, since they were all connected simultaneously to different channels (see Figure 2.8-a, in section 2.4.2), perhaps room-temperature changes, on the order of 5 ºC.

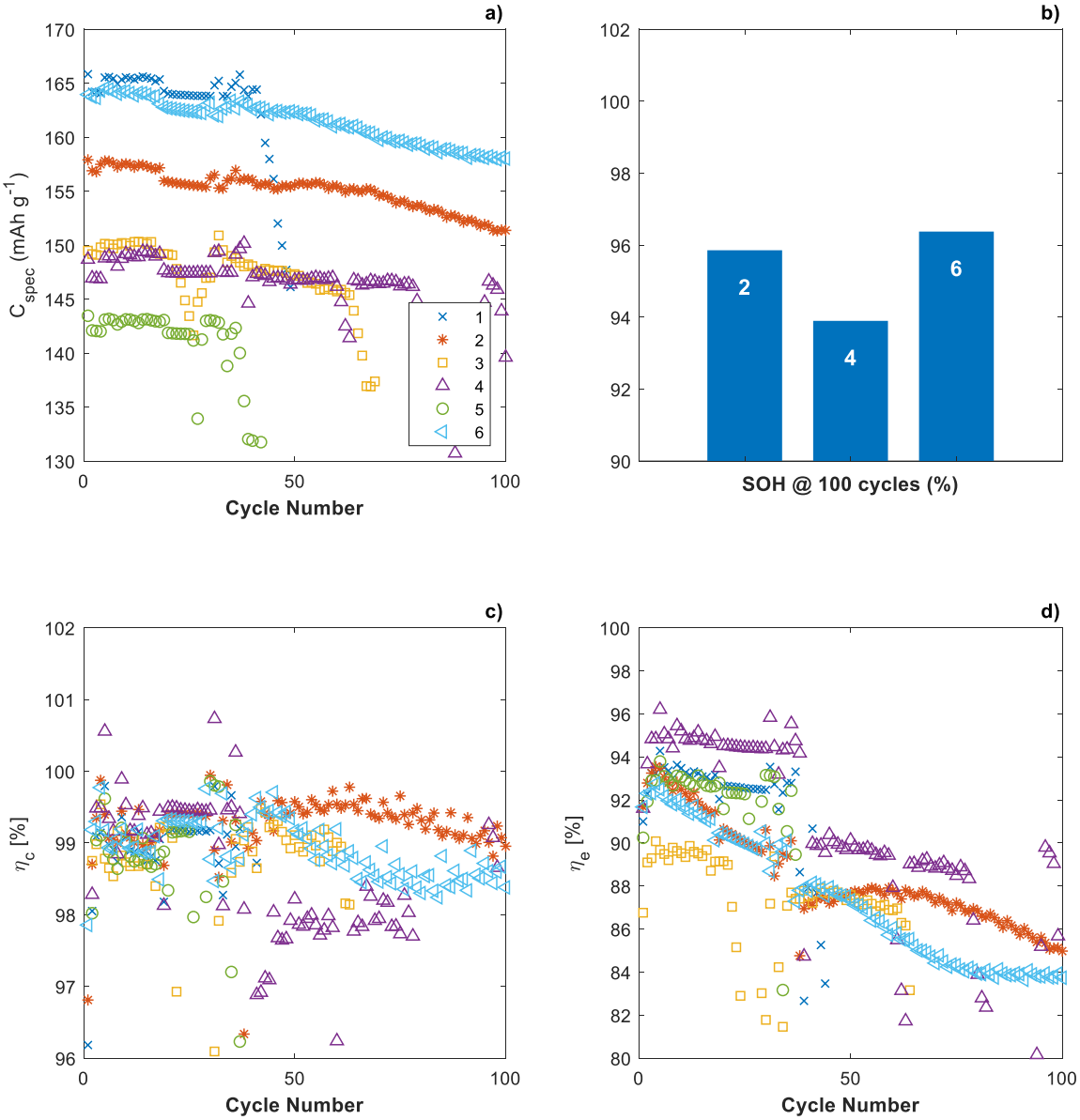

Figure 4.6: Cyclability test results for the deformed samples. Description of Figure 4.5 is analogously applied here. Specimens 1, 3 and 5 are not represented in (b) because they did not reach the 100th cycle.

The results of the deformed sample are presented in Figure 4.6. One of the things that will call the attention firstly will be the lack of three of the specimens at the SOH plot (Figure 4.6-b). Specimens 1, 3 and 5 could not reach the 100th cycle because they were

short-circuited earlier. The other three showed SOH in the near of 95 % at that point of aging.

The coulombic efficiency (Figure 4.6-c) behavior shows a similar behavior to that of the undeformed sample, with very little decrease in coulombic efficiency after 100 cycles (higher than 98 %). However, also similarly to the undeformed sample, the aging has a stronger effect on the energy efficiency (Figure 4.6-d), with the specimens being between 85 and 90 % at that point. Nonetheless, although the loss of efficiency after 100 cycles is like that of the thick undeformed specimens, the rate at which it is lost seems to be different, as the change in slope occurring around cycle 50 does not take place here. It is, instead, generally constant (obviating the aforementioned short-circuit peaks).

Other generalized steps in capacity appear around cycle 20 and 35, decreasing and increasing, respectively (Figure 4.6-a). Nonetheless, in those plots there seems to be a correlation between the appearance of those steps and the onset of short-circuit in one of the specimens. The step at cycle 20 coincides with the a negative peak of specimen 3, and the step at cycle 40 also happens together with the failure of specimens 1 and 5. Furthermore, a negative peak of specimen 4 at cycle 60 seems to trigger the short-circuit of specimen 3 and even a change in the slope of specimens 2 and 6. Lastly, the negative peak of undeformed specimen 1 (Figure 4.5-a) is also synced with the step in the rest of the sample.

Yet its effects have to be analyzed more in depth, it seems reasonable to consider that the onset of short-circuit in some specimens may cause alterations in the cycles of the other channels, perhaps by affecting the electronic control of the cycler.

Other possible explanations would be that certain aging levels trigger mechanisms in the electrodes that affect the electrochemical process; or the aforementioned temperature variations. Regarding the first one, the fact that the thick and thin specimens of the undeformed sample look equally affected, coming from different electrodes, makes the electrochemical hypothesis less appealing than the apparatus perturbations idea.

A reason for the early failure of half of the specimens of the deformed sample could be a higher propensity to the lithium dendrites formation as the result of a stronger polarization. In the following discussion, arguments on the higher polarization of deformed cells are given.

4.2. Discussion

The initial potential is a bit lower in the undeformed specimens than in the deformed ones (3.31 versus 3.46 V Li^+/Li). Nevertheless, it is close in both cases to approx. 3.5 V Li^+/Li, as referred in the literature [5]. The specific capacity normalized by mass of LFP is close to the theoretical value (170 mAh/g) in both and coincides almost exactly with the practical gravimetric capacity reported (160 mAh/g) [5]. It is even slightly higher than the rated capacity of the commercial LFP utilized, 153 mAh/g (see section 2.2.2). This indicates that the construction of the electrodes using the CNT mat as current collector has been successful, which is an accomplishment because the CNT collector is already lighter and thinner than the traditional aluminum foil.

The values of the nominal areal capacity in mAh/cm^2 for the undeformed electrodes were computed, using the diameter of the coin cell (15 mm). They can be consulted in Table 11 together with the derived gravimetric capacity of the complete electrode, and a hypothetical figure of an equivalent electrode built with aluminum foil, using areal densities from Table 4 and assuming equal surface capacity. For the deformed specimens it was impossible to obtain this data since the perpendicular section was unknown. However, the differences are negligible.

*Table 11:Surface and gravimetric capacity of the complete electrodes. *Aluminum electrode is a hypothetical result assuming that the capacity would be equal to the thin CNT specimens.*

	Thin CNT+LFP	**Thick CNT+LFP**	**Al + LFP***
Surface capacity (mAh/cm^2)	0.52 ± 0.08	0.88 ± 0.18	0.52 ± 0.08
Gravimetric capacity $\left(\frac{mAh}{g_{elect}}\right)$	113 ± 24	–	79 ± 15

Although the assumption of equal surface capacity made for the aluminum electrode is on the cautious side, given that the thickness of its coating was smaller than on the CNT one, there is an increase in the specific capacity (on an electrode assembly mass basis) of 43% just by using a lighter and thinner current collector such as the CNT mat. Independently of other potential advantages, this is already a positive finding which could increase the practical gravimetric capacity of real batteries.

No remarkable changes in specific capacity or voltage occur with CNT+LFP electrodes after they have been strained to mechanical failure. However, there is a difference in the evolution of the coulombic efficiency during the first five cycles of the battery, at the initial test. The deformed specimens show an average of 94 % at the first cycle which climbs to 99 % at the fifth. The undeformed ones, on the other hand, do not present that evolution and show a coulombic efficiency close to 100 % right from the first cycle.

The initial low coulombic efficiency showed by the deformed specimens can be a consequence of more sluggish electrode kinetics, affecting the charge distribution in the electrolyte and, in turn, the lithium deposition mechanism on the anode. A higher polarization promotes the formation of dendrites, and the larger surface area created by those dendrites results in the formation a larger solid electrolyte interphase (SEI) layer on the anode, which lowers the coulombic efficiency of the first cycle.

The SEI is a passivation layer formed by the deposition of some electrolyte products as the result of redox reactions occurring at the interfaces of the electrolyte and the electrodes. It has low electronic and high ionic conductivities, and, in the case of secondary lithium-ion batteries, it plays an important role because it helps improve the lithium-ions intercalation process on the active materials, reducing over-voltages and aging [4]. Nevertheless, it also causes some drawbacks in the battery operation, the most noticeable being the increase in ohmic resistance.

In the case of the experimental half-cells presented here, with an LFP positive electrode and metal lithium for the negative, two different SEI layers are formed, one at each interface. The SEI layer on the anodic electrolyte-lithium metal interface is reported to contain an unstable compound (lithium alkyl carbonate) when the electrolyte contains ethylcarbonate, as it is the case (electrolyte composition, section 2.4.1). That organic compound continuously reacts and transforms with long-term contact with lithium metal [4], producing what is known as calendar aging. On the cathodic LFP electrode interface, since the redox potential is higher than on the lithium metal, the reactions are different. Here, lithium iron oxide (LFO) appears on the surface of LFP when in contact with air.

Perhaps due to differences in the storing conditions, the formation of LFO could have been promoted on the deformed LFP electrodes, which were transported to IMDEA Materiales for tensile testing and then brought back for coin-cell fabrication. On the

contrary, the undeformed electrodes stayed at IMDEA Energía and were stored sooner and not exposed to the ambient during mechanical testing. A higher content of LFO on the surface could exacerbate polarization in the deformed sample and, in turn, faster growth of lithium dendrites, with the consequences in SEI formation earlier discussed.

A higher LFO content in the deformed samples could also be a consequence of an increased electrode-air surface area thanks to the microcracks observed on the coating surface perpendicular to the loading direction during tensile testing (Figure 3.11-c, section 3.2). These cracks could also favor a heterogeneous electric field distribution during the first charges, which would also promote the uneven lithium deposition at the anode.

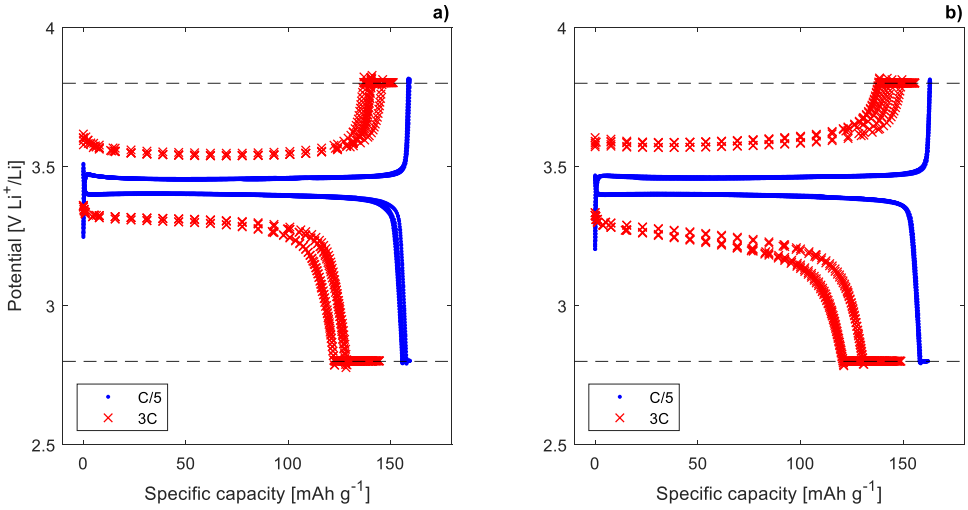

Figure 4.7: Potential-capacity plots of half-cells during 5 rate-capability cycles, each at certain low (C/5) and high (3C) current densities. (a) Undeformed specimen 3. (b) Deformed specimen 2.

Moving on to the rate-capability test, one of the parameters commonly utilized to characterize whether an electrode is power- or energy-oriented (section 1.2.1.3), is the surface capacity, mentioned earlier in this section and presented in Table 11 for the electrodes studied here. This is the case because electrodes (and full-batteries, by extension) with higher surface capacities are thicker, because of the higher contents of active coating, and this causes the ohmic losses to be more relevant. To put the manufactured electrodes in context, it should be mentioned that typical industrial Li-ion power-oriented electrodes are manufactured with surface capacities of 1.5 mAh/cm^2 or less, whereas energy-oriented typically range from 2.5 to 4.5 mAh/cm^2 [5]. This situates the CNT+LFP electrodes tested clearly on the power side (0.52 and 0.88 mAh/cm^2), what

would, in principle, enhance the behavior of the half-cells at high C-Rates, by reducing ohmic losses and over-voltages.

Figure 4.7 shows the voltage-capacity plots of representative undeformed and deformed specimens during 5 charge-discharge cycles. No significant difference is observed between the undeformed and the deformed electrode C/5 rate. However, a bigger hysteresis (difference in the potential plateau between charge and discharge) in the deformed specimen, as well as the steeper slope of the discharge curves, are indicators which confirm the higher polarization of the deformed specimens.

A common way to quantify the rate-capability of a battery is by using the Peukert's equation [64], which relates the capacity of the battery at different discharge rates by means of an exponent, k (eq. (4.1)). The closer this exponent is to 1, the less the capacity decreases with increasing discharge rate, and vice versa. A power-oriented device is designed to have a lower exponent than an energy-oriented battery.

$$C_{r1} = C_r \left(\frac{I_r}{I_{r1}} \right)^{k-1} \tag{4.1}$$

Where,

C_{r1} is the capacity at the desired rate, r1,

C_r is the known capacity, at rate r

$\frac{I_r}{I_{r1}}$ is the ratio of the currents,

k is the Peukert's exponent.

Using the data from Table 10, in section 4.1.2, and taking the nominal specific capacity obtained during the initial test at C/10 (Table 8) as reference, mean values for the Peukert's exponent were computed: 1.029 ± 0.003 and 1.025 ± 0.006 for the undeformed and deformed samples, respectively. Looking at values of the literature, these seem to be higher than expected given the power orientation of these electrodes. Graphite-LFP battery cells are reported to have exponents ranging from 1.000 to 1.015, and graphite-NCA a bit higher, 1.010 to 1.053 [5]. This means that the fast-charging capabilities of the manufactured half-cells are not especially good.

Nonetheless, in a work by Lim et al. data of LFP electrodes with worse rate-capability are reported [65], with a resulting Peukert's exponent higher than 1.20 for the increase

from 0.5C to 1 and 2C. That poor performance is associated with the low electrical conductivity and ionic diffusivity of the LFP, described in 2.2.2. It could be a consequence of the LFP particles being too big or not homogeneously dispersed in the electrode mixture.

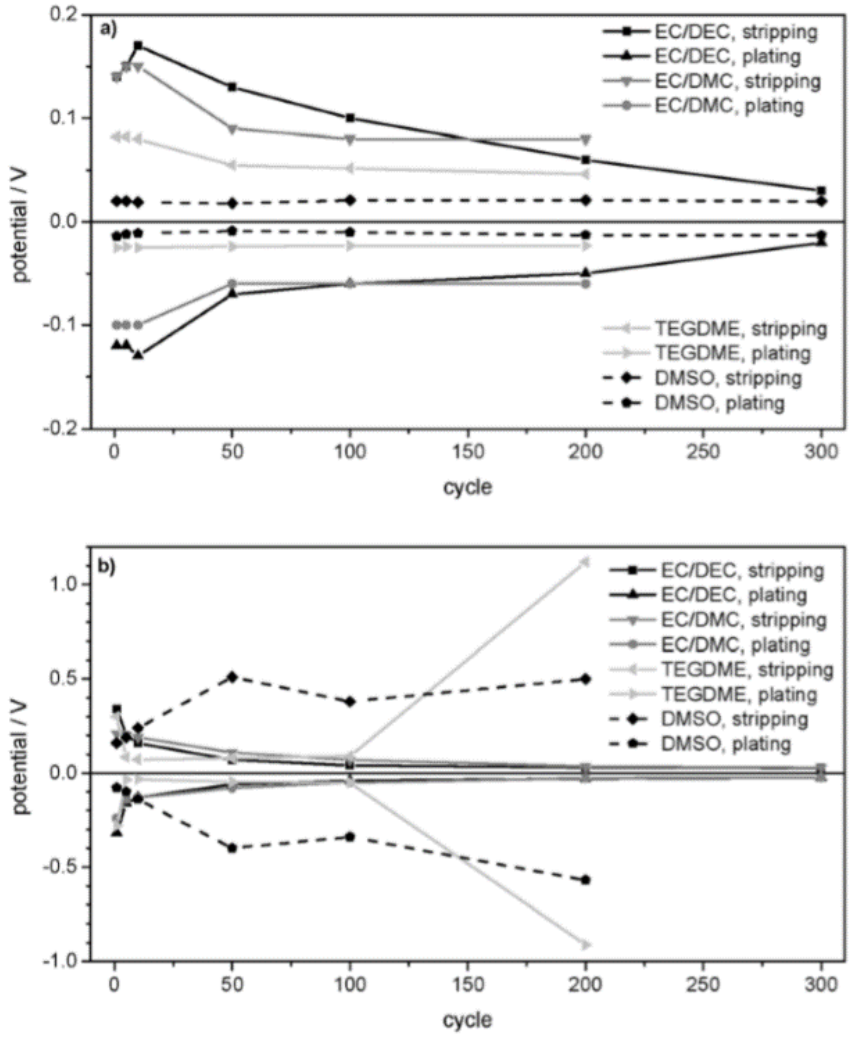

Figure 4.8: Maximum overpotentials of subsequent Li plating/stripping processes in Li/Li symmetrical cells. (a) j=0.01 mA/cm^2. (b) j=0.1 mA/cm^2. Reproduced from [66].

There exists an asymmetry between the charge and discharge potential-capacity profiles (Figure 4.7). Focusing on the 3C curves, it is noticeable that the constant voltage phases limited by the cut-off potentials are longer close to end of discharge than at the end of the charging phases due to the additional polarization. This is much likely a consequence of the asymmetry between the stripping (discharge, lithium dissolution) and plating (charge, lithium deposition) processes undergone by the lithium metal anode. Bieker et al. [66] reported larger over-polarization of lithium metal anodes during the

stripping phase, especially at the first cycles (before 50^{th} , see Figure 4.8), when the pristine lithium surface has not been roughened by continuous dissolution and deposition cycles. This is the phenomenon observed here. As the overpotential of the anode increases during discharge, the overall potential of the cell is decreased, and the cut-off voltage is reached earlier.

It is worth noting that the current density of the 3C cycles is almost 1.6 mA/cm^2, which is one order of magnitude higher than the values shown in Figure 4.8. This augments the differences in polarization.

The hypothesis of greater dendritic growth in the deformed specimens is reinforced by this idea, since the access to the pristine undissolved lithium would become more complicated in the presence of more prominent dendrites.

The asymmetry between charge and discharge is the reason behind the negative peaks in the coulombic efficiency which appear when switching to higher C-Rates (Figure 4.2 and Figure 4.3). During the first charge of the new higher-current cycle, the cell is more polarized, and less charge is stored. However, at the first discharge, the extra polarization of the higher current density aggravates the problems of over-polarization during lithium stripping, and even less charge is available. Therefore, the coulombic efficiency of the first cycle is reduced. On the second charging step, the maximum capacity which can be transferred back to the anode cannot be bigger than what was allocated at the cathode in that first over-polarized discharge, so the coulombic efficiency in the subsequent cycles is restored. Finally, when switching to a lower C-rate, (3C to C/10, cycle 26), the opposite behavior appears, and the blocked capacity becomes available again.

Thus, it is concluded that the heterogeneous lithium metal surface profile and the asymmetry between plating and stripping processes at lithium metal anode is limiting the cell rate-capability. This is supported by the slightly sloped potential-capacity profile of the deformed specimens at 3C (Figure 4.7-b), which is a hint of the lithium metal anode becoming the bottleneck of the charges' movement (it occurs at constant voltage in the LFP due to the two-phase intercalation described in 2.2.2).

Energy efficiency dependence on C-rate is acceptable, about 94 % for the undeformed and 92 % for the deformed, comparable to that of C-LFP and C-NCA technologies at low C-rates [5]. This is no surprise as the voltage profile is flat and the coulombic efficiency is very close to 100%. However, it decreases noticeably at 3C, especially for the deformed

specimens (from 94 to 89 % and 92 to 84 % in undeformed and deformed specimens, respectively). In Figure 4.7 one can see that hysteresis increases from around 100 mV at C/5 to around 300-400 mV at 3C. That fact, and the larger drop in energy efficiency of the deformed sample are in keeping with the polarization phenomena discussed.

No significant capacity loss in the C/10 cycles is observed after the rate capability test is completed. However, there is a slight decrease in the coulombic efficiency of the cycles at C/10 and 3C, especially in the case of the deformed specimens. It is believed that there are two competing phenomena. At C/10, the polarization is low, but the cell is stressed for longer, what leaves more time for slow irreversible reactions to take place, like the electrolyte's ethylcarbonate degradation. At 3C, however, there is not enough time for the slow reactions, but the extra polarization creates other degradation phenomena promoted at higher potentials. In the intermediate C-rates, a compromise between both mechanisms is reached and coulombic efficiencies are higher.

Regarding the cyclability test, the results are similar for both electrodes, ignoring the failed deformed specimens. The SOH is on the same range for the thick undeformed specimens and the deformed ones (94 %). Both present evidences of lithium plating: non-linear aging, in the case of the thick undeformed sample; and low initial coulombic efficiency for the deformed specimens. Nonetheless, the results are considered as satisfactory, especially for the undeformed thin electrodes, which show SOH higher than 98 % after 100 cycles. The most relevant issues encountered are related to the use of lithium metal as anode. Therefore, the outcome is promising. The electrode should eventually be evaluated in a full-cell against a more stable anode.

Lastly, an estimation of a hypothetical CNT-LFP/CNT-LTO cell is presented. The aim is to establish a comparison of the specific energy (per mass of electrode assemblies) of such a system with two different setups: another hypothetical LTO-LFP cell with traditional aluminum and copper current collectors; and one with a very common LIB couple: Al-LCO/Cu-graphite.

For the LTO-LFP, it is assumed a nominal voltage of 2 V [5], and that it is possible to manufacture an analogous electrode coated with an identical slurry containing LTO instead of LFP. Considering that the LTO theoretical capacity is very similar to the LFP (175 versus 170 mAh/g), and an approximate 10 % capacity excess on the anode for safety reasons, the hypothetical negative LTO electrode is assumed to have 102 mAh/g (90 %

of the value of the CNT-LFP, Table 11). Recovering formula (1.17) from the end of section 1.2.1.3, the LTO-LFP electrodes couple would have 53.6 mAh/g, translated to 107 Wh/kg at 2V working potential [1]. The electrolyte normally accounts for 20 % of the weight of the electrodes, so the cell would have 44.7 mAh/g and 89.17 Wh/kg, with only the casing left to be added.

Considering the gravimetric capacity of the hypothetical Al-LFP electrode (79 mAh/g, Table 11), which is a cautious assumption, as explained earlier, an estimation of a Cu-LTO is proposed. The capacity of the copper electrode is obtained by the addition of the mass loading of the CNT electrode, increased by 10 %, for the same reasons as earlier (4.73 mg/cm^2, Table 4) and the areal density of copper foil foil (8.8 mg/cm^2, Table 2). Finally, equal surface capacity is considered (0.52 mAh/cm^2, Table 11). This yields a negative electrode of 38.4 mAh/g. The resulting cell would have 25.8 mAh/g and 52 Wh/kg; that is, half of that of the battery made with CNTs.

In the case of the Cu-C/Al-LCO cell, their theoretical capacities are 372 mAh/g for graphite and 137 mAh/g for LCO [5]. For this hypothesis, a different approach is used, taking advantage of the inactive material mass term of equation (1.17) (which was not utilized before). Using the data of a state-of-the-art LIB, which is 6.20 g/Ah according to Placke et al. [1], the output of this cell would be 61.8 mAh/g and 235 Wh/kg.

The comparison lets extract some conclusions. The reduction in weight achieved by the CNT collectors of the LTO-LFP cell does not account entirely for the loss of specific capacity of the anode when using LTO instead of graphite. That problem is aggravated by the low working potential of the cell, what yields a specific energy almost 3 times lower than state-of-the-art C-LCO technology. Nonetheless, it must not be forgotten that the data assumptions come from preliminary experimental LFP electrodes in which the primary concern was the mechanical integrity upon tensile deformation, not the energy-storing capabilities. The calculations show that, under equal active materials, the switch to carbon nanotubes can double the specific capacity, while adding functionalities like deformability.

Despite the LTO-LFP couple being conservative in terms of specific energy, it is now possible to study other commercially available materials like LCO, LMO, NCA or NMC, for the cathode; and graphite, for the anode, which could be used with analogous manufacturing processes.

5. SOCIO-ECONOMIC AND ENVIRONMENTAL CONTEXT

5.1. Budget

The allocation of funds for the realization of this project is detailed in Table 12. Since the work was developed as an internship at the IMDEA Materiales and Energía institutions, the number of hours of the student researcher have been obtained by multiplying three months of 20 business days, with 7h shifts, plus 180h for the writing of the report.

Table 12: Detailed budget for the study.

		Unit price	Units	Total
Workforce (€/h)				
	Student researcher	15.00 €	600	9,000.00 €
	Main supervisor	40.00 €	20	800.00 €
	Auxiliary supervisor	30.00 €	20	600.00 €
	Assistant researcher	30.00 €	3	90.00 €
	Laboratory technicians	20.00 €	10	200.00 €
Software (€/yr.)				
	MS Office 365 license	69.00 €	0.5	34.50 €
	Matlab license	250.00 €	0.5	125.00 €
Hardware (€/yr.)				
	PC depreciation	250.00 €	0.5	125.00 €
	Peripherals	100.00 €	0.5	50.00 €
Raw materials				
	CNT commercial mat (€/kg)	50 €/kg	0.3	15.00 €
	Lab-produced CNT (€/kg)	75 €/kg	0.3	22.50 €
	Aluminum collector	2.5 €/m^2	0.06	0.15 €
	Copper collector	10.60 €/m^2	0.06	0.64 €
	Electrolyte	800 €/L	4.5	3.60 €
	Separator (Whatman GF/D)	0.5 €/u	12	6.00 €
	Coin-caps CR2032	1.66 €/u	12	19.80 €
	Wave spring/spacer	1 €/u	12	12.00 €
	LFP powder	1.1 €/g	10	11.00 €
	Super P powder	2 €/g	0.5	1.00 €
	Lithium metal	3 €/g	6	18.00 €
	PVDF binder	1 €/g	0.5	0.50 €
	NMP solvent	126 €/L	0.025	3.15 €
Others				
	SEM session (€/h)	30.00 €	3	90.00 €
	Office equipment			5.00 €
			TOTAL	11,232.84 €

The assistant researcher concept accounts for the SEM sessions carried out by Anastasiia Mikhalchan, another researcher of the Advanced Materiales For Multifunctional Applications group of IMDEA Materiales. The laboratory technicians were present during the tensile tests, helping set up the apparatus correctly.

The test machines (galvanostatic cycler, universal uniaxial tester, SEM, DMA) are assumed as depreciated since they would have been used for other purposes otherwise.

The prices for the CNT sheets were provided by the manufacturer (Tortech) and an estimation of IMDEA. For the test-cells consumables the data were taken from the suppliers, Solvionics, Sigma-Aldrich [67] and MTI Corporation [68]. For the software licenses, data from Mathworks [69] and Microsoft were utilized [70].

5.2. Socio-economic and environmental implications

Regarding the socio-economical side, it is worth considering the positive impact of research in the development of the country. The findings achieved by institutes like IMDEA provide with valuable intangible assets such as *know-how*, patents or talent preservation which help the productive network become more competitive, which ultimately results in and the improvement of the economic situation, with more job opportunities for the society.

Spain is one of the European leaders in the production of fiber reinforced composite materials, especially for the aerospace industry. as it is demonstrated by the great number of Spanish companies in the field, (Aerrnova, Aciturri, Alestis, M. Torres, Sener, etc.) [71], or the presence of centers of international companies such as carbon fiber producers (Hexcel [72] or Gurit [73]) and important consumers such as aircraft manufacturers, which have factories and R&D centers, like the multiple locations of Airbus [74] or the Boeing R&D center for Europe, located in Madrid [75].

Therefore, the developments in composite materials from academic efforts have great perspectives for their application to the real world through this strong industry. Hence, gaining knowledge on carbon nanotube fibers would help situate Spain at the cutting edge of a technology which looks suitable to, if not replace, at least complement carbon fibers in the long term. The obtained expertise could be combined with the existing *know-how* about composites, which this is a great opportunity to bring our country to the production

of reinforcement-fibers, which would be integrated into the prominent industry in the field.

Nonetheless, independently of their structural functionality, which is yet to be proven, the carbon-nanotubes worldwide market as a whole is expected to grow from $2,360 million in 2014 to more than $8,400 million by the end of 2022 [76], and $ 14,800 million by 2025 [77], so the importance of any competitive advantage which research can provide in this growing area of nanomaterials is unquestionable.

The socio-economic impact is not limited to carbon nanotubes. Lithium-ion batteries are another growing industry due to the electrification of transport and energy generation exposed in the introduction. Therefore, any steps forward in this area would also have a positive impact in the socio-economic situation of the country and the European Union. The lithium-ion battery market is expected to become a $46,000 million market by the end of 2022 [78].

One of the crucial questions which arises related to the expected growth of the LIBs market is the amount of lithium reserves available. According to reference [5], there are between 37.1 and 43.6 Mt of available lithium, enough for around 13,000 million of electric vehicles, which is ten times the current number of circulating cars. Therefore, the supply, at least for the EVs, is guaranteed.

Besides the socio-economic factors discussed, which would have more of a local impact in Spain and Europe, the competitive advantages gained through research would also have a global environmental positive outcome.

The most obvious improvements would be the reduction in energy consumption in the transportation sector and the increased presence of renewable energy sources. Nonetheless, it is worth considering too the benefits in sustainability coming from the use of new less harmful battery materials such as LFP with longer service-life, lower cost and less toxic composition.

Finally, the substitution of current carbon fibers by CNT fibers would also have a positive environmental impact. The production of carbon fibers relies on costly polymer precursors and, among other steps, requires high-temperature treatments (up to 3000 ºC) which are intensively energy and time consuming. Instead, production of direct-spun CNT fibers is comparatively cheaper and demand less energy (synthesis at 1300 ºC), as

reported by Mikhalchan et al. [79]. Besides, it could use potentially CO_2 or natural gas as carbon precursors, which would bring further improvements in sustainability [80].

6. CONCLUSIONS

Several conclusions can be extracted from this dissertation. A reproduction of the tensile testing of a commercial Tortech CNT direct-spun mat was successfully accomplished, with some minor discrepancies. The bulk tensile behavior dominated by the weak van-der-Waals interactions was observed.

The procedure for preparation of standalone CNT mat specimens was explored. It was concluded that, for an increase in accuracy, more refined methods should be carried out. These may include the utilization of dedicated tooling (such as tailored machined punch-die pairs), and the development of a different strategy to measure the thickness, given that a traditional micrometer was proven unsuitable. Nonetheless, despite the need of a more cautious procedure for the future, the method was sufficiently reliable to establish the comparison with the coated CNT mat, the main goal of this work.

Despite the low quality of the IMDEA CNT mat utilized, which was not specifically manufactured with great structural properties in mind, the specific strength values were already in the range of those of a thin aluminum foil. This result is encouraging, since by means of an increased winding-speed is possible to produce mats with higher degrees of longitudinal bundle-alignment, which should result in superior mechanical properties. The link between direct-spinning parameters, degree of anisotropy and mechanical performance could be the subject of future studies.

It is concluded that the electrochemical coating has a net absolute contribution to the load bearing capabilities of the CNT mat; and that the same phenomenon does not take place at the traditional aluminum collector. The differences arise at the interface between the coating and the substrate, because the porosity of the CNT material allows for more available surface and a more intimate connection.

The two mechanisms which contribute to the reinforcement of the nanotube network are, presumably, an enhancement of inter-bundle friction, produced by the LFP and SuperP particles of the coating; and the creation of an effective polymer matrix by the flow of the polymer binder during the coating process. Both help homogenize the stress distribution and thus, the bulk properties are enhanced.

A quantitative study relating the morphology of the coating and the mechanical behavior seems inescapable. Proportions of the constituents, particle sizes, the choice of

a polymer binder (or even its removal, as reported in other literature works [42]), and factors affecting the coating process itself, like the viscosity of the slurry, look crucial in the mechanical outcome of the electrode, much like the matrix of traditional fiber-reinforced composites.

That quantitative study of the coating morphology could also help discern the possibility of getting not only an increase in absolute load-bearing ability, but also an enhancement of the specific figures of strength and modulus, which should not be discarded provided the especial matrix-fiber interfaces which appear in CNT networks due to their nanoscale nature.

In terms of electrochemical performance, the results obtained are considered as quite successful. It has been proven that a robust reversible capacity for the LFP-CNT electrode is obtained, even slightly higher than the rated capacity from the technical sheet of the material. This is an indicator of the suitability of current semi-industrial CNT mats to the use as current collectors of LIBs, which would readily bring cells with better specific energies. The horizon for their widely application looks close in time, according to the results obtained here.

Nonetheless, the utilization of CNTs carries with it augmented mechanical properties, as exposed in the introduction. The viability of the ductile electrode was successfully demonstrated by means of previously deformed working electrodes, with strains at break in the range of 7-18 %. This opens the possibility of deformable batteries integrable in non-standard geometries, although the ductility is still quite limited, so the potential cavities could not have intricate shapes.

The electrochemical performance was only slightly degraded by the deformation. Nominal capacity, rate-capability and capacity retention upon aging were affected mildly. The differences may come from a larger exposed surface in the deformed electrodes, as a result of the microcracks perpendicular to the loading direction. Those additional sites could have reacted with air and formed larger quantities of LFO, increasing polarization in the deformed sample. The cracks could have also promoted the uneven distribution of the electric field upon charging, thus promoting the dendritic lithium deposition on the anode surface.

Altogether, the mutually-related over-polarization and dendritic formation work to explain the problems observed at the deformed and thick undeformed specimens, which also have poorer capacity retention after 100 cycles.

Nonetheless, the differences should not hinder the overall positive outcome of the tests, especially considering that the problems seem to be related closely to the utilization of lithium metal. The construction of a full cell with CNT current collectors, and conventional lithium intercalation materials seems like an obvious extension of this work and it would clarify the origin of the inconveniences found.

The somewhat poor rate-capability of the electrode could be also related to the electrode morphology. Maybe, too large LFP particles or an uneven distribution of super P around them. The quantitative study of the electrode morphology, suggested for the mechanical properties, could also help extract conclusions on this area. However, there are symptoms which suggest that lithium metal is the bottleneck in charges movement along the test-cell. This will also be clarified when a full-cell is constructed. The utilization of a solid polymer electrolyte (SPE) could also help improve the capacity retention at higher C-rates due to the elimination of the separator.

The specific energy of a hypothetical low-voltage LTO-LFP full cell was estimated, with not especially remarkable results. However, it was not the main goal of this study to achieve an efficient LIB, but to construct a proof-of-concept of the deformable electrode. Now that it has been accomplished, the optimization of the energy storage capabilities shall begin. The application of CNT collectors to other commercial active materials (LCO, NMC, graphite, etc.) opens the door for new lighter and flexible batteries in the short term.

Finally, looking towards longer term goals, framed within the multifunctional composites field, the reinforcement effect of active coating on the CNT-mat is considered as promising, despite the humble figures: 12 MPa/(g/cm^3) for strength; and 1.1 GPa/(g/cm^3) for modulus. Regarding this, important factors should be considered: the utilization of a “poor” CNT-mat, from the structural point of view, non-oriented to load bearing; and the use of a “traditional” LIB slurry, whose composition was not specifically tailored to a CNT collector.

Ideally, by means of a right combination of constituents, the active coating could become a multifunctional resin, reinforcing the CNT network and allocating the active

material. This issue is one of the most prominent ones in the literature of energy-storing multifunctional composites, although it has been historically more related with the creation of structural SPEs [3].

The multifunctional resin would be nothing but the result of the quantitative analysis of the morphology proposed earlier, although the dimension of this analysis should not be underestimated; quite the opposite. Nonetheless, without being able to specify more objective findings than the ones presented along this dissertation, it seems reasonable to point out the conceptual architecture of how a structural CNT battery may look in the future: a hierarchical composite, perhaps with a higher mass-fraction of CNTs than that of the presented CNT electrodes, where an ideal multifunctional resin formed a matrix providing simultaneously with stress distribution, ion conductivity and active material allocation.

This kind of construction, combined with an expected enhancement of mechanical properties of bulk CNT formats, and the advances in SPE electrolytes, both things coming from the research community, seem likes the sketch of how solid-state structural batteries might look in the future.

REFERENCES

[1] T. Placke, R. Kloepsch, S. Dühnen y M. Winter, «Lithium ion, lithium metal and alternative rechargeable battery technologies: the odyssey for high energy density,» *Journal of Solid State Electrochemistry,* vol. 21, nº 7, pp. 1939-1964, 2017.

[2] C. Menictas, M. Skyllas-Kazacos y T. Lim, «Chapter 6: Lithium-ion batteries (LIBs) for medium and large-scale energy storage: current cell materials and components,» de *Advances in Batteries for Medium and Large-Scale Energy Storage*, Woodhead Publishing, 2014.

[3] C. González, J. J. Vilatela, J. Molina-Aldareguía, C. .. Lopes y J. Llorca, «Structural composites for multifunctional applications: Current challenges and future trends,» *Progress in Materials Science,* vol. 89, pp. 194-251, 2017.

[4] J.-k. Park, Principles and Applications of Lithium Secondary Batteries, Singapore: Wiley-VCH, 2012.

[5] C. Glaize y S. Geniès, Lithium Batteries and Other Electrochemical Storage Systems, Croydon: ISTE Ltd. and John WIley & Sons, Inc., 2013.

[6] D. Linden y T. B. Reddy, Handbook of Batteries, 3rd Ed., McGraw-Hill, 2002.

[7] International Electrotechnical Commission, Secondary Cells And Batteries Containing Alkaline or Other Non-acid Electrolytes - Secondary Lithium Cells And Batteries For Portable Applications (IEC 61960-3:2017), 2017.

[8] European Standard, Aircraft batteries - Part 1: General test requirements and performance levels (IEC 60952-1:2013), 2013.

[9] U. Kasavajjula, C. Wang y A. J. Appleby, «Nano- and bulk-silicon-based insertion anodes for lithium-ion secondary cells,» *Journal of Power Sources,* vol. 163, nº 2, pp. 1003-1039, 2007.

[10] M. Yoshio, R. J. Brodd y A. Kozawa, Lithium-Ion Batteries: Science and Technologies, 2009: Springer.

[11] G. Derrien, J. Hassoun, S. Panero y B. Scrosati, «Nanostructured Sn-C Composite as an Advanced Anode Material in High-Performance Lithium-Ion Batteries,» *Advanced Materials,* vol. 19, nº 17, pp. 2336-2340, 2007.

[12] C. Menictas, M. Skyllas-Kazacos y T. Lim, «Chapter 7: Lithium-ion batteries (LIBs) for medium- and large-scale energy storage: emerginc cell materials and components.,» de *Advances in Batteries for Medium and Large-Scale Energy*, Woodhead Publishing, 2014.

[13] K. Wang, S. Luo, Y. Wu, X. He, F. Zhao, J. Wang, K. Jiang y S. Fan, «Super-Aligned Carbon Nanotube Films as Current Collectors for Lightweight and Flexible Lithium Ion Batteries,» *Advanced Functional Materials,* vol. 23, pp. 846-853, 2013.

[14] J. Stallard, W. Tan, F. Smail, T. Gspann, A. Boies y N. Fleck, «The mechanical and electrical properties of direct-spun carbon nanotube mats,» *Extreme Mechanics Letters,* vol. 21, pp. 65-75, 2018.

[15] C. J. Smithells, «19: Electrical properties,» de *Smithells Metals Reference Book*, 2004.

[16] AENOR, Cobre y aleaciones de cobre. Cátodos de cobre. (UNE-EN 1978:1998), 1999.

[17] A. Hirsch, «The era of carbon allotropes,» *Nature Materials,* vol. 9, nº 11, pp. 868-871, 2010.

[18] S. Iijima, «Helical Microtubules of Graphitic Carbon,» *Nature,* vol. 354, nº 6348, p. 56, 1991.

[19] T. D. Burchell, Carbon Materials for Advanced Technologies, Oak Ridge: Elsevier Science, 1999.

[20] V. J. González Velázquez, *Nanomateriales de carbono, síntesis, funcionalización y aplicaciones.*, Ph.D. Thesis, Dpto. Ciencia e Ingeniería de los Materiales e Ing. Química, UC3M, Leganés, Spain, 2015.

[21] E. Pop, D. Mann, Q. G. K. Wang y H. Dai, «Thermal conductance of an individual single-wall carbon nanotuve above room temperature,» *Nano Letters*, vol. 6, nº 1, pp. 96-100, 2006.

[22] B. Peng, M. Locascio, P. Zapol, S. Li, S. L. Mielke, G. C. Schatz y H. D. Espinosa, «Measurements of near-ultimate strength for multiwalled carbon nanotubes and irradiation-induced crosslinking improvements,» *Nature Nanotechnology*, vol. 3, pp. 626-631, 2008.

[23] J. Planeix, N. Coustel, B. Coq, V. Brotons, P. Kumbhar y R. Dutartre, «Application of carbon nanotubes as supports in heterogeneous catalysis,» *Journal of American Chemistry Society*, vol. 116, nº 117, p. 7935, 1994.

[24] O. Paris, «Carbon Nanotubes and Nanotube-Based Composites: Deformation Micromechanics,» de *Structure and Multiscale Mechanics of Carbon Nanomaterials*, Vienna, Springer, 2016, pp. 51-74.

[25] C. Journet, W. Maser, P. Bernier y A. Louiseau, «Large-scale production of single-walled carbon nanotubes by the electric-arc technique,» *Nature*, vol. 388, nº 6644, pp. 756-758, 1997.

[26] A. Rinzler, J. Liu, H. Dai, P. Nikolaev, C. Huffman y F. Rodríguez Macias, «Large-scale purification of single-wall carbon nanotubes: process, product and characterization,» *Applied Physics A: Materials Science and Processing*, vol. 67, nº 1, pp. 29-37, 1998.

[27] M. Endo, K. Takeuchi, K. Kobori, K. Takahashi, H. Kroto y A. Sarkar, «Pyrolitic carbon nanotubes from vapor-grown carbon fibers,» *Carbon*, vol. 33, nº 7, pp. 873-881, 1995.

[28] Y. Dahman, «7.3 Production Methods of NTs,» de *Nanotechnology and Fuctional Materials for Engineers*, Philadelphia, Elsevier, 2017.

[29] M. Mann, B. Milne y K. Teo, «Chapter 5: Engineering the Synthesis of Carbon Nanotubes to Fabricate Novel Nanostructures,» de *Emerging Nanotechnologies for Manufacturing: A volume in Micro and Nano Technologies*, Burlington, Elsevier Science & Technology, 2009, pp. 131-158.

[30] D. Eder, «Carbon Nanotube - Inorganic Hybrids,» *Chemical Reviews*, vol. 110, pp. 1348-1385, 2010.

[31] Y.-L. Li, I. A. Kinloch y A. H. Windle, «Direct spinning of carbon nanotube fibers from chemical vapor deposition synthesis.,» *Science,* vol. 304, pp. 276-278, 2004.

[32] H. D. Espinosa, T. Filleter y M. Naraghi, «Multiscale experimental mechanics of hierarchical carbon-based materials,» *Advanced Materials,* vol. 24, pp. 2805-2823, 2012.

[33] M.-F. Yu, B. S. Files, S. Arepally y R. S. Ruoff, «Tensile loading of single wall carbon nanotubes and their mechanical properties,» *Physical Review Letters,* vol. 84, pp. 5552-5555, 2000.

[34] A. Kis, G. Csányi, J. Salvetat, T.-N. Lee, E. Couteau, A. Kulik, W. Benoit, J. Brugger y L. Forró, «Reinforcement of single-walled carbon nanotube bundles by intertube bridging,» *Nature Materials,* vol. 3, pp. 153-157, 2004.

[35] S. Yoon, S. Lee, S. Kim, K.-W. Park, D. Cho y Y. Jeong, «Carbon nanotube film anodes for flexible lithium ion batteries,» *Journal of Power Sources,* vol. 279, pp. 495-501, 2015.

[36] D. T. Welna, L. Qu, B. E. Taylor, L. Dai y M. F. Durstock, «Vertically aligned carbon nanotube electrodes for lithium-ion batteries,» *Journal of Power sources,* vol. 196, nº 3, pp. 1455-1460, 2011.

[37] Z. Sun, J. S., h. Jin, Z. Du, Y. Zhu, A. Cao, H. Ji y L. Wan, «Robust Expandable Carbon Nanotube Scaffold for Ultrahigh-Capacity Lithium-Metal Anodes,» *Advanced Materials,* vol. 30, nº 32, 2018.

[38] H. Kim, J. T. Lee y G. Yushin, «High-temperature stabilization of lithium-sulfur cells with carbon nanotube current collector,» *Journal of Power Sources,* vol. 226, pp. 256-265, 2013.

[39] S. Choi, J. Kim, M. Eom, X. Meng y D. Shin, «Application of a carbon nanotube (CNT) sheet as a current collector for all-solid-state lithium batteries,» *Journal of Power Sources,* vol. 299, pp. 70-75, 2015.

[40] J. Ren, Y. Zhang, W. Bai, C. X., Z. Zhang, X. Fang, W. Weng, Y. Wang y H. Peng, «Elastic and Wearable Wire-Shaped Lithium-Ion Battery with High Electrochemical Performance,» *Angewandte Chemie,* vol. 53, pp. 7864-7869, 2014.

[41] J. W. Hu, Z. P. Wu, S. W. Zhong, W. B. Zhang, S. Suresh, A. Mehta y N. Koratkar, «Folding insensitive, high energy density lithium-ion battery featuring carbon nanotube current collectors,» *Carbon,* vol. 87, pp. 292-298, 2015.

[42] S. Luo, K. Wang, J. Wang, K. Jiang, Q. Li y S. Fan, «Binder-Free LiCoO2/Carbon Nanotube Cathodes for High-Performance Lithium Ion Batteries,» *Advanced Materials,* vol. 24, pp. 2294-2298, 2012.

[43] P. K. Mallick, Fiber-Reinforced Composites: Materials, Manufacturing and Design. 3rd Ed., Dearborn: Taylor & Francis, 2007.

[44] AENOR, Alambres de aluminio indutrial recocido, para conductores eléctricos (UNE 21096:1969), 1969.

[45] AENOR, Cobre-tipo recocido e industrial, para aplicaciones eléctricas (UNE 20003:1954), 1954.

[46] Y. Guo, Y. Huang, D. Jia, X. Wang, N. Sharma, Z. Guo y X. Tang, «Preparation and electrochemical properties of high-capacity LiFePO4-Li3V2(PO4)3/C composite for lithium-ion batteries,» *Journal of Power Sources,* vol. 246, pp. 912-917, 2014.

[47] Y. Zhao, L. Peng, B. Liu y G. Yu, «Single-Crystalline LiFePO4 Nanosheets for High-Rate Li-Ion Batteries,» *Nano Letters,* vol. 14, pp. 2849-2853, 2014.

[48] Y. Xia, W. Zhang, H. Huang, Y. Gan, J. Tian y X. Tao, «Self-assembled mesoporous LiFePO4 with hierarchical spindle-like architectures for high-performance lithium-ion batteries,» *Journal of Power Sources*, vol. 196, pp. 5651-5658, 2011.

[49] Alees Co., «LFP-NCO Cathode Material M121,» [En línea]. Available: http://www.aleees.com/en/product/lfp-nco/m121.html. [Último acceso: 20 September 2018].

[50] A. M. Gaikwad, A. C. Arias y D. A. Steingart, «Recent Progress onf Printed Flexible Batteries: Mechanical Challenges, Printing Technologies and Future Prospects,» *Energy Technology*, vol. 3, pp. 305-328, 2015.

[51] ISO, Plastics. Determination of tensile properties. Part 1: General principles (ISO 527-1:2012), 2012.

[52] ISO, Metallic materials. Tensile testing. Part 1: Method of test at room temperature (ISO 6892-1:2016), 2016.

[53] ISO, Plastics. Determination of tensile properties. Part 3: Test conditions for films and sheets. (ISO 527-3:1995), 1995.

[54] M. Roudau, Proability, Statistics and Estimation, 2013.

[55] J. Elliot, T. Gspann, J. Terrones y A. Windle, «The measurement of properties in carbon nanotube yarns,» *WSEAS TRANSACTIONS on APPLIED and THEORETICAL MECHANIC*, vol. 12, pp. 33-40, 2007.

[56] T. S. Gspann, N. Montinaro, A. Pantano, J. A. Elliot y A. H. Windle, «Mechanical properties of carbon nanotube fibers: St. Venant's principle at the limit and the role of imperfections,» *Carbon*, nº 93, pp. 1021-1033, 2015.

[57] M. Wachtler, «Li-Ion Batteries. Lecture: electrolytes.,» Zentrum für Sonnenenergie-und Wasserstoff-Forschung. Ulm Universität., Ulm, 2017.

[58] ATSM, Standard Test Method for Tensile Properties of Plastics (ATSM D638-02a), 2002.

[59] C. J. Smithells, «22: Mechanical properties of metals and alloys,» de *Smithells Metals Reference Book*, Butterworth-Heinemann, 2004.

[60] C. J. Smithells, «2: General physical properties of light metal alloys and pure light metals,» de *Smithells Light Metal Handbook*, Butterworth-Heinemann, 1998, p. 6.

[61] B. Mas, A. Monreal-Bernal, H. Yue, H. Zhang y J. J. Vilatela, «Understanding the Enhancement of Young's modulus of Macroscopic Carbon Nanotube Fibers After Polymer Infiltration,» de *AIP Proceedings, CNT-NET Conference*, Dresden, 2017.

[62] S. P. Timoshenko y J. M. Gere, Theory of Elastic Stability 2nd ed., Mineola, NY: Dover Publications, 2009.

[63] A. M. Gaikwad, B. V. Khau, G. Davies, B. Hertzberg, D. A. Steingart y A. C. Arias, «A High Areal Capacity Flexible Lithium-Ion Battery with a Strain-Compliant Design,» *Advanced Materials,* vol. 5, nº 3, pp. 1-11, 2014.

[64] D. Doerffel y S. A. Sharkh, «A critical review of using the Peukert equation for determining the remaining capacity of lead-acid and lithium-ion batteries,» *Journal of Power Sources,* vol. 155, nº 2, pp. 395-400, 2006.

[65] J. Lim, J. Gim, J. Song, D. Nguyen, S. Kim, J. Jo, V. Mathew y J. Kim, «Direct formation lf LiFePO4/graphene composite via microwave-assisted polyol process,» *Journal of Power Sources,* vol. 304, pp. 354-359, 2016.

[66] G. Bieker, M. Winter y P. Bieker, «Electrochemical in situ investigations of SEI and dendrite formation of the lithium metal anode,» *Physical Chemistry Chemical Physics,* vol. 17, pp. 8670-8679, 2015.

[67] Sigma-Aldrich, [En línea]. Available: https://www.sigmaaldrich.com/spain.html. [Último acceso: 25 September 2018].

[68] MTI Corporation, «Battery R&D Equipment,» [En línea]. Available: http://www.mtixtl.com/batterycapacitorequipment.aspx. [Último acceso: 25 September 2018].

[69] Mathworks, «Pricing and Licensing,» [En línea]. Available: https://www.mathworks.com/pricing-licensing.html?prodcode=ML&intendeduse=edu. [Último acceso: 25 September 2018].

[70] Microsoft Corporation, «Office 365, Personal,» [En línea]. Available: https://products.office.com/es-ES/. [Último acceso: 25 September 2018].

[71] F. Barciela, «España, la gran potencia de los 'composites',» *El País*, 24 Agosto 2014.

[72] Hexcel, «Plantas y Oficinas: Hexcel Illescas,» [En línea]. Available: https://www.hexcel.com/About/Site-Locations/1446/hexcel-illescas. [Último acceso: 25 September 2018].

[73] Gurit, «Sites Locations,» [En línea]. Available: http://www.gurit.com/About/Sites--Locations. [Último acceso: 25 September 2018].

[74] Airbus, «Our locations,» [En línea]. Available: http://company.airbus.com/careers/Our-locations.html. [Último acceso: 25 September 2018].

[75] Aerrnova, «La española Aernnova entrega la primera estructura compleja de materiales compuestos para el Boeing 787 Dreamliner,» [En línea]. Available: http://www.aernnova.com/es/la-espanola-aernnova-entrega-la-primera-estructura-compleja-de-materiales-compuestos-para-el-boeing-787-dreamliner/. [Último acceso: 25 September 2018].

[76] Crystal Market Research, «Carbon Nanotubes Market by Product Type, Method and Application - Global Industry Analysis and Forecast to 2022,» 2017.

[77] Accuray Research LLP , «Global Carbon Nanotubes Market Analysis & Trends - Industry Forecast to 2025,» Research and Markets, 2017.

[78] PR Newswire; New York , «FinancialBuzz.com: The Effects of Rechargeable Batteries on the Lithium Market,» 17 January 2017. [En línea]. Available: https://search.proquest.com/docview/1858941909?accountid=14501. [Último acceso: 25 September 2018].

[79] A. Mikhalchan, T. Gspann y A. Windle, «Aligned carbon nanotube–epoxy composites: the effect of nanotube organization on strength, stiffness, and toughness,» *Journal of Materials Science,* vol. 51, pp. 10005-10025, 2016.

[80] J. Webb, «Carbon nanofibres made from CO2 in the air,» BBC News. Science & Environment, 20 August 2015. [En línea]. Available: https://www.bbc.com/news/science-environment-33998697. [Último acceso: 25 September 2018].

[81] J. V. A. M. M. M. P. C. M. S. A. W. Krzysztof Koziol, «High-Performance Carbon Nanotube FIber,» *Science,* vol. 318, nº 1892, pp. 1892-1894, 2007.

[82] H. J.Y., S. Chen, R. Z.F., W. Z.Q., D. Wang, M. S. Z. C. G. Vaziri y M. Dresselhaus, «Superplastic carbon nanotubes,» *Nature,* vol. 439, nº 7074, p. 281, 2006.

[83] M. F. Ashby, P. J. Ferreira y D. L. Schodek, Nanomaterials, Nanotechnologies and Design: An Introduction for Engineers and Architects, Butterworth-Heinemann, 2009.

[84] K. Novoselov, A. Geim, M. S.V:, D. Jiang, M. Karsnelson, I. Grigorieva, S. Dubonos y A. Firsov, «Two-dimensional gas of massless Dirac fermions in graphene,» *Science,* vol. 306, pp. 666-669, 2004.

[85] M. Dresselhaus, G. Dresselhaus y R. Saito, «Physics of Carbon Nanotubes,» *Carbon,* vol. 33, nº 7, pp. 883-891, 1995.

[86] M. Moniruzzaman y K. Winey, «Polymer nanocomposites containing carbon nanotubes,» *Macromolecules,* vol. 39, nº 16, pp. 5194-5205, 2006.

[87] H. O. Pierson, Handbook of Chemical Vapor Deposition (CVD): Principles, Technology and Applications, 2nd ed., Albuquerque: William Andrew, 1999.

[88] R. Baker, *Carbon*, nº 27, p. 315, 1989.

[89] Y. Homma, «Chapter 9: Carbon Nanotube Synthesis and the Role of Catalyst,» de *Frontiers of Graphene and Carbon Nanotubes*, Tokyo, Springer, 2015, pp. 125-129.

[90] S. Li, X. Zhang, J. Zhao, F. Meng, G. Xu, Z. Yong, J. Jia, Z. Zhang y Q. Li, «Enhancement of carbon nanotube fibres using different solvents and polymers,» *Composites Science and Technology*, vol. 72, nº 12, pp. 1402-1407, 2012.

[91] J.-L. Basdevant, J. Rich y M. Spiro, Fundamentals in Nuclear Physics, Springer, 2005.

[92] J. J. Vilatela y D. Eder, «Nanocarbon Composites and Hybrids in Sustainability: A Review,» *ChemSusChem*, vol. 5, pp. 456-478, 2012.

[93] M. F. Ashby, H. Shercliff y D. Cebon, Materials: Engineering, Science, Procesing and Design, 2nd ed., Oxford: Butterworth-Heinemann, 2010.

[94] R. C. Hibbeler, Mechanics of Materials, 9th ed..

[95] A. Yamada, H. Koizumi, S.-I. Nishimura, N. Sonoyama, R. Kanno, M. Yonemura, T. Nakamura y Y. Kobayashi, «Room-temperature miscibility gap in LiXFePO4,» *Nature materials*, vol. 5, pp. 357-360, 2006.

A. APPENDIX: Study of the dependence of tensile properties of a CNT mat on the specimen shape

As discussed previously in section 2.3.1, it was decided not to constraint the testing procedure with the available standards because, despite the limited resources, the ongoing research needed an agile way to extract preliminary values for the mechanical properties of the electrodes. Probably, of all the deviations from the standard, the one with the biggest impact was the specimen shape. What follows are the reasons behind using the specimen type I instead of type II or III, presented in Figure A.1.

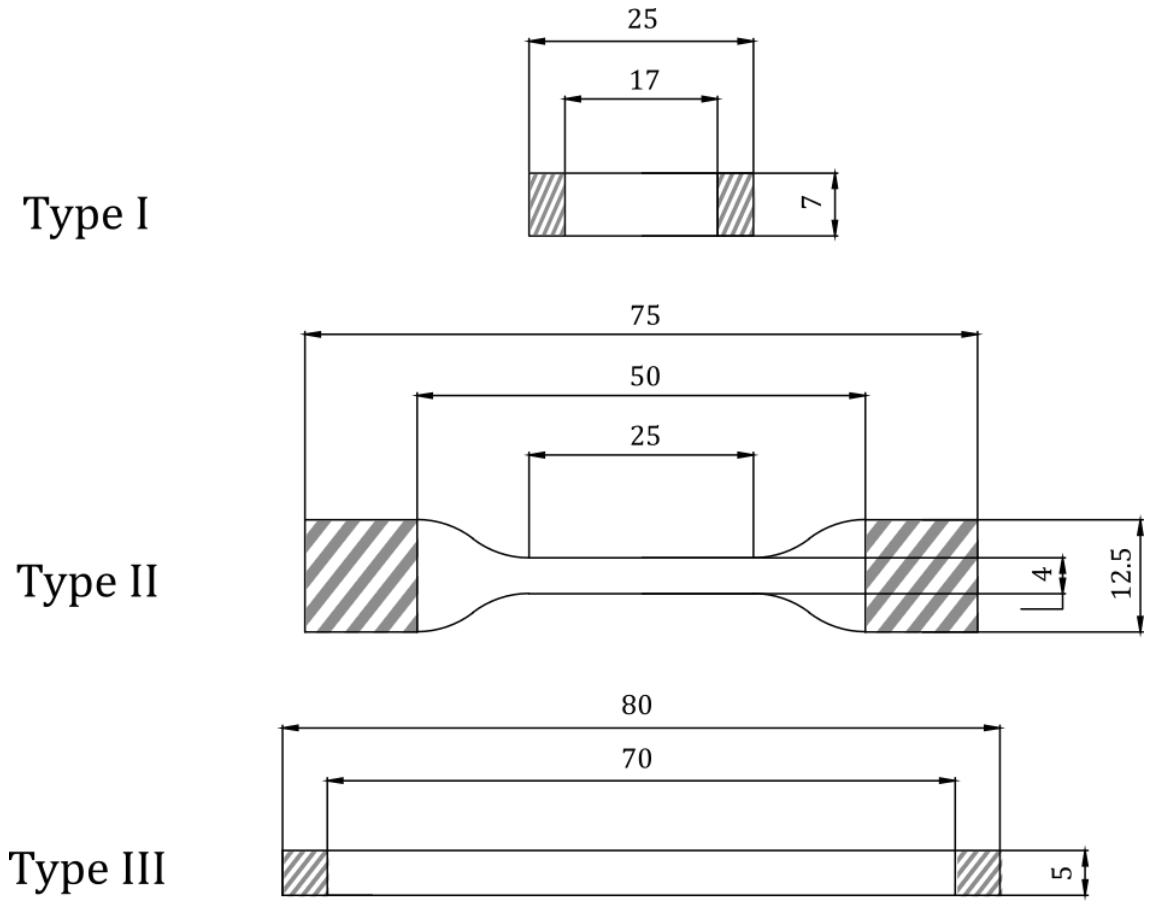

Figure A.1: Specimen geometries utilized for the shape-dependence assessment. Line-pattern denotes gripped region. Units in mm.

At first, the dog-bone shape and big aspect ratio of type II looks as the better choice to ensure the correct stress concentration at the gauge length. However, it was discarded for several reasons. It required a specific tooling to be cut, instead of a general-purpose knife or razor and, although there was one available, it was large; too large for the current size of the strips of CNTs and the electrodes produced at IMDEA. Also, the dog-bone shape

forced the utilization of an external device to measure the elongation of the gauge length; either a mechanical extensometer or Digital Image Correlation (DIC). The first one was not suitable for materials as thin as the ones tested here, while the DIC complicated the process noticeably. An experiment to the determine the potential benefit of this technique is presented in this section (pictures of the set up are included as Figure A.4-a,-b and -c). Lastly, the large dimensions of the type II also disqualified the use of the DMA machine because its length was too big to fit into the maximum grips separation (24 mm). The importance of having the possibility to use the same specimen interchangeably in different apparatus is discussed in the conclusions section.

Similar reasons forced to discard type III, with its advantageous bigger aspect ratio. However, this kind, although possible to be cut with conventional tools, also resulted in a larger consumption of raw material, thus reducing the number of specimens potentially obtainable from a given batch. Sample size was given priority to ensure the statistical relevance of the data. An advantage of the rectangular shape was the possibility of using the increase in length between the grips of the machine as the elongation of the sample, instead of using the extensometer or the DIC. However, the big size disqualified the interchangeability between the Instron and the DMA machines in the same manner as with type II.

With all those reasons being considered, the decision was to use specimen type I. It guaranteed a moderate use of raw material, which allow for bigger sample sizes; it was possible to measure the elongation directly from displacement raw data of the machine, streamlining the process compared to the steps required by the DIC; it could be tested interchangeably in the two different machines available; and it could be cut with conventional tools. The issue with stress concentration at the grips of rectangular specimens was addressed with the logic introduced at the end of section 3.1.4. That is, validating the results of specimens broken at the grips with specimens broken at the middle (Figure 3.7.-l and -m, respectively).

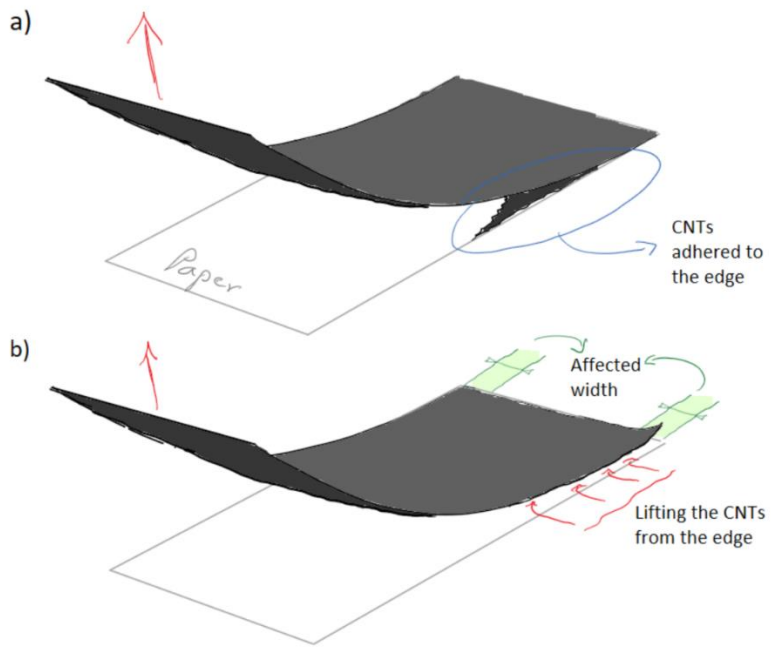

Figure A.2: Schematics of the phenomenon encountered during the separation of a CNT specimen from the protective paper. (a) shows the region where the CNTs stuck. (b) The way it had to be lifted to avoid the further propagation of the delamination.

Narrower strips could have been prepared to increase the aspect ratio. Nonetheless, the 7 mm width was fixed to increase the range of forces at which failure of the samples would occur, thus reducing the noise that would appear working so far of the 500 N limit of the load cell. Another reason to keep the width was a particular phenomenon observed during CNT samples preparation, described as follows. CNT mats are typically delivered over a protective substrate (i.e., of paper). This protector was cut simultaneously with the proper CNT mat, and remained attached to each specimen before placing it on the testing support. At that moment, during the separation of the CNT strip and the paper (see Figure A.2), the strip would tend to stick to the edges of the paper (a), probably as a consequence of the pressure exerted by the knife during cutting and the great tendency of the CNTs to adhere due to their high porosity. This adhesion could cause the layers of CNT bundles to delaminate obliquely to the edges, what had to be stopped by lifting the CNT strip firstly by the edges of the paper (b). However, small delaminations occurring along the edge regions were impossible to avoid, affecting some portion of the total width (green zones, in Figure A.2.b). A smaller width would have increased the relative importance of this unavoidable defects introduced during the preparation.

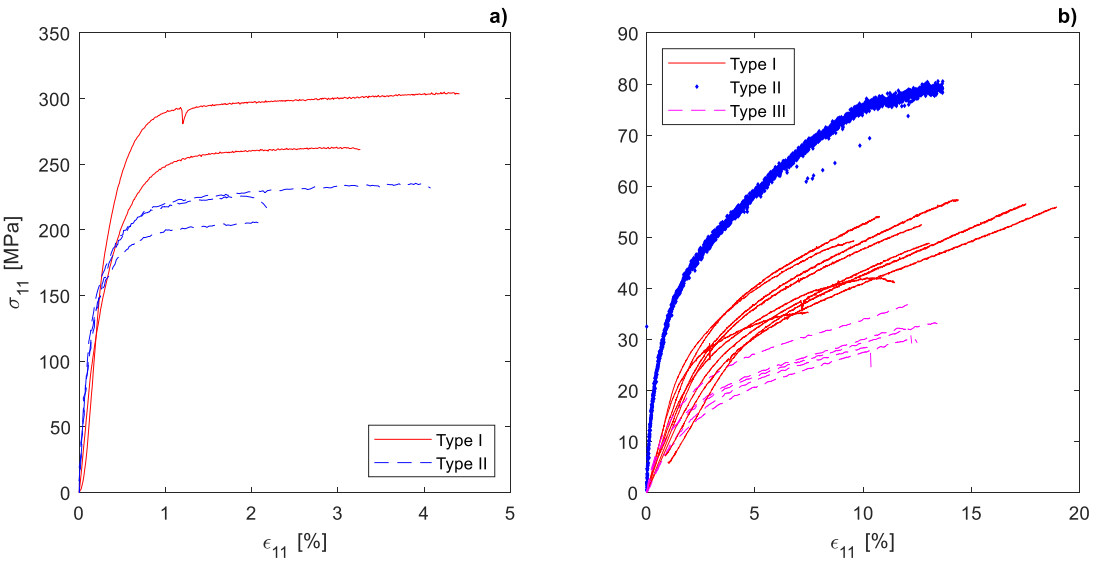

Figure A.3: Stress-strain curves comparing different kinds of specimens. (a) Copper samples. (b) Tortech CNT mat. Refer to Table 13 for more details.

Despite all this reasoning, a limited set of tests of the more ideal sample-types II and III was performed. Their results are introduced in Table 13 to establish a comparison with the type I that allows to extrapolate the conclusions obtained.

Table 13: Comparison of different specimen shapes.

Material	Copper	Copper	Tortech CNT	Tortech CNT	Tortech CNT
Specimen type	I	II	I	II	III
Strain measurement	Grip disp.	DIC	Grip disp.	DIC	Grip disp.
$\varepsilon_b(\%)$	3.8 ± 0.7	3.1 ± 0.1	14 ± 5	13.6 ± 0.4	11.9 ± 1.0
$\sigma_b(MPa)$	287 ± 56	211 ± 43	52 ± 15	80 ± 13	31 ± 8
$E\ (GPa)$	75 ± 19	87 ± 22	1.2 ± 0.5	7.4 ± 1.4	1.4 ± 0.7
$\sigma_b' \left(MPa \left(\frac{g}{cm^3}\right)^{-1}\right)$	35 ± 6	25 ± 5	137 ± 43	211 ± 38	83 ± 22
$E' \left(GPa \left(\frac{g}{cm^3}\right)^{-1}\right)$	9 ± 2	11 ± 3	3 ± 1	20 ± 4	4 ± 2

From the data gathered, this set of tests lets extract conclusions for both the copper and the CNT mats. It is stated that shapes II and III are, in principle, more reliable than type I. As well, DIC is considered to provide with a more accurate strain measurement.

Starting with the metal, the comparison of the values the three main parameters (namely strain at break, strength and modulus) works to prove that the shape I provides with numbers that fall on the uncertainty ranges of shape II. In terms of averages, there is a 16% increase in the modulus when comparing the DIC, dog-bone shape sample with the rectangular specimens. This would agree with the hypothesis of slightly uneven stress-distribution on the cross section of the specimen I that was mentioned in section 3.1.2. There is also a reduction of 19% and 26% in strain at break and tensile strength, respectively. This is thought to be a consequence of rough cutting edges of the cutting tool which could induce early failure of the specimens. These imperfections can be observed slightly in Figure A.5.a. In any case, the ranges of properties are comparable enough to consider acceptable the result of the type I specimens.

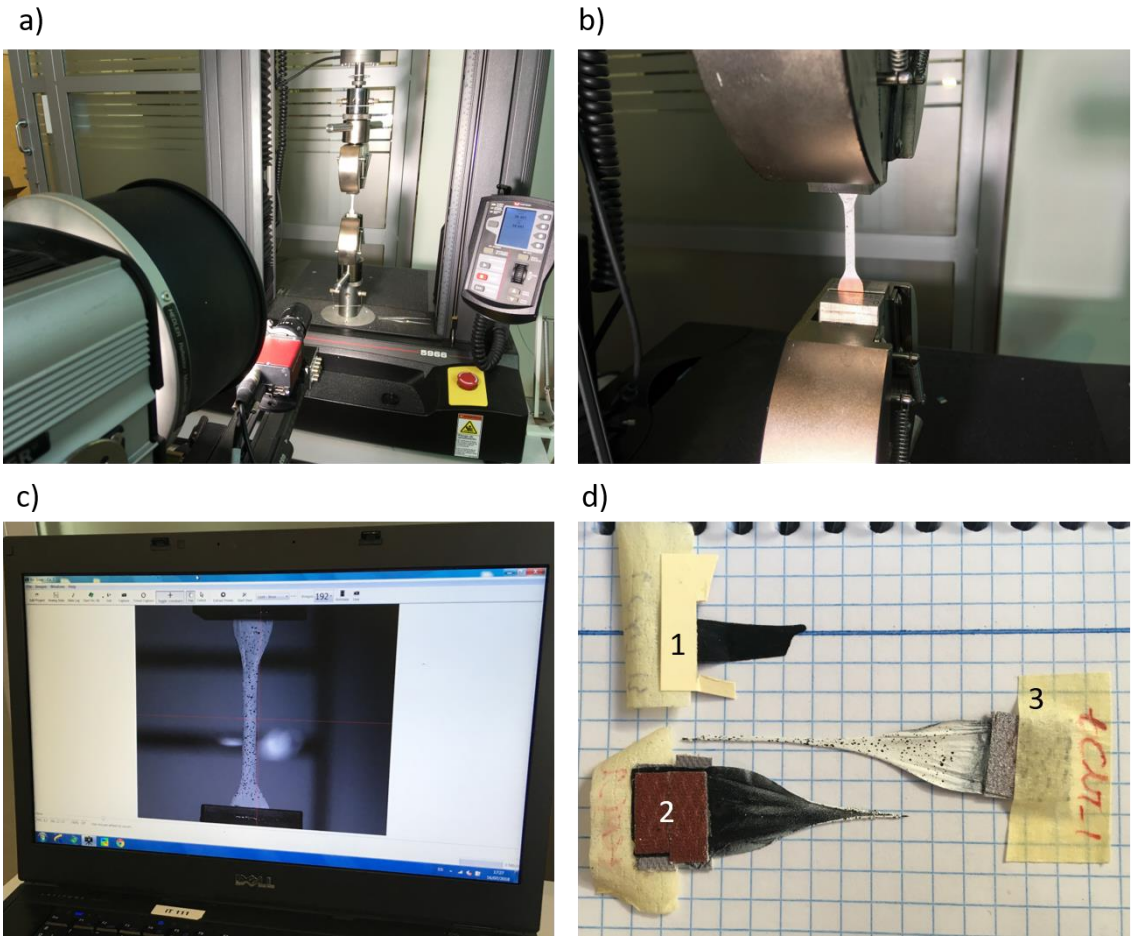

Figure A.4: (a) Test set-up for DIC. (b) Cu specimen ready for testing. (c) Visualization of the camera image on the software. (d) Detail of a CNT specimen after testing. Notice that 2 is whiter than 1.

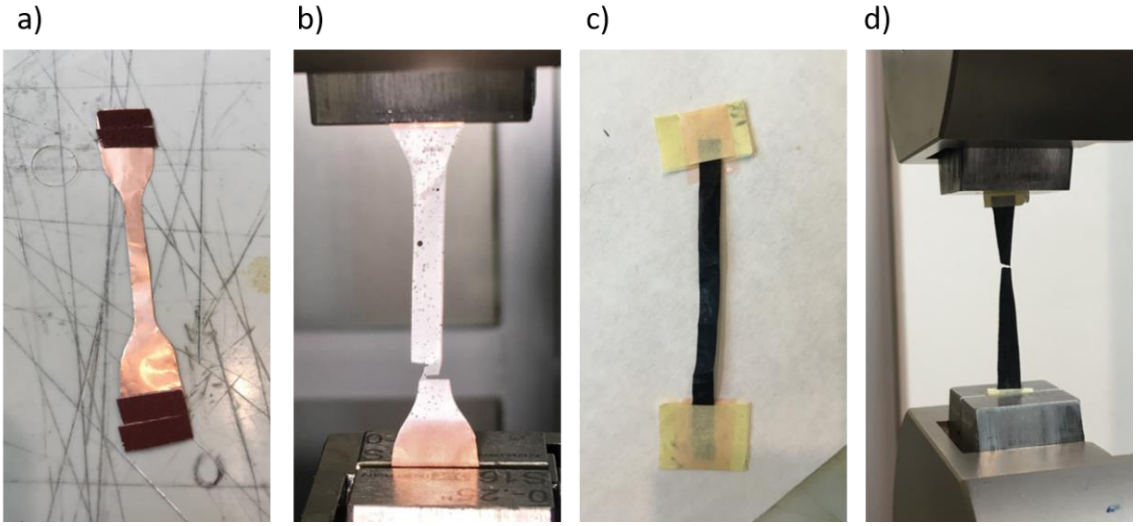

Figure A.5: (a) Specimen type II of copper, before testing. (b) Same Cu specimen after testing, with special contrast paint for DIC. (c) Specimen type III of CNT. (d) Same specimen after breakage.

The Tortech CNT mat was also tested with a type II specimen using the DIC. Figure A.4-d shows a picture of the only specimen evaluated with this method, whose two halves after breakage are denoted by the numbers 2 and 3 in the photograph. The number 3 is the side where the special paint for the image correlation was applied, while 2 is the opposite face, and 1 is another broken specimen of Tortech mat without any paint. From the picture it is possible to notice the difference in darkness between the specimen without paint and the one with paint, even at the face where the paint was not applied. The white shades of 2 evidence the penetration of the paint in the mat. The remarkable increase in modulus (6 times more) of the DIC sample with respect to the other two Tortech mat samples present in Table 13 is attributed to a stiffening of the material caused by this paint penetration.

Finally, the Tortech mat results were confirmed with data coming from type III specimens (Figure A.5-c and -d). This kind of specimens was prepared before any other as a preliminary assessment of the testing methods. The switch to type I was done afterwards due to the reasons explained at the beginning of this section. However, the fact that they were performed earlier did not affect the validity of the comparison with the type I sample. A comparison that, after analyzing the ranges of properties obtained, allows us to conclude that the use of a specimen with such a low aspect ratio as type I does not compromise the results remarkably.

In any case, the reduction in strength, which occurs when increasing the gauge length and aspect ratio, is related to the yarn-like nature of the CNT bundles. Both specimens have gauge lengths one order of magnitude higher than the typical length of a CNT bundle (~10 vs. ~1 mm), which means that the strength increase observed is not a consequence of CNT bundles spanning continuously from grip to grip. If this were the case, a new statistical modal peak at higher tensile strengths would appear, as it can be seen in the works by Elliot et al. [55] and Koziol et al. [81] on single CNT yarns. That new peak is centered at tensile strengths 4 or 5 times the principal peak. The increase in strength occurring here when switching from the 80 mm specimen to the 17 mm one, which is approximately 1.7 times, is much smaller. This suggests that the behavior observed has to be a consequence of a different phenomenon.

In a publication by Gspann et al. [56], the opposite trend for strength vs. specimen gauge length is presented. The cause is claimed to be the heterogeneous stress distribution on the cross section of the specimen which occurs at short gauge lengths. This happens because the stress transfers that occurs at the grips from the outer CNT bundles to the inner ones is very inefficient due to the low shear strength of the van-der-Waals friction mechanism that links them [55]. The consequence is that, unless sufficient length is available, the shear load of the grips will not be completely transferred to the whole cross section of the yarn; the outer layers will cope with a larger portion of the load and that exterior stress concentration will result in a premature failure of the yarn. The required length to achieve the homogeneous stress distribution can be noticeably reduced if friction-enhancing mechanisms enter the scene. The presence of particulate impurities as catalyst residue and the lack of alignment of the bundles are two phenomena that increase the bundle-to-bundle friction, the first acting as an internal *sandpaper* and the second helping in carrying the load transversely to the inner layers. [56] At the same time, an increased specimen length also enlarges the probability of finding longitudinal defects such as terminations of bundles, CNT ends, reversing loops or longitudinal voids with limited or no presence of branching bundles [56].

With all these precedents, keeping in mind that they refer CNT yarns and not the mats which are the object of this study, the conclusion obtained is as follows: for a randomly-oriented commercial mat, seems reasonable to expect the presence of some impurities and, mainly, the existence of transversely oriented bundles. Both enhance the load transfer from the shearing of the grips to the stretching of the material. Therefore, the reduction

in strength (52 vs. 31 MPa) in sliding modulus (190 vs. 124 MPa) looks like the result of the higher probability of longitudinal defects of the longer specimen.

B. APPENDIX: Error propagation in magnitudes

Here the equations for the propagation of uncertainties in the experimental measurements are presented.

The uncertainty values (Δ) were chosen as the maximum between the standard deviation of a sample and the resolution of the measurement device utilized.

The magnitudes measured directly were:

- Breaking force, F_b
- Width, w
- Thickness, t
- Gauge length, L_o
- Total length, L
- Elongation, ΔL
- Force-displacement slope, k, by least-squares.
- Mass, m
- Capacity, C, as the integral of current vs. time, provided by the cycler.
- Energy, E, as the integral of the current-potential product vs. time, provided by the cycler.
- Diameter, D.

Mass properties

Areal density, ρ_a

$$\Delta\rho_a = \frac{m}{L\,w}\left(\frac{\Delta m}{m} + \frac{\Delta L}{L} + \frac{\Delta w}{w}\right) \quad \text{(B.1)}$$

Tex, T

$$\Delta T = \Delta\rho_a w + \rho_a \Delta w \quad \text{(B.2)}$$

Mass loading, m_{load}

$$\Delta m_{load} = \Delta\rho_{a_{coated}} + \Delta\rho_{a_{uncoated}} \quad \text{(B.3)}$$

Mass fraction, m_f

$$\Delta m_f = \frac{m_{load}}{\rho_{a_{coated}}}\left(\frac{\Delta m_{load}}{m_{load}} + \frac{\Delta\rho_{a_{coated}}}{\rho_{a_{coated}}}\right) \quad \text{(B.4)}$$

Mechanical properties

Strength, σ_b

$$\Delta\sigma_b = \frac{F_b}{w\,t}\left(\frac{\Delta F_b}{F_b} + \frac{\Delta w}{w} + \frac{\Delta t}{t}\right) \quad \text{(B.5)}$$

Modulus, E

$$\Delta E = \frac{kL_o}{w\,t}\left(\frac{\Delta L_o}{L_o} + \frac{\Delta k}{k} + \frac{\Delta w}{w} + \frac{\Delta t}{t}\right) \quad \text{(B.6)}$$

Elongation at break, ε_b

$$\Delta\varepsilon_b = \frac{\Delta L}{L_o}\left(\frac{\Delta(\Delta L)}{\Delta L} + \frac{\Delta L_o}{L_o}\right) \quad \text{(B.7)}$$

Specific strength, σ_b'

$$\Delta\sigma_b' = \frac{F_b}{T}\left(\frac{\Delta\sigma_b}{\sigma_b} + \frac{\Delta T}{T}\right) \quad \text{(B.8)}$$

Specific modulus, E'

$$\Delta E' = \frac{F_b}{T}\left(\frac{\Delta\sigma_b}{\sigma_b} + \frac{\Delta T}{T}\right) \quad \text{(B.9)}$$

Electrochemical properties

Nominal capacity, C_{nom}

$$\Delta C_{nom} = \frac{C}{m_{active}}\left(\frac{\Delta C}{C} + \frac{\Delta m_{active}}{m_{active}}\right) \quad \text{(B.10)}$$

Specific energy, E_s

$$\Delta E_s = \frac{E}{m_{active}}\left(\frac{\Delta E}{E} + \frac{\Delta m_{active}}{m_{active}}\right) \quad \text{(B.11)}$$

Surface capacity, C_{surf}

$$\Delta C_{surf} = \frac{4\,C}{\pi\,D^2}\left(\frac{\Delta C}{C} + \frac{2\Delta D}{D}\right) \quad \text{(B.12)}$$